

Dear Dr. Cziczó,

Below you will find our point-by-point responses to each of the reviewers, including an indication of changes made in response to their comments. In addition, you will find an annotated “track changes” version of the manuscript. We have made numerous changes to the manuscript in response to the reviewer comments, and believe that we have addressed their concerns in full. We thank you for your consideration of this work.

Regards,

Chris Cappa

UC Davis

## Response to Comments from Anonymous Referee #1

Response to comments on “Understanding the Optical Properties of Ambient Sub- and Supermicron Particulate Matter: Results from the CARES 2010 Field Study in Northern California” by C. D. Cappa et al.

We thank the reviewer for her/his comments, which have helped us to improve our work. The original reviewer comments are in **black** and our responses are in **blue**.

This paper comprehensively reports the results of optical properties measurements made as part of the CARES campaign. This is a very weighty paper and while the conclusions could not really be regarded as game-changing, the high quality of the measurements and the depth of the analysis means that these results are still very important and relevant to ACP, having a wide range of potential applications in radiative transfer and the interpretation of remote sensing data. I would recommend that this be published subject to minor corrections.

General: I found the various combinations of sampling conditions referred to a bit bewildering at times. It would greatly help the reader if a schematic figure could be given showing the different sampling arrangements for the different sites. On a related note, I also found the large number of mathematical symbols to be a bit confusing at times, so it would be useful to compile these as a table.

A table has been added to aid the reader in recalling the definition of symbols used throughout the manuscript (new Table S1). A schematic has also been added to the supplemental material (new Figure S2).

Line 122: The method used to humidify the sample flow to 85%, including the methods to monitor and control the humidity, should be described here.

The following sentence has been added to address the method used for humidification:

“The air stream was humidified by passing it through a custom humidifier, which consisted of a semi-permeable capillary membrane (Accurel) that was kept continuously wetted. The relative humidity in the CRD cells was monitored using Vaisala RH probes (HMP50) that were calibrated using saturated salt solutions.”

Line 128: A reference should be supplied for the mobility conversion for the aerodynamic diameters. Rather than assume sphericity (which is probably not valid for dust and dry sea salt particles), it would probably be more correct to refer to the assumed 2 g/cc density as the ‘effective’ density.

A reference has been added (DeCarlo et al., 2004) and we now use the “effective density” terminology.

Line 138: These mobility diameters should be qualified as ‘approximate’ because they have each been clearly rounded off compared to the actual theoretical values.

The sentence now reads:

“The mobility equivalent cut-diameters are (assuming a density of  $2 \text{ g cm}^{-3}$ ) *approximately* 700 nm, 1750 nm and 7200 nm, respectively.”

Line 166: The factor of 1.66 is contrary to the factor of 1.33 recommended by Laborde et al. (2012b), so the nature of the ‘personal communication’ cited may need expanding on here.

First, we note that we used 1.53, not 1.66. Second, we note that in Laborde et al., the relationship between Aquadag and Fullerene soot is not 1.33, but a larger factor. From their Fig. 5, using a BC particle mass of 10 fg as a reference point, the scaling between these two is about  $1.35/0.9 = 1.5$ , which is very similar to the value of 1.53 used here. Finally, we have added the sentence “This adjustment factor was determined from laboratory studies conducted after the CARES campaign.”

Line 233: A reference should be included here because the exact effect BrC has on AAE is by no means certain.

We fully agree that the effect of BrC on AAE values is “by no means certain.” At the same time, it seems quite clear that BrC tends to increase the AAE over pure BC. We have added a reference to Lack and Cappa (2010) here, although there are many references that could be chosen to illustrate this point.

Line 238: Similarly, include references for examples of how SAE is ‘commonly used’.

We have added a reference to (Clarke and Kapustin, 2010), which summarizes results from 14 different flight campaigns using SAE as a key criteria for particle size. Many references could be chosen, so we have taken the approach of selecting just one that considers a multitude of different data sets.

Line 384: What AAE would be necessary to cancel out any influence from BrC? How does this compare with DOI:10.1002/2014GL062443?

For BrC to be entirely cancelled out, the AAE for BC would need to simply be assumed equal to the observed AAE, namely 1.17 at T0 and 1.28 at T1 (from Table 2). We have modified the sentence to read: “if the actual  $AAE_{BC}$  were  $>1$ , as possibly suggested by the  $AAE_{532-660}$  measurements at both sites, then the attributed brown carbon fraction would be even smaller *and cancelled out entirely if  $AAE_{BC}$  equals the observed value for the ambient particles.*”

Regarding the comparison with Liu et al. (2015), we are not entirely certain what the reviewer is asking us to compare. The Liu et al. (2015) study is primarily a theoretical study when it comes to consideration of the AAE. What we are discussing is really an empirical approach to assessing BrC properties. In other words, an AAE is assumed for BC, and then BrC is “attributed” by difference. Yes, the actual AAE for BC is predicted to be larger than one by Mie theory when “large” particles ( $\sim 100 \text{ nm}$ , as opposed to  $<30 \text{ nm}$  spherules) are used, and as has been discussed many times prior to the Liu et al. study, most notably by Lack and Langridge (Lack and Langridge, 2013) who address specifically the question of how assumptions regarding the AAE of BC influence the attribution of BrC. This is, in some ways, exactly our point in indicating that

if the AAE for BC is  $> 1$  (the base assumption, commonly made) then our attribution would overestimate the absorption attributable to BrC.

Line 402: A more fundamental reason the PALMS and SPLAT II are not capable of quantifying contributions from BC internally mixed on dust particles is the matrix effects associated with each instrument, such that the mass fractions reported on individual particles are not quantitative.

We have modified this sentence to also indicate that matrix effects may preclude explicit quantification even if particles were sampled across the entire size range. Specifically, “Although informative, these measurements unfortunately cannot be used to quantitatively assess the relative contributions of the different absorbing particle types to the supermicron absorption because both instruments sample only over a subset of the entire supermicron size range, e.g. the SPLAT-II only up to  $d_{v,a} \sim 2 \mu\text{m}$ , and matrix effects can impact quantification of individual components in mixed particles (e.g. BC mixed with dust).”

Line 453: Shouldn't the qualitative influence of sea salt particles be evident in the single particle mass spectrometer data?

Ideally, yes. However the particle sampling statistics during CARES make it difficult to develop a qualitative picture that can be confidently assessed in this case.

Line 514 (and elsewhere): “consistent with that of (Russell et al., 2010)” should read “consistent with that of Russell et al. (2010)”

These have been fixed.

Line 531: This opening statement should be made more descriptive, as it isn't specified what exactly the effect on climate is. It may also be worth mentioning that this is an important parameter for remote sensing retrievals.

The statement now reads:

“The extent to which particles scatter light in the backward versus forward direction has an important controlling influence on their climate impacts, *namely the amount of incident solar radiation that is reflected back to space and the associated radiative forcing* (Haywood and Shine, 1995). *Furthermore, the backscatter fraction and asymmetry parameter are important parameters for remote sensing retrievals.*”

Line 573: Was any correction for thermophoretic losses invoked? If not, the authors should comment on how much of an issue they believe this to be.

Yes, a correction for thermophoretic losses was applied, similar to what was done in Cappa et al. (2012). The correction factor for particles that passed through the TD was 0.8. We have added the following statement to the methods: “Measurements made through the thermodenuder were corrected for thermophoretic losses (Huffman et al., 2008).”

Line 593: According to conventional wisdom, supermicron sulphate and nitrate tends to be in the form of salts of calcium and sodium rather than ammonium, which makes them quite involatile, so I would doubt that this is significant.

We have clarified this to indicate that we mean that there could *potentially* be evaporation of “inorganics such as *ammonium* sulfate and *ammonium* nitrate,” although we agree with the reviewer that this is likely to be less important than organics.

Line 599: A related hypothesis could be that undenuded sea salt particles do not completely effloresce during drying due to the presence of magnesium salts (doi: 10.5194/acp-15-11273-2015) and organics. If the denuded particles are more completely dried out (due to the water being boiled off) then this would increase their apparent hygroscopicity further.

This is certainly a possibility. The “2-D Area Ratio” reported in the reference given (Gupta et al., 2015) for pure  $\text{MgCl}_2$  at 30% RH is about 1.3 and for pure  $\text{NaCl}$  at 80% RH is about 5. Given that the diameter growth factor (GF) for  $\text{NaCl}$  is  $\sim 2$  at 80% RH, this implies that the equivalent  $\text{MgCl}_2$  GF at 30% RH is around 1.07. The mass ratio between Mg and Na in sea water is about 0.12. Thus, the  $\text{MgCl}_2$  would be only a small fraction of the sea salt ( $\text{NaCl}$  would dominate) and the  $\text{MgCl}_2$  would have only a negligible impact on the average water content of the particles. In fact, this is apparent in Gupta et al., who find that the 2-D Area Ratio is only about 1.2 at 30% RH for mixed  $\text{NaCl}/\text{MgCl}_2$  particles where the  $\text{NaCl}$  mole fraction is 0.9. In this case, the equivalent GF would be 1.05. Thus, although residual water due to magnesium salts could influence the measurements, the magnitude of this influence would be small. Although we believe this to most likely be an unimportant effect, we have added the following sentences to indicate it as a possibility. “It is possible that the thermodenuding removed residual water that did not fully evaporate in the drier due to the presence of magnesium sea salts (which do not effloresce until very low RH), leading to an apparent increase in the hygroscopicity of the thermodenuded particles. However, the potential impact from this is expected to have been quite limited, given the small amount of residual water retained by magnesium salts at low RH (Gupta et al., 2015).”

Line 620: How does this fit in with the conclusions of Doi:10.1038/Ngeo2220?

Saleh et al. (2014) also observe that the brown carbon fraction from biomass burning samples has a higher effective absorptivity at shorter wavelengths. Saleh et al. (2014) also argue that heating can leave behind more lower-volatility organics that are more absorbing than the higher-volatility species that evaporate more easily in a thermodenuder. This can lead to a suppression of observable absorption enhancement values over the “true” value for BC. However, Cappa et al. (2011) showed that the thermodenuder-derived  $E_{\text{abs}}$  values behaved very similarly to  $E_{\text{abs}}$  values derived from consideration of mass absorption coefficients for CARES, which suggests that such “residual” more-absorbing organics are playing a negligible role here (see the Supplementary Material of that paper). We also note that Zhang et al. (2016) also found good agreement between thermodenuder-derived and MAC-derived  $E_{\text{abs}}$  values for a region known to be impacted by biomass burning (the focus of the Saleh et al. study), suggesting that the limitations of the heating method identified by Saleh et al. (2014) may be limited in scope. This is certainly an issue that remains to be fully resolved, but is not a major point of this work and thus we have not pursued it further here.

Line 646: The caveat should be added that this is assuming that the particles have not acquired an involatile coating (e.g. coagulation with sea salt, condensation of humiclike SOA), because this could confound any attempt to isolate the effect of morphological changes on SSA.

We have added the following sentence: “However, if non-absorbing and non-volatile materials remained (e.g. sea salt), then the extrapolated SSA would not be fully representative of pure BC particles, confounding straightforward interpretation in terms of morphological changes.”

Line 653: It should be noted that if the particles are thought to be very non-spherical, the SMPS sizing is likely to be overestimated to a large degree

True, but shape effects would not be large enough to make the SMPS-measured 300 nm shift down to  $< \sim 50$  nm, which would be necessary to explain such small SSA values.

Line 653: If the particles are fundamentally different to ‘normal’ black carbon particles, then the SP2’s calibration could be invalid and the equivalent core sizes reported inaccurate. If the instrument had a narrow band incandescence detector, it may be informative to compare the ratio of this to the broadband detector to see if the apparent colour temperature had changed.

This is an interesting point. Laborde et al. (2012) reported SP2 sensitivities for a variety of different BC types. The largest difference observed corresponded to a sensitivity ratio of about 1.6. If the SP2 were too sensitive towards the asphalt particles by a factor of 1.6 (in per particle mass), then the diameter would be overestimated by a factor of  $1.6^{1/3} = 1.17$ . Fig. S9 (now S10) showed the particles during the asphalt-impacted period to be about a factor of 2 larger in diameter. This would require a mass sensitivity difference of  $2^3 = 8$ . This seems unreasonably large, given the results shown in Laborde et al. (2012). Thus, although we agree that the particles may have been detected with a somewhat different sensitivity than typical ambient BC particles, the difference is unlikely to make a substantial impact on the conclusions here, and certainly unlikely to invalidate our conclusion that it is most likely that the particles are composed of smaller spherules.

Figure S1: Adjust the colour scale so that areas covered by land are green rather than blue.

Done.

Figure S9: Given that Babs of black carbon is more closely related to mass than number, a mass-weighted distribution comparison would be informative here.

Done. The conclusions are unaffected.

## References

Cappa, C. D., Onasch, T. B., Massoli, P., Worsnop, D., Bates, T. S., Cross, E., Davidovits, P., Hakala, J., Hayden, K., Jobson, B. T., Kolesar, K. R., Lack, D. A., Lerner, B., Li, S. M., Mellon, D., Nuaanman, I., Olfert, J., Petaja, T., Quinn, P. K., Song, C., Subramanian, R., Williams, E. J., and Zaveri, R. A.: Radiative absorption enhancements due to the mixing state of atmospheric black carbon Science, 337, 1078-1081, doi:10.1126/science.1223447, 2012.

Clarke, A. and Kapustin, V.: Hemispheric Aerosol Vertical Profiles: Anthropogenic Impacts on Optical Depth and Cloud Nuclei, 329, 1488-1492, doi:10.1126/science.1188838, 2010.

Gupta, D., Eom, H. J., Cho, H. R., and Ro, C. U.: Hygroscopic behavior of NaCl–MgCl<sub>2</sub> mixture particles as nascent sea-spray aerosol surrogates and observation of efflorescence during humidification, *Atmos. Chem. Phys.*, 15, 11273-11290, doi:10.5194/acp-15-11273-2015, 2015.

Haywood, J. M. and Shine, K. P.: The Effect of Anthropogenic Sulfate and Soot Aerosol on the Clear-Sky Planetary Radiation Budget, *Geophys. Res. Lett.*, 22, 603-606, doi:10.1029/95GL00075, 1995.

Huffman, J. A., Ziemann, P. J., Jayne, J. T., Worsnop, D. R., and Jimenez, J. L.: Development and characterization of a fast-stepping/scanning thermodenuder for chemically-resolved aerosol volatility measurements, *Aerosol Sci. Technol.*, 42, 395-407, doi:10.1080/02786820802104981, 2008.

Laborde, M., Mertes, P., Zieger, P., Dommen, J., Baltensperger, U., and Gysel, M.: Sensitivity of the Single Particle Soot Photometer to different black carbon types, *Atmos. Meas. Tech.*, 5, 1031-1043, doi:10.5194/amt-5-1031-2012, 2012.

Lack, D. A. and Langridge, J. M.: On the attribution of black and brown carbon light absorption using the Angstrom exponent, *Atmos. Chem. Phys.*, 13, 10535-10543, doi:10.5194/acp-13-10535-2013, 2013.

Saleh, R., Robinson, E. S., Tkacik, D. S., Ahern, A. T., Liu, S., Aiken, A. C., Sullivan, R. C., Presto, A. A., Dubey, M. K., Yokelson, R. J., Donahue, N. M., and Robinson, A. L.: Brownness of organics in aerosols from biomass burning linked to their black carbon content, *Nat. Geosci.*, 7, 647-650, doi:10.1038/ngeo2220, 2014.

Zhang, X., Kim, H., Parworth, C., Young, D. E., Zhang, Q., Metcalf, A. R., and Cappa, C. D.: Optical Properties of Wintertime Aerosols from Residential Wood Burning in Fresno, CA: Results from DISCOVER-AQ 2013, *Environ. Sci. Technol.*, 50, 1681-1690, doi:10.1021/acs.est.5b04134, 2016.

## Response to Comments from Anonymous Referee #2

Response to comments on “Understanding the Optical Properties of Ambient Sub- and Supermicron Particulate Matter: Results from the CARES 2010 Field Study in Northern California” by C. D. Cappa et al.

We thank the reviewer for her/his comments, which have helped us to improve our work. The original reviewer comments are in **black** and our responses are in **blue**.

This paper describes measurements of absorption, scattering, and extinction for PM<sub>1</sub>, PM<sub>2.5</sub>, and PM<sub>10</sub> particles at two field sites near Sacramento, California. The authors use these measurements to conclude that supermicron particles contribute approximately half of scattering, and are composed of varying amounts of dust and sea salt. Photochemical processing does not have a consistent effect on submicron aerosol scattering, partly due to transport. The authors propose relationships between other intensive aerosol properties. This is a well-written paper, although the discussion is long and could possibly benefit from some condensing. I recommend publication after the following issues are addressed.

### *Major comments:*

1. The introduction is short and does not summarize existing knowledge about the composition and optical properties of supermicron aerosol. A previous study from the CARES campaign has already reported the unexpectedly large contribution of coarse mode aerosol to radiative forcing (Kassianov et al., 2012). This paper and other relevant results (possibly including Malm et al., 1994; Dubovik et al., 2002; Hand et al., 2002; Malm et al., 2007; Eck et al., 2010) should be described and cited in an expanded introduction.

We have expanded the introduction to some extent. We now note that while measurements of PM<sub>1</sub> and PM<sub>10</sub> composition and mass (which allows determination of supermicron particle properties) have become routine, the measurements of supermicron particle optical properties (via difference between PM<sub>10</sub> and PM<sub>1</sub> measurements) remain relatively uncommon. This goes directly to studies such as Kassianov et al. (2012), in which optical properties were inferred from size distribution measurements. Our paper reports on actual measurement of the supermicron optical properties and does not rely on “reconstruction” of optical properties from mass or composition measurements. We have added the following to the introduction:

“Measurements of particulate mass concentrations and composition for PM<sub>2.5</sub> and PM<sub>10</sub> have become routine through networks such as the U.S. Interagency Monitoring of Protected Visual Environments (IMPROVE) network (Malm et al., 2007), and these can be used to “reconstruct” aerosol optical properties (Malm and Hand, 2007). However, direct measurements of the optical properties of particles between different size regimes are much less common, and where they do exist are quite often made in the marine boundary layer (e.g. Bates et al., 2006) and not over land. (PM<sub>2.5</sub> and PM<sub>10</sub> refer to particulate matter with aerodynamic diameters below 2.5  $\mu\text{m}$  and 10  $\mu\text{m}$ , respectively.)”



“A previous analysis of particle size distributions measured during the CARES campaign indicated a large contribution of supermicron aerosol to the total particle scattering (Kassianov et al., 2012). Here, direct measurements of the scattering by these supermicron particles are reported on, and their sources and properties and the factors that drive their variability are examined.”

“Results from *in situ* measurements such as here can help to inform remote sensing retrievals and climatologies, which can provide a much broader spatial picture of sub- versus supermicron abundances and contributions to light scattering and extinction (Dubovik et al., 2002; Eck et al., 2010).”

2. Lines 156-157: “Data during the first week of the campaign (June 3-12) are especially noisy due to instrumental problems.” What caused the noise and were the measurements still accurate?

The noisy AMS data during the first week occurred because the AMS was inadvertently set wrong during the first week, with a very short MS-open duration and long MS-closed duration. This uneven open/closed cycle was the cause of noisier data (decreased precision) but did not affect quantification. The AMS was returned to normal setting of equal durations for MS open and MS closed mode June 16 onwards.

3. Section 2.2: What were the specific differences between the T0 and T1 site? Were the HR-AMS instruments operated by the same research group? Do the different OOA mass factors represent true aerosol composition differences between the sites?

There are many differences in location, available instrumentation and operators between the T0 and T1 sites. All of these differences are detailed in the “Overview of the 2010 Carbonaceous Aerosols and Radiative Effects Study (CARES)” by Zaveri et al. (2012), which is referenced in the overview of the Experimental section. As specified in Zaveri et al. (2012), the HR-ToF-AMS was operated by Qi Zhang’s group from UC Davis at the T1 site and by Chen Song and Rahul Zaveri’s group from Pacific Northwest National Laboratory at the T0 site. Regardless, OOA never represents “true” aerosol composition differences, only a mathematical representation of those differences that has some physical/chemical interpretation. However, the reviewer is most likely asking about comparability between OOA from the two sites. The HR-AMS measurements from T0 and T1 are discussed at length in Setyan et al. (2014), and thus rather than repeating those results here, we refer the reader to that work for more details. But the short answer is “yes, the differences in OOA factors are meaningful.”

4. Section 3.1: Besides Kassianov et al. (2012), what have prior studies of supermicron aerosol extinction under relatively clean conditions observed?

To be clear, Kassianov et al. (2012) calculated supermicron aerosol extinction from size distributions, while in the current study we actually report on measurements of the scattering, absorption and extinction by the supermicron particles in this region. As we now note in the introduction, direct measurements of supermicron optical properties are fairly uncommon, and where they do exist are most often found for the marine boundary layer where the contribution of sea spray will be large. We have focused our revisions on studies in which optical properties

were measured (either *in situ* or remote sensing) and not considered measurements of particulate mass concentrations alone. To this end, we have added an extensive comparison with some remote sensing results that look at the relationship between Angstrom exponents and the fine mode fraction of extinction, and that look at the relationship between the SSA and the fine mode fraction of extinction. We have added two new figures in support, one in the supplemental and one in the main text.

The added text and figures are provided below.

“Clarke and Kapustin (2010), in a survey of hemispheric aerosol vertical profiles, used a value of  $SAE_{450,550} = 1.3$  as a dividing line between air masses impacted by smaller particles from combustion sources ( $SAE_{450,550} > 1.3$ ) or coarse-mode particles, such as sea salt and dust ( $SAE_{450,550} < 1.3$ ). Our results indicate that  $SAE_{450,550,PM10} = 1.3$  corresponds to  $f_{sca,550,PM1} = 0.50$ , suggesting that  $SAE_{450,550} = 1.3$  is a reasonable dividing line between sub- and supermicron aerosol. They also observed that the relative magnitudes of scattering by smaller versus larger particles was highly variable, depending on altitude and region.”

“However, a better property to compare with remote sensing methods may be the  $PM_{10}$  extinction Ångstrom exponent ( $EAE_{PM10}$ ) versus the  $PM_1$  extinction fraction,  $f_{ext,PM1}$ . This is complementary to the  $SAE_{PM10}$  versus  $f_{sca,PM1}$  relationship discussed above, but focuses on the total optical losses (scattering plus absorption) as opposed to just scattering. The  $EAE_{PM10}$  and  $f_{ext,PM1}$  values (for the various wavelength combinations) also exhibit reasonably linear relationships (Fig. SX). The  $EAE_{PM10}$  value when  $f_{ext,PM1} = 0.5$  is used here as a reference point (referred to here as  $EAE_{PM10-50}$ ). For a given  $EAE_{PM10}$  wavelength pair the  $EAE_{PM10-50}$  increases notably as the wavelength for  $f_{ext,PM1}$  increases, exhibiting much less sensitivity to the choice of wavelength pair (although generally decreasing as the wavelength pairs increase) (Table SX). For example, for  $EAE_{450,700,PM10}$  the  $EAE_{PM10-50}$  increases from 0.85 to 1.09 to 1.37 for  $f_{ext,PM1,450}$  to  $f_{ext,PM1,550}$  to  $f_{ext,PM1,700}$ . The  $EAE_{PM10}$  versus  $f_{ext,PM1}$  relationships from these *in situ* measurements can be compared with remote sensing retrievals of the wavelength dependence of the AOD and the “fine mode fraction” (*FMF*) of AOD, which is nominally the same as the  $f_{ext,PM1}$  values here. As one example, Eck et al. (2010) investigated the relationship between the *FMF* of AOD and *EAE* from AERONET AOD measurements for a few locations around the world. The Eck et al. (2010) observations suggest  $EAE_{440-870,PM10-50} \sim 0.5$  at 440 nm and  $EAE_{440-870-50} \sim 0.9$  at 675 nm. These are somewhat smaller than what is observed here, although given the wavelength differences between the *in situ* and remote sensing measurements the difference is not unreasonable. Some of the difference in the  $EAE_{PM10-50}$  values could be attributable to differences in absorption by non-BC species in the regions studied in Eck et al. (2010) (India, China, West Africa) versus in the Sacramento region.”

“The relationship between the  $PM_{10}$  SSA and the  $PM_1$  fraction of extinction can also be examined to understand how particle size relates to the extent of scattering versus absorption. At T0, the  $SSA_{PM10}$  at all three wavelengths decreases as  $f_{ext,PM1,700}$  increases for  $f_{ext,PM1,700} < 0.7$ , at which point the trend reverses and  $SSA_{PM10}$  increases with  $f_{ext,PM1,700}$ . At T1, the relationship is somewhat different, with  $SSA_{PM10}$  decreasing with  $f_{ext,PM1,700}$  until about  $f_{ext,PM1,700} = 0.55$ , above which the SSA is relatively constant. The decrease in  $SSA_{PM10}$  with  $f_{ext,PM1}$  below some value can

be understood as resulting from an increasing contribution of absorbing black carbon as  $PM_{10}$  comes to dominate the extinction, and limited absorption by the supermicron particles at all wavelengths. The increase at T0 above  $f_{ext,PM_{10},700}$  can be understood as an increase in the contribution of local, photochemical production of secondary inorganic and organic aerosol within the submicron size range. At T1, the flat relationship above  $f_{ext,PM_{10},700}$  likely results from a dampening of the local BC impact as air masses travel from T0 to T1. When  $f_{ext,PM_{10},700}$  is small (supermicron dominated) the  $SSA_{PM_{10}}$  increases very slightly with wavelength (i.e.  $SSA_{PM_{10},700} > SSA_{PM_{10},450}$ ), but as  $f_{ext,PM_{10},700}$  increases the trend is reversed and the differences between wavelengths become larger. This demonstrates that the SSA versus wavelength relationship is fundamentally different between the sub- and supermicron particles in this region. These relationships can also be compared with results from remote sensing, specifically from AERONET (Eck et al., 2010). (Note that SSA from AERONET retrievals are limited to periods when the AOD is  $> 0.4$  at 440 nm, which is generally during high-concentration periods (Dubovik and King, 2000). AERONET AOD measurements (<http://aeronet.gsfc.nasa.gov/>) are available from the nearby McClellan Air Force Base from June 8-12, 2010, overlapping the CARES study period. During these days, the maximum  $AOD_{440nm}$  (for Level 2 data) was  $\sim 0.20$ , below the SSA retrieval threshold.) The shape of the observed  $SSA_{PM_{10}}$  versus  $f_{ext,PM_{10},700}$  curves at T0 are quite similar to that observed by AERONET for  $SSA_{675}$  versus  $FMF_{675}$  over India (Kanpur) and China (Beijing). However, the  $SSA_{440}$  versus  $FMF_{675}$  curves from AERONET over these same locations was much flatter than observed here for  $SSA_{PM_{10},450}$ . This could reflect differences in the nature of the supermicron particles between these regions and Sacramento, with apparently higher absorption by supermicron particles at shorter wavelengths in India and China leading to a weaker dependence of  $SSA_{440}$  on particle size than observed here.”

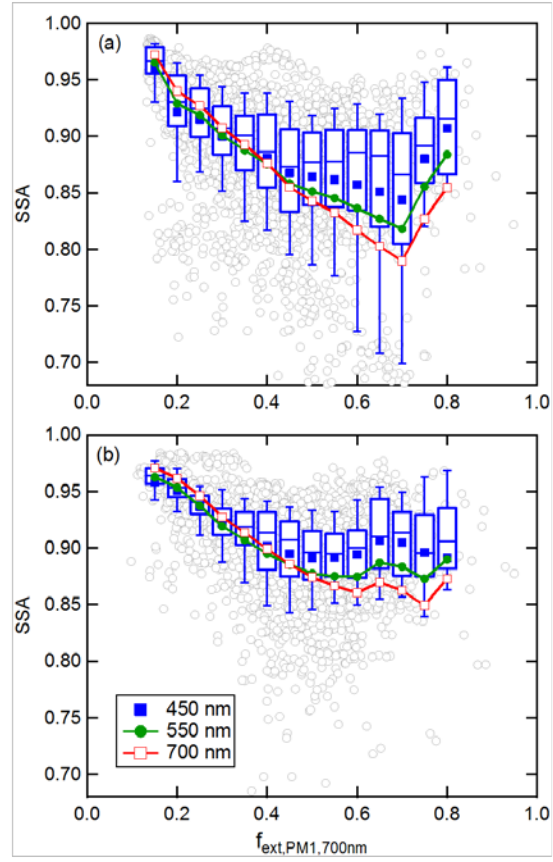


**Figure 4.** Relationship between the PM<sub>10</sub> SSA and the PM<sub>1</sub> fraction of extinction at 700 nm,  $f_{\text{ext},\text{PM1},700}$ , for the (a) T0 and (b) T1 sites. The individual data points (gray, circles) are shown for the  $\text{SSA}_{\text{PM10}}$  at 450 nm along with a box-and-whisker plot binned by  $f_{\text{ext},\text{PM1},700}$ . For the  $\text{SSA}_{\text{PM10}}$  at 550 nm (green line) and 700 nm (red line) only the mean, binned values are shown.

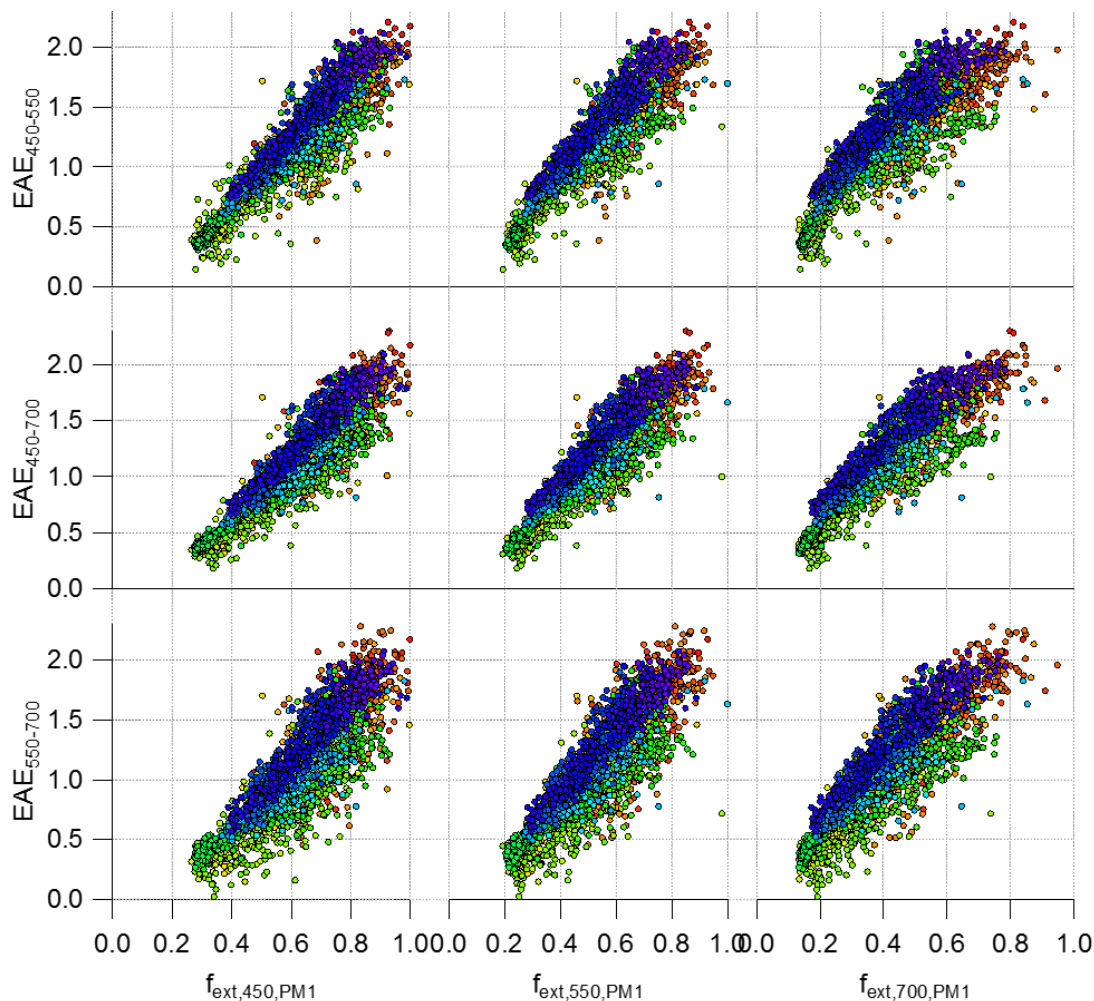


**Figure S6.** The relationship between the extinction Ångström exponent for PM<sub>10</sub> for different wavelength pairs and the PM<sub>1</sub>/PM<sub>10</sub> scattering ratio at different wavelengths for the T0 site. The points are colored according to time during the campaign, as in Figure S4. The  $EAE$  values when  $f_{\text{ext},\text{PM1}} = 0.5$  are reported in Table S3.

*Minor comments:*

Line 129: Give model and manufacturer for SMPS.

Done.

Line 176: What is the part number of the NO<sub>x</sub> chemiluminescence instrument?

We now give further information about the operation of the instrument, specifically stating “Gas-phase concentrations of the sum of NO and NO<sub>2</sub> (= NO<sub>x</sub>) and the sum of nitrogen oxides (= NO<sub>y</sub>) were measured using a 2-channel chemiluminescence instrument (Air Quality Design, Inc, High Performance, 2-Channel) in which NO<sub>2</sub> is photolyzed to NO *using a blue light photolytic converter* and NO<sub>y</sub> is converted to NO on a Mo catalyst,” and where the new text is in italics.

*Typographic corrections:*

Line 32: "... but the there is some" - [done](#)

Line 79: Use SI units. - [done](#)

Lines 99,125, 203, 205: Remove comma after June - [done](#)

Line 157: This is a very long week. – [We now indicate this is a week and a half](#)

## **References:**

Bates, T. S., Anderson, T. L., Baynard, T., Bond, T., Boucher, O., Carmichael, G., Clarke, A., Erlick, C., Guo, H., Horowitz, L., Howell, S., Kulkarni, S., Maring, H., McComiskey, A., Middlebrook, A., Noone, K., O'Dowd, C. D., Ogren, J., Penner, J., Quinn, P. K., Ravishankara, A. R., Savoie, D. L., Schwartz, S. E., Shinozuka, Y., Tang, Y., Weber, R. J., and Wu, Y.: Aerosol direct radiative effects over the northwest Atlantic, northwest Pacific, and North Indian Oceans: estimates based on in-situ chemical and optical measurements and chemical transport modeling, *Atmos. Chem. Phys.*, 6, 1657-1732, doi:10.5194/acp-6-1657-2006, 2006.

Clarke, A. and Kapustin, V.: Hemispheric Aerosol Vertical Profiles: Anthropogenic Impacts on Optical Depth and Cloud Nuclei, 329, 1488-1492, doi:10.1126/science.1188838, 2010.

Dubovik, O., Holben, B., Eck, T. F., Smirnov, A., Kaufman, Y. J., King, M. D., Tanre, D., and Slutsker, I.: Variability of absorption and optical properties of key aerosol types observed in worldwide locations, *J. Atmos. Sci.*, 59, 590-608, 2002.

Dubovik, O. and King, M. D.: A flexible inversion algorithm for retrieval of aerosol optical properties from Sun and sky radiance measurements, 105, 20673-20696, doi:10.1029/2000JD900282, 2000.

Eck, T. F., Holben, B. N., Sinyuk, A., Pinker, R. T., Goloub, P., Chen, H., Chatenet, B., Li, Z., Singh, R. P., Tripathi, S. N., Reid, J. S., Giles, D. M., Dubovik, O., O'Neill, N. T., Smirnov, A., Wang, P., and Xia, X.: Climatological aspects of the optical properties of fine/coarse mode aerosol mixtures, 115, D19205, doi:10.1029/2010JD014002, 2010.

Kassianov, E., Pekour, M., and Barnard, J.: Aerosols in central California: Unexpectedly large contribution of coarse mode to aerosol radiative forcing, *Geophys. Res. Lett.*, 39, L20806, doi:10.1029/2012GL053469, 2012.

Malm, W. C. and Hand, J. L.: An examination of the physical and optical properties of aerosols collected in the IMPROVE program, *Atmos. Environ.*, 41, 3407-3427, doi:10.1016/j.atmosenv.2006.12.012, 2007.

Malm, W. C., Pitchford, M. L., McDade, C., and Ashbaugh, L. L.: Coarse particle speciation at selected locations in the rural continental United States, *Atmos. Environ.*, 41, 2225-2239, doi:10.1016/j.atmosenv.2006.10.077, 2007.

Zaveri, R. A., Shaw, W. J., Cziczo, D. J., Schmid, B., Ferrare, R. A., Alexander, M. L., Alexandrov, M., Alvarez, R. J., Arnott, W. P., Atkinson, D. B., Baidar, S., Banta, R. M., Barnard, J. C., Beranek, J., Berg, L. K., Brechtel, F., Brewer, W. A., Cahill, J. F., Cairns, B., Cappa, C. D., Chand, D., China, S., Comstock, J. M., Dubey, M. K., Easter, R. C., Erickson, M.

H., Fast, J. D., Floerchinger, C., Flowers, B. A., Fortner, E., Gaffney, J. S., Gilles, M. K., Gorkowski, K., Gustafson, W. I., Gyawali, M., Hair, J., Hardesty, R. M., Harworth, J. W., Herndon, S., Hiranuma, N., Hostetler, C., Hubbe, J. M., Jayne, J. T., Jeong, H., Jobson, B. T., Kassianov, E. I., Kleinman, L. I., Kluzek, C., Knighton, B., Kolesar, K. R., Kuang, C., Kubátová, A., Langford, A. O., Laskin, A., Laulainen, N., Marchbanks, R. D., Mazzoleni, C., Mei, F., Moffet, R. C., Nelson, D., Obland, M. D., Oetjen, H., Onasch, T. B., Ortega, I., Ottaviani, M., Pekour, M., Prather, K. A., Radney, J. G., Rogers, R. R., Sandberg, S. P., Sedlacek, A., Senff, C. J., Senum, G., Setyan, A., Shilling, J. E., Shrivastava, M., Song, C., Springston, S. R., Subramanian, R., Suski, K., Tomlinson, J., Volkamer, R., Wallace, H. W., Wang, J., Weickmann, A. M., Worsnop, D. R., Yu, X. Y., Zelenyuk, A., and Zhang, Q.: Overview of the 2010 Carbonaceous Aerosols and Radiative Effects Study (CARES), *Atmos. Chem. Phys.*, 12, 7647-7687, doi:10.5194/acp-12-7647-2012, 2012.

# Understanding the Optical Properties of Ambient

## Sub- and Supermicron Particulate Matter: Results from

## the CARES 2010 Field Study in Northern California

Christopher D. Cappa<sup>1,\*</sup>, Kathryn R. Kolesar<sup>1,+</sup>, Xiaolu Zhang<sup>1</sup>, Dean B. Atkinson<sup>2</sup>, Mikhail S. Pekour<sup>3</sup>,  
Rahul A. Zaveri<sup>3</sup>, Alla Zelenyuk-Imre<sup>3</sup>, Qi Zhang<sup>4</sup>

<sup>1</sup> Department of Civil and Environmental Engineering, University of California, Davis, CA 95616, USA

<sup>2</sup> Department of Chemistry, Portland State University, Portland, OR, 92707, USA

<sup>3</sup> Atmospheric Sciences & Global Change Division, Pacific Northwest National Laboratory, Richland,  
WA, 99352, USA

<sup>4</sup> Department of Environmental Toxicology, University of California, Davis, CA 95616, USA

<sup>+</sup> Now at Department of Chemistry, University of Michigan, Ann Arbor, MI 48109, USA

\*Correspondence to: Christopher D. Cappa ([cdcappa@ucdavis.edu](mailto:cdcappa@ucdavis.edu))

### Short Summary

One way in which particles impact the solar radiation budget is through absorption and scattering of solar radiation. Here, we report on measurements of aerosol optical properties at visible wavelengths in the Sacramento, CA region and characterize their relationships with and dependence upon particle composition, particle size, photochemical ageing, water uptake and heating.

### Abstract

Measurements of the optical properties (absorption, scattering and extinction) of PM<sub>1</sub>, PM<sub>2.5</sub> and PM<sub>10</sub> made at two sites around Sacramento, CA during the June 2010 Carbonaceous Aerosols and Radiative Effects Study (CARES) are reported. These observations are used to establish relationships



22 between various intensive optical properties and to derive information about the dependence of the optical  
 23 properties on photochemical ageing and sources. Supermicron particles contributed substantially to the  
 24 total light scattering at both sites, about 50% on average. A strong, linear relationship is observed between  
 25 the scattering Ångstrom exponent for PM<sub>10</sub> and the fraction of the scattering that is contributed by  
 26 submicron particles ( $f_{\text{sca,PM1}}$ ) at both sites and with similar slopes and intercepts (for a given pair of  
 27 wavelengths), suggesting that the derived relationship may be generally applicable for understanding  
 28 variations in particle size distributions from remote sensing measurements. At the more urban T0 site, the  
 29  $f_{\text{sca,PM1}}$  increased with photochemical age whereas at the downwind, more rural T1 site the  $f_{\text{sca,PM1}}$   
 30 decreased slightly with photochemical age. This difference in behavior reflects differences in transport,  
 31 local production and local emission of supermicron particles between the sites. Light absorption is  
 32 dominated by submicron particles, but there is some absorption by supermicron particles (~15% of the  
 33 total). The supermicron absorption derives from a combination of black carbon that has penetrated into  
 34 the supermicron mode and from dust, and there is a clear increase in the mass absorption coefficient of  
 35 just the supermicron particles with increasing average particle size. The mass scattering coefficient (*MSC*)  
 36 for the supermicron particles was directly observed to vary inversely with the average particle size,  
 37 demonstrating that *MSC* cannot always be treated as a constant in estimating mass concentrations from  
 38 scattering measurements, or vice versa. The total particle backscatter fraction exhibited some dependence  
 39 upon the relative abundance of sub- versus supermicron particles, however this was modulated by  
 40 variations in the median size of particles within a given size range; variations in the submicron size  
 41 distribution had a particularly large influence on the observed backscatter efficiency and an approximate  
 42 method to account for this variability is introduced. The relationship between the absorption and scattering  
 43 Ångstrom exponents is examined and used to update a previously suggested particle classification  
 44 scheme. Differences in composition led to differences in the sensitivity of PM<sub>2.5</sub> to heating in a  
 45 thermodenuder to the average particle size, with more extensive evaporation (observed as a larger  
 46 decrease in the PM<sub>2.5</sub> extinction coefficient) corresponding to smaller particles, i.e. submicron particles  
 47 were generally more susceptible to heating than the supermicron particles. The influence of heating on  
 48 the particle hygroscopicity varied with the effective particle size, with larger changes observed when the  
 49 PM<sub>2.5</sub> distribution was dominated by smaller particles.

Deleted: the

Formatted: Font: Italic

Formatted: Font: Italic

## 1. Introduction

Atmospheric aerosol particles impact regional and global climate by scattering and absorbing solar radiation, as well as by affecting the properties of clouds, although the magnitude of these impacts remain uncertain (IPCC, 2013). The specific ability of particles to interact with solar radiation is dependent upon particle size, morphology and composition (Bohren and Huffman, 1983), which are often linked through variations in sources and chemical processing. Atmospheric particles span a wide range of sizes, from just a few nm to many microns. Quantitative understanding of the absolute and relative contributions across this entire size range is necessary to assess their climate impacts (Schwartz, 1996). The major sources of particles within the submicron and supermicron size regimes differ, with submicron particles generally deriving from combustion emissions and secondary formation and supermicron particles generally coming from mechanical action (e.g. wind-blown dust or ocean wave breaking) (Seinfeld and Pandis, 1998). As such, particle composition varies across this size range, as does the effectiveness with which particles absorb and scatter solar radiation. *In situ* measurements of the wavelength- and size-dependent light scattering and absorption properties of ambient atmospheric particles made concurrent with measurements of the size-dependent particle composition can provide insights into the impacts of particles on local climate and air quality (Anderson et al., 2003; Jung et al., 2009), as well as into the more general relationships between particle size, composition and radiative effects that determine their global impacts (Quinn et al., 2004; Bates et al., 2006; Wang et al., 2007; Garland et al., 2008; Gyawali et al., 2009; Yang et al., 2009). Such *in situ* measurements can help to interpret observations from remote sensing (Russell et al., 2010; Giles et al., 2012) and to provide observational constraints for results from simulations using regional and global models (Kaufman et al., 2002; Myhre et al., 2012; Tsigaridis et al., 2014). [Measurements of particulate mass concentrations and composition for PM<sub>2.5</sub> and PM<sub>10</sub> have become routine through networks such as the U.S. Interagency Monitoring of Protected Visual Environments \(IMPROVE\) network \(Malm et al., 2007\), and these can be used to “reconstruct” aerosol optical properties \(Malm and Hand, 2007\). However, direct measurements of the optical properties of particles between different size regimes are much less common, and where they do exist are quite often made in the marine boundary layer \(e.g. Bates et al., 2006\) and not over land. \(PM<sub>2.5</sub> and PM<sub>10</sub> refer to particulate matter with aerodynamic diameters below 2.5 µm and 10 µm, respectively.\)](#)

The US Department of Energy Carbonaceous Aerosols and Radiative Effects Study (CARES) took place in June 2010 with a motivation of improving our understanding of aerosol optical properties and how they evolve in the atmosphere through observations (Zaveri et al., 2012). Two heavily-instrumented ground observational sites were set up, one within the greater Sacramento, CA urban area and one

approximately 40 km to the northeast in much more rural Cool, CA ([Figure S1](#)). At both sites a variety of aerosol particle physical, chemical and optical property measurements were made. These two sites were chosen because of the generally reproducible wind patterns that, much of the time, bring air up from the San Francisco Bay Area (~~~160 km~~ SW) and past the Sacramento urban core before continuing up towards the foothills of the Sierra Nevada mountains where the air mass accumulates biogenic emissions during the day, with a reversed flow at night bringing more biogenically influenced air down from the mountains. In this way, comparison between the two sites facilitates understanding of the role that atmospheric photochemical processing plays in altering particle optical properties.

Results from measurements of dry particle light scattering and absorption made for submicron particulate matter (PM<sub>1</sub>) and for PM smaller than 10 µm (PM<sub>10</sub>) at both sites and of dry particle light absorption and extinction for PM smaller than 2.5 µm (PM<sub>2.5</sub>) at just the urban Sacramento site are reported in this study. The separate PM<sub>1</sub> and PM<sub>10</sub> measurements allow for determination of the optical properties of both submicron and supermicron (PM > 1 µm) particles. The distinct sub- and supermicron measurements are used here to characterize and examine the variability in their relative contributions as well as the differences between their properties and sources in the summertime Sacramento region. [A previous analysis of particle size distributions measured during the CARES campaign indicated a large contribution of supermicron aerosol to the total particle scattering](#) (Kassianov et al., 2012). [Here, direct measurements of the scattering by these supermicron particles are reported, and their sources and properties and the factors that drive their variability are examined.](#)

These regional results are also used to develop more general understanding of the size- and composition-dependent variability in aerosol particle optical properties. The analysis here focuses especially on quantifying and assessing the relationships between various intensive optical parameters (such as the scattering Ångström exponent, the absorption Ångström exponent, and the single scatter albedo) or between these parameters and characteristics of the particle distribution (such as the fine mode fraction or characteristic particle diameter) and how these differ between size ranges (sub- versus supermicron) or are influenced by photochemical ageing or heating. [Results from \*in situ\* measurements such as here can help to inform remote sensing retrievals and climatologies, which can provide a much broader spatial picture of sub- versus supermicron abundances and contributions to light scattering and extinction](#) (Dubovik et al., 2002; Eck et al., 2010).

Deleted: Figure S1

Deleted: 00 m

Deleted: i

Deleted: s

Formatted: Font: Italic

## 2. Experimental

All measurements were made during the 2010 CARES study, which took place in the Sacramento, CA region from 2-29 June, 2010. Measurements were made at one of two sites: one located in the greater Sacramento urban region (termed the T0 site) and one located ca. 40 km northeast downwind in Cool, CA (termed the T1 site), shown in [Figure S1](#). The CARES study has previously been described in detail (Fast et al., 2012; Zaveri et al., 2012), and only a brief overview is given here. A list of instrumentation used in this study is given in [Table 1](#), [an overview schematic of the sampling configuration in Figure S2](#), and [a list of abbreviations and symbols in Table S1](#).

Deleted: ,

Deleted: Figure S1

Deleted: Table 1

Formatted: Font: Not Bold

### 2.1 Measurements at the T0 Site

Particle light absorption coefficients ( $b_{\text{abs}}$ ) were measured using the UC Davis (UCD) photoacoustic spectrometer (PAS) at 405 nm and 532 nm (Lack et al., 2012) and using a particle soot absorption photometer (PSAP; Radiance Research, Inc.) at 470 nm, 532 nm and 660 nm (Bond et al., 1999; Virkkula et al., 2005). The PAS measured light absorption for  $\text{PM}_{2.5}$  sampled through a cyclone, alternating on a 2.5 or 5 minute time scale between bypass measurements (i.e. dried ambient particles) and measurements behind a constant-temperature (225°C) thermodenuder (Huffman et al., 2008; Cappa et al., 2012) with a residence time of 5 s. The PAS was calibrated before, during and after the study by referencing the observed photoacoustic response to added ozone to the extinction measured at the same wavelengths via cavity ringdown spectroscopy (CRDS) (Lack et al., 2012). The PSAP measured  $b_{\text{abs}}$  for  $\text{PM}_1$  or  $\text{PM}_{10}$  on an alternating 6 minute cycle. The PSAP was corrected for spot size, flow and particle scattering using standard methods (Bond et al., 1999; Ogren, 2010). Light scattering and backscattering coefficients ( $b_{\text{sca}}$  and  $b_{\text{bsca}}$ , respectively) were measured for dried particles using a three-wavelength total/backscatter nephelometer (TSI, Model 3563) at 450 nm, 550 nm and 700 nm. The nephelometer sampled  $\text{PM}_1$  and  $\text{PM}_{10}$  on the same alternating 6 minute cycle as the PSAP. The  $b_{\text{sca}}$  and  $b_{\text{bsca}}$  were corrected for truncation error (Anderson and Ogren, 1998). Light extinction coefficients ( $b_{\text{ext}} = b_{\text{abs}} + b_{\text{sca}}$ ) were directly measured for  $\text{PM}_{2.5}$  using the UCD aerosol CRDS (Langridge et al., 2011; Cappa et al., 2012). The  $b_{\text{ext}}$  were measured for dried particles at both 405 nm and 532 nm, and at 532 nm measurements were additionally made for particles exposed to elevated RH (~85%). [The air sample was humidified by passing it through a custom humidifier, which consisted of a semi-permeable capillary membrane \(Accurel\) that was kept continuously wetted. The relative humidity in the CRD cells was monitored using Vaisala RH probes \(HMP50\) that were calibrated using saturated salt solutions.](#) As with the UCD PAS, the CRDS operated behind a thermodenuder on a 2.5 or 5 minute cycle. [Measurements made through the thermodenuder were corrected for thermophoretic losses](#) (Huffman et al., 2008; Cappa et al., 2012). PSAP and nephelometer

Deleted: Active humidification

Deleted: was achieved

Deleted: the particles

Deleted: permeable membrane tube and the RH was

Deleted: with a

157 measurements were made over the period 3-28 June 2010, with a data gap from the period 16-20 June.  
158 The CRD measurements and PAS measurements at 405 nm were made starting 20:00 PDT on 16 June  
159 through 09:00 PDT on 29 June. Due to a laser malfunction, the PAS measurements at 532 nm started at  
160 12:00 PDT on 19 June. The thermodenuder measurements began at 12:00 PDT on 20 June.

Deleted: ,

161 Particle mobility diameter ( $d_{p,m}$ ) size distributions from 12.2 to 736.5 nm were measured using a  
162 scanning mobility particle sizer (SMPS; [TSI Model 3080](#)). Particle aerodynamic diameter ( $d_{p,a}$ ) size  
163 distributions from 542 nm to 19,810 nm were measured using an aerodynamic particle sizer (APS [TSI](#)  
164 [Model 3321](#)). The APS size distributions were converted to mobility-equivalent size distributions,  
165 assuming spherical particles and an [effective](#) particle material density of  $2.0 \text{ g cm}^{-3}$  and accounting for  
166 the Cunningham slip correction (DeCarlo et al., 2004). The use of an [effective](#) material density of  $2.0 \text{ g}$   
167  $\text{cm}^{-3}$  implicitly assumes that the larger particles characterized by the APS were primarily dust or sea spray.  
168 The resulting APS distribution was merged with the SMPS distribution to generate a time-series of the  
169 mobility size distributions with sizes over the entire range (12.2-19,810 nm). Because the  $\text{PM}_{10}$ ,  $\text{PM}_{2.5}$  and  
170  $\text{PM}_{10}$  designations are associated with aerodynamic diameters, mobility equivalent cut-diameters must be  
171 determined. The mobility equivalent cut-diameters are (assuming a density of  $2 \text{ g cm}^{-3}$ ) [approximately](#)  
172 700 nm, 1750 nm and 7200 nm, respectively. (For simplicity, we will continue to refer to the sub and  
173 supermicron particle ranges based on the aerodynamic size.) The merged size distribution was truncated  
174 to an upper limit of 7200 nm, and the campaign average for the T0 site is shown for reference in [Figure](#)  
175 [S3](#). One complication at the T0 site is that the APS did not collect data from 13:30 PDT on June 22  
176 onwards, and thus information about the supermicron particle size distribution and mass concentrations  
177 are not available after this date.

Deleted: Figure S2

178 Particle composition was monitored at T0 using the single particle laser ablation time-of-flight mass  
179 spectrometer (SPLAT-II) from 3-28 June (Zelenyuk et al., 2009). SPLAT-II characterizes the composition  
180 of individual particles and can be used to build a statistical picture of the distribution of particle types, as  
181 defined by the uniqueness of and similarities between their mass spectra (Zelenyuk et al., 2008). Analysis  
182 of the single particle mass spectra from SPLAT-II indicate a diversity of particle types, including dust,  
183 sea salt-containing (SS), combustion derived (including particles categorized as soot, biomass burning  
184 (BB), primary organic (POA) and hydrocarbon (HC)), amine-containing, and mixed sulfate/organic.  
185 SPLAT-II samples particles between  $\sim 50 \text{ nm}$  and  $2 \text{ }\mu\text{m}$ , although the sampling efficiency varies with  
186 particle size and with particle shape. SPLAT-II is optimized for particles with vacuum aerodynamic  
187 diameters ( $d_{va}$ ) between 100 and 600 nm, and detects larger particles with reduced relative efficiency.

Non-refractory submicron particulate matter (NR-PM) composition was measured using an Aerodyne high resolution time-of-flight aerosol mass spectrometer (HR-AMS) (Canagaratna et al., 2007). The NR-PM components measured include organics, sulfate, nitrate, ammonium and chloride. Data during the first week and a half of the campaign (June 3-12) are especially noisy due to instrumental problems. The AMS data were processed and NR-PM concentrations determined using standard methods, assuming a collection efficiency of 50%. Positive matrix factorization was applied to the dataset (Zhang et al., 2011) and three factors associated with the organic aerosol (OA) were determined. One of these was characterized as a more-oxidized OA factor (OOA) while two were characterized as less-oxidized OA factors, which were most likely cooking- and traffic-related and will be collectively referred to here as the hydrocarbon-like OA factor (HOA) and (Atkinson et al., 2015). Black carbon mass concentrations were measured with a single particle soot photometer (SP2; DMT) (Schwarz et al., 2006). The SP2 was calibrated using mobility size selected Aquadag particles, using a size-dependent particle density (Gysel et al., 2011). The reported concentrations have been multiplied by a factor of 1.53 to account for the difference in sensitivity of the SP2 to Aquadag compared with fullerene soot (R. Subramanian, Personal Communication), which is thought to be a reasonable proxy for diesel soot (Laborde et al., 2012a). This adjustment factor was determined from laboratory studies conducted after the CARES campaign. The CARES SP2 instruments measured BC-containing particles with volume equivalent core diameters between 30 and 400 nm, although quantification below  $d_{p,ved} \sim 100$  nm becomes generally more challenging and can vary between instruments (Laborde et al., 2012b). No adjustment of the reported concentrations for black carbon containing particles outside of the SP2 detection size range has been made, thus the reported concentrations may be underestimated (Cappa et al., 2014).

Deleted: particle

Deleted: will be referred to here as the hydrocarbon-like OA factor (HOA) and

Gas-phase concentrations of the sum of NO and NO<sub>2</sub> (= NO<sub>x</sub>) and the sum of all nitrogen oxides (= NO<sub>y</sub>) were measured using a 2-channel chemiluminescence instrument (Air Quality Design, Inc. High Performance, 2-Channel) in which NO<sub>2</sub> is photolyzed to NO using a blue light photolytic converter and NO<sub>y</sub> is converted to NO on a Mo catalyst. Gas-phase concentrations of hydrocarbons, in particular of toluene and benzene, were measured using a proton transfer reaction mass spectrometer (PTR-MS). These measurements can be used to estimate the average photochemical age (*PCA*) of the air mass (Roberts et al., 1984), with:

$$PCA_{NOx} = -\frac{1}{k_{rxn}[OH]} \ln \left( \frac{[NO_x]}{[NO_y]} \right) \quad (1)$$

where  $k_{\text{rxn}}$  is the reaction rate coefficient for the OH + NO<sub>2</sub> reaction ( $7.9 \times 10^{-12} \text{ cm}^3 \text{ molecules}^{-1} \text{ s}^{-1}$ ; (Brown et al., 1999)), and

$$PCA_{HC} = \frac{\ln(ER) - \ln\left(\frac{[\text{benzene}]}{[\text{toluene}]}\right)}{(k_b - k_t)[OH]} \quad (2)$$

where  $ER$  is the emission ratio between benzene and toluene, assumed here to be 3.2 (Warneke et al., 2007), and  $k_b$  and  $k_t$  are the reaction rate coefficients for reaction of benzene ( $1 \times 10^{-12} \text{ cm}^3 \text{ molecule}^{-1} \text{ s}^{-1}$ ) and toluene ( $5.7 \times 10^{-12} \text{ cm}^3 \text{ molecule}^{-1} \text{ s}^{-1}$ ) with OH, respectively (Atkinson et al., 2006). Although there are challenges in interpreting  $PCA$  estimates quantitatively due to e.g. mixing of different sources (Parrish et al., 2007) and weekend/weekday differences (Warneke et al., 2013),  $PCA$  nonetheless provides a useful estimate of the extent of photochemical processing.

## 2.2. Measurements at the T1 Site

A similar suite of measurements were made at the T1 site as at the T0 site, including light absorption at 470, 532, 660 nm by PSAP, light scattering at 450, 550, 700 nm by nephelometer, particle size by SMPS and APS and submicron particle composition by HR-AMS and SP2. The SMPS deployed at T1 (described in Setyan et al. (2014)) measures particle number distribution in the range of 10 – 858 nm in  $d_{p,m}$ . Analysis of the HR-AMS data using positive matrix factorization identified two distinct OOA factors, one of which was mainly associated with biogenic emissions and the other representative of secondary organic aerosol (SOA) formed in photochemically processed urban emissions. HOA was also observed at T1 but it on average accounted for only ~10% of the OA mass. Details on HR-AMS and SMPS measurements at T1 and associated data analysis are given in Setyan et al. (2012) and Setyan et al. (2014). The particle scattering and absorption measurements were made nearly continuously from 3-28 June, 2010. Light absorption measurements were also made using different PAS instruments, although these are not utilized here. PTR-MS measurements of toluene and benzene are available from 3-28 June, 2010. Although NO and NO<sub>y</sub> measurements were made, NO<sub>x</sub> was not measured. Thus, it is only possible to estimate  $PCA$  at the T1 site using the benzene-toluene method (Equation 2).

One additional way in which particle composition was characterized at T1 was with a particle ablation laser-desorption mass spectrometer (PALMS) (Cziczo et al., 2006). The PALMS is similar to the SPLAT-II in that single particle mass spectra are collected for particles between about  $d_{p,a}$  150 nm and 2

Formatted: Not Highlight

Deleted: ,

Deleted: ,

254  $\mu\text{m}$ , which are used to build a statistical picture of particle types. Analysis of the single particle mass  
 255 spectra from PALMS at the T1 site yielded the following particle types: dust (termed MinMet for  
 256 mineralogical/meteoritic), sea salt-containing (SS), combustion derived (including particles categorized as  
 257 soot, biomass burning (BB), or oil), mixed sulfate/organic and “other.” Results from the PALMS  
 258 measurements have been previously reported in Zaveri et al. (2012).

### 259 **2.3 Derived particle properties**

260 Using the alternating (i.e. sequential)  $\text{PM}_1$  and  $\text{PM}_{10}$  measurements, the properties of supermicron  
 261 particles specifically have been estimated from the difference between  $\text{PM}_{10}$  and  $\text{PM}_1$ , with

$$262 \quad b_{x,\text{super}} = \frac{b_{x,\text{PM}_{10}}(t-1) + b_{x,\text{PM}_{10}}(t+1)}{2} - b_{x,\text{PM}_1}(t) \quad (3)$$

263 where  $x$  indicates absorption or scattering and where the  $t$  values indicate the average concentration over  
 264 each 6 min averaging period (i.e. the  $\text{PM}_1$ - $\text{PM}_{10}$  cycle time). The fraction of absorption or scattering from  
 265  $\text{PM}_1$  or supermicron PM is therefore defined as:

$$266 \quad f_{x,\text{PM}_1} = \frac{b_{x,\text{PM}_1}}{b_{x,\text{PM}_{10}}} \quad (4a)$$

$$267 \quad f_{x,\text{super}} = \frac{b_{x,\text{super}}}{b_{x,\text{PM}_{10}}} \quad (4b)$$

268 where  $x$  again indicates absorption or scattering. These ratios give an indication of the contribution of  
 269 submicron or supermicron particles to the total absorption or scattering, e.g. larger values of  $f_{\text{sca},\text{PM}_1}$   
 270 indicate greater dominance of the submicron particle mode in terms of total scattering.

271 Light absorption measurements are used to determine the absorption Ångstrom exponent (AAE),  
 272 which characterizes the wavelength dependence of absorption and is given as:

$$273 \quad \text{AAE}_{\lambda_1,\lambda_2} = -\frac{\log\left(\frac{b_{\text{abs},\lambda_1}}{b_{\text{abs},\lambda_2}}\right)}{\log\left(\frac{\lambda_1}{\lambda_2}\right)} \quad (5)$$

274 where  $\lambda_1$  and  $\lambda_2$  indicate different wavelengths. It is often assumed that “pure” black carbon (BC)  
 275 particles have an AAE close to 1 and that values  $>1$  indicate the presence of light absorbing organics  
 276 (referred to as brown carbon, or BrC) or dust, which tend to exhibit absorption that increases sharply as  
 277 wavelength decreases (Lack and Cappa, 2010). The AAE is dependent upon the chosen wavelength pair.

278 The specific wavelength pair used to calculate AAE will be indicated using the notation  $\text{AAE}_{\lambda_1-\lambda_2}$ . A related  
 279 [property](#), the difference in the  $\text{PM}_{10}$  and  $\text{PM}_1$  AAE, can [then](#) be calculated:



$$\Delta AAE_{10-1} = AAE_{PM10} - AAE_{PM1} \quad (6)$$

The scattering Ångström exponent (*SAE*) is also commonly used to characterize the relative contributions from sub- and supermicron particles (Clarke and Kapustin, 2010), and is defined analogously to the *AAE* as:

$$SAE_{\lambda_1, \lambda_2} = - \frac{\log\left(\frac{b_{sca, \lambda_1}}{b_{sca, \lambda_2}}\right)}{\log\left(\frac{\lambda_1}{\lambda_2}\right)} \quad (7)$$

Larger values of the *SAE* correspond to overall smaller particles, and have been calculated for  $PM_{10}$ ,  $PM_{10}$  and  $PM_{super}$ . A similar parameter, the extinction Ångström exponent, *EAE*, can be calculated for  $PM_{2.5}$  using the measured  $b_{ext}$  [or for  \$PM\_{10}\$  or  \$PM\_{10}\$  using the sum of the  \$b\_{sca}\$  and  \$b\_{abs}\$](#) .

The fraction of extinction due to scattering is characterized through the single scatter albedo (*SSA*), which can be written in multiple ways depending on whether  $b_{ext}$ ,  $b_{abs}$  or  $b_{sca}$  were the directly measured properties:

$$SSA = \frac{b_{ext} - b_{abs}}{b_{ext}} = \frac{b_{sca}}{b_{ext}} = \frac{b_{sca}}{b_{sca} + b_{abs}} \quad (8)$$

The angular dependence of scattering is characterized through measurement of the backscatter coefficients,  $b_{bsca}$ . The fraction of light that is backscattered, relative to the total scattering, is calculated as

$$f_{bsca} = \frac{b_{bsca}}{b_{sca}} \quad (9)$$

The backscatter fraction is an important climate-relevant parameter as particle radiative effects depend in part on the extent to which incoming solar radiation is reflected back to space versus absorbed within the Earth system. The backscatter fraction is commonly converted to an asymmetry parameter,  $g_{sca}$ , and the empirically derived relationship between these is (Andrews et al., 2006):

$$g_{sca} = -7.143889 \cdot f_{bsca}^3 + 7.464439 \cdot f_{bsca}^2 - 3.9356 \cdot f_{bsca} + 0.9893 \quad (10)$$

The asymmetry parameter is the intensity-weighted average of the cosine of the scattering angle and ranges from -1 (all backscatter) to 1 (all forward scatter).

Using the measurements made behind the thermodenuder at the T0 site (i.e. the PAS and CRD measurements), various ratios and differences can be determined. The ratio between the denuded and

undened extinction (i.e. the fraction of extinction remaining for PM<sub>2.5</sub>) provides a measure of the particle volatility, with smaller values indicating more volatile particles:

$$f_{ext,TD} = \frac{b_{ext,TD}}{b_{ext,amb}} = \frac{b_{ext}(t-1)+b_{ext}(t+1)}{2b_{ext}(t)} \quad (11)$$

where *TD* indicates the thermodenuded and *amb* indicates the ambient time periods, and the 2<sup>nd</sup> equality shows how the sequential TD and ambient measurements were accounted for similar to Eqn. 3. The change in particle hygroscopicity upon thermodenuding is calculated as

$$\Delta\gamma_{RH} = \gamma_{RH,amb} - \gamma_{RH,TD} \quad (12)$$

where

$$\gamma_{RH} = \log\left(\frac{b_{ext,high}}{b_{ext,low}}\right) / \log\left(\frac{100-RH_{low}}{100-RH_{high}}\right) \quad (13)$$

and the *high* and *low* refer to the humidified and dried CRD measurements and again accounting for the sequential nature of the *TD* and *amb* measurements. The parameter  $\gamma_{RH}$  can be thought of as the optical hygroscopicity (i.e., a measure of the affinity of particles to take up water and grow), although it does have some dependence on particle size and thus there is not a 1-to-1 relationship between  $\gamma_{RH}$  and particle growth (Atkinson et al., 2015). In general, for a given amount of particle growth due to water uptake,  $\gamma_{RH}$  is larger for smaller particles.

The difference in the AAE between the ambient and thermodenuded states can also be determined:

$$\Delta AAE_{amb-TD} = AAE_{amb} - AAE_{TD} \quad (14)$$

Mass absorption, scattering and extinction coefficients (*MAC*, *MSC* and *MEC*, respectively) have been calculated for the various wavelengths and PM size ranges. Using scattering as an example,

$$MSC_X\left(\frac{m^2}{g}\right) = \frac{b_{sca}}{[X]} \quad (15)$$

where [X] is the mass concentration of the reference species of interest, such as BC or the total PM. In the case of [BC], the SP2 measurements are used. For total PM, the integrated volume concentrations were used to estimate [PM], assuming spherical particles. For supermicron particles it was assumed that  $\rho_p = 2.0 \text{ g cm}^{-3}$  and for submicron particles the density was  $1.3 \text{ g cm}^{-3}$  (Setyan et al., 2012).

The size distributions have been used to calculate median surface-weighted particle diameters ( $d_{p,surf}$ ) as:

Deleted: (amb)

Deleted: (TD)

Deleted: towards

Deleted: hygroscopicity

$$d_{p,surf} = \frac{\int_{d_{p,low}}^{d_{p,high}} d_p \frac{dN}{d \log d_p} d \log d_p}{\int_{d_{p,low}}^{d_{p,high}} \frac{dN}{d \log d_p} d \log d_p} \quad (16)$$

where  $dN/d \log d_p$  is the observed number-weighted size distribution over the size range of interest ( $d_{p,low}$  to  $d_{p,high}$ ). In this study,  $d_{p,surf}$  values have been separately calculated for the total  $PM_{10}$  distribution and for the supermicron particle range.

### 3. Results and Discussion

#### 3.1 Size dependence of optical properties

##### 3.1.1 Light scattering

Supermicron particles contributed substantially to the dry particle scattering at both T0 and T1 (Figure 1). The average  $f_{sca,PM1}(550 \text{ nm})$  at T0 was  $0.48 \pm 0.17 (1\sigma)$  and at T1 was  $0.55 \pm 0.16 (1\sigma)$ . (If the time period where the scattering measurements were not available at T0 is excluded from the T1 average, the average  $f_{sca,PM1}$  is  $0.57 \pm 0.15 (1\sigma)$ .) Thus, nearly 50% of the dry scattering at these two sites was, on average, due to supermicron particles during the campaign period. This observation is consistent with results from Kassianov et al. (2012), who calculated scattering and direct radiative forcing for these two sites (T0 and T1) based on observed size distributions and concluded that supermicron particles contribute substantially to the total scattering. Because scattering generally increases more rapidly with decreasing wavelength for small particles, the  $f_{sca,PM1}$  is larger for 450 nm ( $= 0.59$  at T0 and  $0.67$  at T1) and smaller for 700 nm ( $= 0.34$  at T0 and  $0.41$  at T1) compared to 550 nm. The similarity of the  $f_{sca,PM1}$  values between the two sites is noteworthy given that the T0 site is situated much closer to urban Sacramento than is the T1 site. The  $f_{sca,PM1}$  values at the two sites show a strong, linear correlation with the  $SAE_{450,550,PM10}$  (Figure 2a,b), which is not entirely surprising since the SAE provides an indication of the mean, optically-weighted particle size. There is a similarly strong relationship with the  $SAE_{PM10}$  values calculated from the other wavelength pairs (Figure S4 and Figure S5 show results for the T0 and T1 sites, respectively, for comparison). The best fit from a one-sided linear fit to  $SAE_{450,550,PM10}$  versus  $f_{sca,PM1}$  at T0 is  $SAE_{450,550,PM10} = 2.69 f_{sca,550,PM1} - 0.05$  ( $r^2 = 0.88$ ) and at T1 is  $SAE_{450,550} = 2.66 f_{sca,550,PM1} + 0.06$  ( $r^2 = 0.91$ ). (Values for other combinations of wavelengths for T0 and T1 are reported in Table S2.) Clarke and Kapustin (2010), in a survey of hemispheric aerosol vertical profiles, used a value of  $SAE_{450,550} = 1.3$  as a dividing line between air masses impacted by smaller particles from combustion sources ( $SAE_{450,550} > 1.3$ ) or coarse-mode particles, such as sea salt and dust ( $SAE_{450,550} < 1.3$ ). Our results indicate that  $SAE_{450,550,PM10} = 1.3$  corresponds to  $f_{sca,550,PM1} = 0.50$ , suggesting that  $SAE_{450,550} = 1.3$  is a reasonable

Formatted: Font: Not Bold

Deleted: Figure 1

Formatted: Font: Not Bold

Formatted: Font: Not Bold

Deleted: Figure 2

Deleted: Figure S3

Deleted: Figure S4

Deleted: S1

dividing line between sub- and supermicron aerosol. They also observed that the relative magnitudes of scattering by smaller versus larger particles was highly variable, depending on altitude and region.

Although the  $SAE_{PM10}$  values exhibit a linear relationship with  $f_{sca,PM1}$ , they exhibit a more complex relationship with the median surface-area weighted particle diameter of the entire distribution ( $d_{p,surf,PM10}$ ). The  $SAE_{PM10}$  values generally decrease with increasing  $d_{p,surf,PM10}$ , as one might expect since an increase in  $d_{p,surf,PM10}$  presumably corresponds to an increase in the supermicron fraction of scattering. However, there is much greater scatter compared to the clear relationship with  $f_{sca,PM1}$ , and clear periods when a monotonic relationship is not observed (Figure 2c,d). The derived  $d_{p,surf,PM10}$  values are sensitive to the exact shapes of the sub- and supermicron modes, and the  $MSC$  for supermicron particles, in particular, is also sensitive to the shape of the supermicron size distribution (discussed further below in Section 3.1.2). Consequently, there is not a straight-forward relationship between the  $SAE_{PM10}$  and  $d_{p,surf,PM10}$  and the  $SAE_{PM10}$  cannot be used to predict average properties of the overall sub- plus supermicron size distribution. However, the strong, linear relationship between the  $SAE_{PM10}$  and  $f_{sca,PM1}$  and the close correspondence between the two sites, despite apparent variations in the underlying size distributions, suggests that the relationships derived here may be sufficiently general to be applied in other locations, although this needs to be verified. This in turn indicates that observations of  $SAE_{PM10}$  can be used to quantitatively estimate the fractional contribution of sub and supermicron particles to the total scattering with an uncertainty of  $\sim 15\%$  based on the spread in the data. Thus, the relationships derived here may be useful for application or comparison with remote sensing methods, such as the AERONET sun photometer network (Schuster et al., 2006; Eck et al., 2010) or satellites (Ginoux et al., 2012).

However, a better property to compare with remote sensing methods may be the  $PM_{10}$  extinction Ångstrom exponent ( $EAE_{PM10}$ ) versus the  $PM_{10}$  extinction fraction,  $f_{ext,PM1}$ . This is complementary to the  $SAE_{PM10}$  versus  $f_{sca,PM1}$  relationship discussed above, but focuses on the total optical losses (scattering plus absorption) as opposed to just scattering. The  $EAE_{PM10}$  and  $f_{ext,PM1}$  values (for the various wavelength combinations) also exhibit reasonably linear relationships (Figure S6). The  $EAE_{PM10}$  value when  $f_{ext,PM1} = 0.5$  is used here as a reference point (referred to here as  $EAE_{PM10-50}$ ). For a given  $EAE_{PM10}$  wavelength pair the  $EAE_{PM10-50}$  increases notably as the wavelength for  $f_{ext,PM1}$  increases, exhibiting much less sensitivity to the choice of wavelength pair although generally decreasing as the wavelength pairs increase (Table S3). For example, for  $EAE_{450,700,PM10}$  the  $EAE_{PM10-50}$  increases from 0.85 to 1.09 to 1.37 for  $f_{ext,PM1,450}$  to  $f_{ext,PM1,550}$  to  $f_{ext,PM1,700}$ . (Similar behavior is observed for the wavelength-sensitivity of the equivalently-defined  $SAE_{PM10-50}$ .) The  $EAE_{PM10}$  versus  $f_{ext,PM1}$  relationships from these *in situ* measurements can be compared with remote sensing retrievals of the wavelength dependence of the AOD

Deleted: Figure 2

Formatted: Font: Not Bold

Deleted:

Formatted: Not Highlight

Formatted: Not Highlight

(i.e. the *EAE*) and the “fine mode fraction” of AOD. The fine mode fraction of AOD is nominally equivalent to  $f_{\text{ext},\text{PM1}}$  here, and thus they can be directly compared. As one example, Eck et al. (2010) investigated the relationship between the fine mode fraction of AOD and *EAE* from AERONET AOD measurements for a few locations around the world. The Eck et al. (2010) observations suggest  $EAE_{440-870,\text{PM10-50}} \sim 0.5$  at 440 nm and  $EAE_{440-870-50} \sim 0.9$  at 675 nm. These are somewhat smaller than what is observed here, although given the wavelength differences between the *in situ* and remote sensing measurements the difference is not unreasonable. Some of the difference in the  $EAE_{\text{PM10-50}}$  values could be attributable to differences in absorption by non-BC species in the regions studied in Eck et al. (2010) (India, China, West Africa) versus in the Sacramento region.

One factor that can influence the sub- versus supermicron contributions to the total scattering is the extent of photochemical processing. Photochemical processing leads to the production of lower-volatility material that will tend to condense according to the particle Fuchs-corrected surface area. As such, photochemical processing and secondary PM formation, especially SOA, will lead to preferential growth of the submicron mode diameters (which grow more for a given amount of material condensed) and will lead to an increase in the submicron scattering in particular. The  $f_{\text{sca},\text{PM1}}$  at T0 exhibits a general increase with PCA (characterized by the  $[\text{NO}_x]/[\text{NO}_y]$  and/or  $[\text{benzene}]/[\text{toluene}]$  ratios), although there is a fair amount of scatter at low photochemical age (Figure 3a,b). The  $f_{\text{sca},\text{PM1}}$  at T1 shows completely different behavior, with  $f_{\text{sca},\text{PM1}}$  exhibiting very little dependence on PCA, although there is possibly a slight decrease (Figure 3c). There is generally good correspondence between the  $[\text{NO}_x]/[\text{NO}_y]$  and  $[\text{benzene}]/[\text{toluene}]$  ratios measured at T0, indicating that the different results at T1 are unlikely to result from use of a particular PCA marker (Figure 3d). The PCA at T1 is on average much larger than at T0. The PCA at the T0 site exhibits a clear peak around 15:00 PDT (Figure 3e). The PCA diel profile at T1 is comparably much broader and exhibits a less-pronounced peak, but that also occurs in the late afternoon (around 16:00 PDT) (Figure 3e). This broadening and different temporal dependence likely reflects the downwind location of the T1 site and the general flow patterns in this region (Fast et al., 2012). It seems likely that the difference in variation of the  $f_{\text{sca},\text{PM1}}$  with PCA between the two sites is related to these difference. At T0, the measured  $b_{\text{sca},\text{PM1}}$  may reflect a relatively local production of submicron particulate mass whereas at T1 the  $b_{\text{sca},\text{PM1}}$  is more reflective of regional conditions. The  $b_{\text{sca},\text{super}}$  at both sites will have some regional contribution (in particular sea spray), but also a strong local contribution. Wind speeds were typically largest in the mid- to late afternoon at both sites, although overall the diel behavior was much clearer at T1 than at T0 and with a larger amplitude (Figure 3e). However, the wind speeds were on average larger at T0. Thus, it seems reasonable to conclude that local emission of supermicron particulates, possibly re-suspended road dust or from agricultural sources, in the afternoon at T1

Deleted: condensable

Formatted: Font: Not Bold

Deleted: Figure 3

Formatted: Font: Not Bold

Deleted: Figure 3

Formatted: Font: Not Bold

Deleted: Figure 3

Formatted: Font: Not Bold

Deleted: Figure 3

Formatted: Font: Not Bold

Deleted: Figure 3

Formatted: Font: Not Bold

Deleted: Figure 3

counteracts the influence of growth of the regional submicron particulates, leading  $f_{\text{sca,PM1}}$  to be nearly independent of PCA at this site. In contrast, at T0 the local photochemical production of new submicron PM mass appears to be sufficiently strong to lead to an increase in  $f_{\text{sca,PM1}}$  with PCA.

The relationship between the  $\text{PM}_{10}$  SSA and the  $\text{PM}_1$  extinction fraction ( $f_{\text{ext,PM1}}$ ) can also be examined to understand how the extent of scattering versus absorption relates to particle size (Figure 4). At T0, the  $\text{SSA}_{\text{PM10}}$  at all three wavelengths decreases as  $f_{\text{ext,PM1,700}}$  increases for  $f_{\text{ext,PM1,700}} < 0.7$ , at which point the trend reverses and  $\text{SSA}_{\text{PM10}}$  increases with  $f_{\text{ext,PM1,700}}$ . (Similar behavior is observed when  $f_{\text{ext,PM10}}$  values at the other wavelengths are used. The choice of 700 nm was made to facilitate comparison with AERONET observations, below.) At T1, the relationship is somewhat different, with  $\text{SSA}_{\text{PM10}}$  decreasing with  $f_{\text{ext,PM1,700}}$  until about  $f_{\text{ext,PM1,700}} = 0.55$ , above which the SSA is relatively constant. The decrease in  $\text{SSA}_{\text{PM10}}$  with  $f_{\text{ext,PM1}}$  below some value can be understood as resulting from an increasing contribution of absorbing black carbon as  $\text{PM}_1$  comes to dominate the extinction, and limited absorption by the supermicron particles at all wavelengths. The increase at T0 above  $f_{\text{ext,PM1,700}} = 0.7$  can be understood as an increase in the contribution of local, photochemical production of secondary inorganic and organic aerosol within the submicron size range. At T1, the flat relationship above  $f_{\text{ext,PM1,700}} = 0.55$  likely results from a dampening of the local BC impact as air masses travel from T0 to T1. When  $f_{\text{ext,PM1,700}}$  is small (supermicron dominated) the  $\text{SSA}_{\text{PM10}}$  increases very slightly with wavelength (i.e.  $\text{SSA}_{\text{PM10,700}} > \text{SSA}_{\text{PM10,450}}$ ), but as  $f_{\text{ext,PM1,700}}$  increases the trend is reversed and the differences between wavelengths become larger. This demonstrates that the SSA versus wavelength relationship is fundamentally different between the sub- and supermicron particles in this region.

These relationships can also be compared with results from remote sensing. As above, we consider as an example measurements from AERONET (Eck et al., 2010). (Note that SSA from AERONET retrievals are limited to periods when the AOD is  $> 0.4$  at 440 nm, which is generally during high-concentration periods (Dubovik and King, 2000). AERONET AOD measurements (<http://aeronet.gsfc.nasa.gov/>) are available from the nearby McClellan Air Force Base from June 8-12, 2010, overlapping the CARES study period. During these days, the maximum  $\text{AOD}_{440\text{nm}}$  (for Level 2 data) was  $\sim 0.20$ , below the SSA retrieval threshold. Thus, we cannot compare our *in situ* measurements directly to AERONET measurements from the same location and time period.) The shape of the observed  $\text{SSA}_{\text{PM10}}$  versus  $f_{\text{ext,PM1,700}}$  curves at T0 are quite similar to that observed by AERONET for  $\text{SSA}_{675}$  versus the fine mode fraction of AOD at 675 nm over India (Kanpur) and China (Beijing). However, the  $\text{SSA}_{440}$  versus fine mode fraction of AOD at 675 nm curves from AERONET over these same locations was much flatter than observed here for  $\text{SSA}_{\text{PM10,450}}$  versus  $f_{\text{ext,PM1,700}}$ . This could reflect differences in the nature of the

Field Code Changed

Formatted: Font: Not Bold

Formatted: Font: Italic

supermicron particles between these regions and Sacramento, with apparently higher absorption by supermicron particles at shorter wavelengths in India and China leading to a weaker dependence of  $SSA_{440}$  on particle size than observed here.

### 3.1.2 Light absorption

Light absorption at both sites was dominated by submicron particles, although a small fraction may also be from supermicron particles (Figure 1). The average  $f_{abs,PM1}$  at 532 nm at T0 was  $0.89 \pm 0.14$  ( $1\sigma$ ) and at T1 was  $0.85 \pm 0.17$  ( $1\sigma$ ). At T1 there is a slight indication that  $f_{abs,super}$  decreased as  $f_{sca,super}$  decreased, but no such relationship is clearly evident at T0 (Figure 1g-h). Such potential relationships must be viewed with some amount of caution, as the PSAP requires correction for particle scattering and the extent of forward versus backward scattering is particle size dependent. It is also known that the PSAP shows an additional sensitivity to particle size due to differences in the depth of penetration of particles into the filter (Nakayama et al., 2010), which might influence the measurements here.

That light absorption is dominated by submicron particles suggests that black carbon, and possibly brown carbon, make up the majority of the light absorbing particle burden. The  $AAE_{PM1}$  values at both T0 and T1 exhibit reasonably normal distributions (Figure 5). The spread at T0 was substantially smaller than at T1. The average  $AAE_{PM1}$  values are slightly larger than unity at both sites ( $1.21 \pm 0.13$  and  $1.33 \pm 0.22$  for T0 and T1, respectively, where uncertainties are 1 standard deviation; Table 2), and do not show any pronounced dependence on the wavelength pair chosen. Black carbon is typically thought to have an  $AAE$  close to unity (Cross et al., 2010). The average  $PM1$   $AAE_{PM1,450-532}$  are identical between the sites, whereas the  $AAE_{PM1,450-660}$  and  $AAE_{PM1,532-660}$  are slightly larger at T1. The larger spread in the  $AAE_{PM1}$  values for all wavelength pairs at T1 suggests that the two PSAP instruments were not entirely identical and had somewhat different noise characteristics, making it difficult to establish whether these small differences are real. One method that has been used to estimate the contribution of brown carbon relative to black carbon is to extrapolate the observed  $b_{abs}$  at longer  $\lambda$  (e.g. 660 nm) to shorter wavelengths assuming that  $AAE = 1$  and that absorption by brown carbon at long  $\lambda$  is zero (Gyawali et al., 2009; Yang et al., 2009; Chung et al., 2012; Lack and Langridge, 2013). To the extent that this method is appropriate, and some have argued it may not be (Lack and Langridge, 2013), it provides an estimate of  $b_{abs}$  for pure BC (assuming that  $AAE_{BC} = 1$  exactly) and the contribution from brown carbon can then be estimated by subtracting the pure BC  $b_{abs}$  from the total. Given the observed  $AAE_{PM1}$  values, this spectral differencing method suggests that brown carbon contributes ~6% at T0 and up to 11% at T1 to submicron particle light absorption at 450 nm; if the actual  $AAE_{BC}$  were  $>1$ , as possibly suggested by the  $AAE_{532-660}$  measurements at both sites, then the attributed brown carbon fraction would be even smaller and cancelled out entirely

Deleted: Figure 1

Formatted: Font: Not Bold

Deleted: Figure 1

Formatted: Font: Not Bold

Formatted: Font: Not Bold

Deleted: Figure 4

§11 [if  \$AAE\_{BC}\$  equals the observed value for the ambient particles](#). These relatively minor contributions from  
§12 brown carbon are consistent with the conclusions of Cappa et al. (2012) and indicate that in this region  
§13 the summertime submicron particulate light absorption is predominately from black carbon.

§14 There are two likely origins of the supermicron absorption ([assuming it is not simply an artefact](#)):  
§15 penetration of BC into the supermicron size range, likely from coagulation of BC with larger particles or  
§16 tailing of the predominately submicron BC size distribution, or dust (assuming the observed supermicron  
§17 absorption is not simply an experimental artifact). Dust is known to contribute substantially to the  $PM_{10}$   
§18 burden in Sacramento, with sources including [local emissions from](#) roadways, agricultural activity and  
§19 disturbed open residential areas (California Air Resources Board, 2005;  
§20 <http://www.arb.ca.gov/pm/pmmeasures/pmch05/pmch05.htm>), [and](#) long range transport (Ewing et al.,  
§21 2010). The single particle measurements from the SPLAT-II instrument at T0 indicate that both BC-  
§22 containing and dust particles are observed in the supermicron size range, along with substantial  
§23 contributions from sea salt-containing particles that are likely of marine origin ([Figure S7](#)). The PALMS  
§24 instrument detected similar particle types at the T1 site (Zaveri et al., 2012). Although informative, these  
§25 measurements unfortunately cannot be used to quantitatively assess the relative contributions of the  
§26 different absorbing particle types to the supermicron absorption because both instruments sample only  
§27 over a subset of the entire supermicron size range, e.g. the SPLAT-II only up to  $d_{v,a} \sim 2 \mu m$ , [and matrix](#)  
§28 [effects can impact quantification of individual components in mixed particles \(e.g. BC mixed with dust\)](#).  
§29 Nonetheless, the single particle composition measurements provide support for [both](#) the likely origins of  
§30 the supermicron absorption being from either BC penetration or dust.

§31 Dust and BC should be distinguishable based on the observed spectral properties and chemical  
§32 composition. Although the optical properties of dust vary by location and source, dust is generally thought  
§33 to have  $AAE$  values  $> 1$ , with typical reported values of  $\sim 1.5$ -3 (Yang et al., 2009; Russell et al., 2010;  
§34 Bahadur et al., 2012), larger than is typically observed for black carbon. The measured average  $AAE_{super}$   
§35 values were [greater than unity and larger than the  \$AAE\_{PM1}\$  \(Table 2\)](#), suggestive of a dust influence.  
§36 However, there are two important points to consider. First, although the  $AAE_{super}$  values were  
§37 approximately normally distributed, the distributions were substantially broader than the distributions for  
§38 the submicron particles, with a range of about  $0.5 < AAE_{super} < 3$  ([Figure 5](#)). Second, the  $AAE_{super}$  values  
§39 exhibited a notable wavelength-pair dependence, with the largest values observed for the 450-532 nm pair  
§40 and the smallest for the 532-660 nm pair and where the wavelength-dependence at T0 was much larger  
§41 than at T1 (Table 2; [Figure 5](#)). The large spread in the  $AAE_{super}$  values may reflect the small magnitudes of  
§42 the absolute  $b_{abs,super}$  values and the use of the difference method to determine the  $b_{abs,super}$  (i.e. noise), but

Deleted: as well as

Deleted: Figure S5

Deleted: typically

Formatted: Font: Not Bold

Deleted: Figure 4

Formatted: Font: Not Bold

Deleted: Figure 4



could also indicate a greater diversity in  $AAE_{\text{super}}$  values compared to  $AAE_{\text{PM1}}$  due to, perhaps, time-varying contributions from dust and BC. As a test, if the averaged  $AAE_{\text{PM1}}$  values are restricted to periods when the absolute absorption was relatively low ( $< 0.6 \text{ Mm}^{-1}$ ), but still generally larger than the  $b_{\text{abs,super}}$ , there is no substantial additional broadening of the distribution. This suggests that the broadening of  $AAE_{\text{super}}$  may be real and that the latter interpretation—diversity in individual  $AAE_{\text{super}}$  values—may be appropriate. However, since there were insufficient periods where the  $b_{\text{abs,PM1}}$  values were as low as the  $b_{\text{abs,super}}$ , changes in the shape of the  $AAE_{\text{PM1}}$  distribution cannot be assessed under the exact same conditions, and thus the possibility that the greater scatter simply reflects the low  $b_{\text{abs,super}}$  values cannot be ruled out. (The  $0.6 \text{ Mm}^{-1}$  threshold was chosen to allow for a sufficient number of  $AAE_{\text{PM1}}$  values to remain to be used to develop a histogram.) Also, if one considers the relationship between  $AAE_{\text{PM10}}$  and the  $f_{\text{sca,PM1}}$ , there is no obvious broadening of the  $AAE$  distribution at smaller values of  $f_{\text{sca,PM1}}$ . There is also some indication of correlations between both  $b_{\text{abs,super}}$  and  $b_{\text{abs,PM1}}$  and between  $b_{\text{abs,super}}$  and  $[\text{BC}]$  (as measured by the SP2) (Figure 6). Although the correlation coefficients are relatively small ( $r^2 = 0.45$  and  $0.25$  at T0 and T1, respectively), this could indicate contributions from penetration of BC into the supermicron mode, which could help to explain why most of the  $AAE_{\text{super}}$  values are smaller than is typical for pure dust but larger than for BC.

Further insight into the nature of the supermicron particles comes from consideration of the  $MAC$  and  $MSC$  values, which are intensive properties like the  $AAE$ . The  $MAC$  and  $MSC$  for supermicron particles have been assessed by comparing  $b_{\text{abs,super}}$  and  $b_{\text{sca,super}}$  with the supermicron mass concentration ( $[\text{PM}_{\text{super}}]$ ) as estimated from the measured size distributions (Figure 7a-b). The  $[\text{PM}_{\text{super}}]$  values were estimated assuming a density of  $2 \text{ g cm}^{-3}$  and spherical particles. In theory, the  $MSC$  is size dependent, falling off rapidly from  $\sim 4 \text{ m}^2 \text{ g}^{-1}$  to  $\sim 1.5 \text{ m}^2 \text{ g}^{-1}$  in going from  $d_{\text{p,m}} = 700$  to  $1000 \text{ nm}$  (with  $d_{\text{p,m}} = 700 \text{ nm}$  corresponding approximately to  $d_{\text{p,a}} = 1000 \text{ nm}$  when density =  $2 \text{ g cm}^{-3}$ ) and ranging from  $\sim 0.5 \text{ m}^2 \text{ g}^{-1}$  to  $1.5 \text{ m}^2 \text{ g}^{-1}$  for larger particles (see Figure S8 and Clarke et al. (2004)). Thus, smaller  $MSC$  values generally correspond to larger particles. The observed  $MSC_{\text{super}}$  exhibit an inverse relationship with  $d_{\text{p,surf}}$  for the supermicron particles (Figure 7e-f). To our knowledge, this is the first explicit demonstration of the theoretically expected inverse relationship from ambient observations. These observations indicate that the nature of the supermicron particle size distributions do vary with time, with some time periods containing larger supermicron particles and some smaller. This variability in size suggests variations in the supermicron particle sources, and consequently in the chemical nature of the particles, discussed further below.

Deleted: PM10

Deleted: Figure 5

Formatted: Font: Not Bold

Formatted: Font: Not Bold

Deleted: Figure 6

Deleted: Figure S6

Deleted: overall

Formatted: Font: Not Bold

Deleted: Figure 6

585 The relationship between  $b_{\text{abs,super}}$  and  $[\text{PM}_{\text{super}}]$  exhibits a great deal of scatter (Figure 7c-d), most  
 586 likely due to the small values of  $b_{\text{abs,super}}$  and to the variability in the  $\text{PM}_{\text{super}}$  sources, including particle  
 587 density and size. The  $\text{MAC}$  values at 532 nm for the supermicron particles range from  $\sim 0$  to  $\sim 0.06 \text{ m}^2 \text{ g}^{-1}$   
 588 at both sites. Further, the  $\text{MAC}_{\text{super}}$  values exhibit a notable dependence on the  $d_{\text{p,surf}}$  (Figure 7g-h). In  
 589 general, when  $d_{\text{p,surf}}$  is on the small side ( $\sim 2 \mu\text{m}$ ) the  $\text{MAC}_{\text{super}}$  is very close to zero and it tends to increase  
 590 with  $d_{\text{p,surf}}$ . Apparently, the particles from sources that produced, on average, smaller supermicron  
 591 particles were less absorbing than the particles from sources that produced larger particles. A plausible  
 592 explanation is that the larger particles are dust while the smaller (yet still supermicron) particles are a  
 593 combination of non-absorbing sea spray particles and other particle types that are penetrating from the  
 594 submicron mode. This hypothesis is generally supported by examination of HYSPLIT back trajectories  
 595 (Draxler and Rolph, 2015) for each day of the campaign (Figure S9), as well as by comparison with the  
 596 source-region identification in Fast et al. (2012), with smaller  $d_{\text{p,surf}}$  values for the supermicron particles  
 597 generally corresponding to periods when the air masses were identified as containing a greater “Bay Area”  
 598 contribution. Considering three specific days as examples, two (11 and 16 June) when the  $\text{MSC}_{\text{super}}$  were  
 599 particularly small (corresponding to larger particles) and one (15 June) when the  $\text{MSC}_{\text{super}}$  were larger,  
 600 clear differences in the air mass origins can be seen. Specifically, the back trajectories on 11 and 16 June  
 601 indicate that the air mass came from almost due north, consistent with a terrestrial origin for the particles  
 602 while the back trajectory on 15 June indicates that the air mass had passed over the San Francisco Bay  
 603 Area and before that came from along the CA coast. These back trajectories are generally consistent with  
 604 the idea that when the overall size distribution is skewed towards smaller supermicron particles (smaller  
 605  $d_{\text{p,surf}}$  and larger  $\text{MSC}_{\text{super}}$ ) the air masses are more impacted by sea spray particles, while when the size  
 606 distribution is skewed towards larger particles there is a greater relative dust contribution.

607 Even though the  $\text{MAC}_{\text{super}}$  exhibits a pronounced relationship with  $d_{\text{p,surf}}$ , there is actually minimal  
 608 dependence of  $b_{\text{abs,super}}$  on  $d_{\text{p,surf}}$  (Figure S10). There is, however, a relatively strong relationship between  
 609  $[\text{PM}_{\text{super}}]$  and  $d_{\text{p,surf}}$ , with larger  $[\text{PM}_{\text{super}}]$  usually corresponding to smaller  $d_{\text{p,surf}}$  (Figure S10). This  
 610 suggests that the small  $\text{MAC}_{\text{super}}$  values at small  $d_{\text{p,surf}}$  result from substantial inputs of non-absorbing  
 611 supermicron particles, which does not necessarily alter the observed  $b_{\text{abs,super}}$  but does serve to increase  
 612 the  $[\text{PM}_{\text{super}}]$ , thereby depressing the  $\text{MAC}_{\text{super}}$  values. The  $\text{MAC}_{\text{super}}$  is approximately  $0.06 \text{ m}^2 \text{ g}^{-1}$  when  
 613  $d_{\text{p,surf}}$  is large (i.e.  $> 3.5 \mu\text{m}$ ; Figure 7). If it is assumed that the major contributor to supermicron absorption  
 614 when  $d_{\text{p,surf}}$  is large is dust then a value for the imaginary refractive index ( $k$ ) for dust in this region is  
 615 estimated from Mie theory. Assuming spherical particles with  $d_p = 3.5 \mu\text{m}$  with density  $= 2 \text{ g cm}^{-3}$  and a  
 616 real refractive index of either 1.5 or 1.6, the  $k$  is  $\sim 0.0035i$ . However, this estimate assumes that all of the  
 617  $\text{PM}_{\text{super}}$  mass is dust and that no other absorbing species contribute. If some of the  $\text{PM}_{\text{super}}$  mass is

Formatted: Font: Not Bold

Deleted: Figure 6

Deleted: Figure 6

Formatted: Font: Not Bold

Deleted: Figure S7

Deleted: Figure S8

Deleted: Figure S8

Formatted: Font: Not Bold

Deleted: Figure 6

624 attributed to non-dust species, then the derived dust-specific  $MAC$  and  $k$  would be larger. Alternatively,  
625 if BC contributes substantially to the observed supermicron absorption, which seems likely, then the dust-  
626 specific  $MAC$  and  $k$  would be smaller. Most likely, the above values are upper-limits. Despite these  
627 uncertainties, the observed  $MAC$  and  $k$  are similar to reported estimates for dust in the Xianghe area in  
628 China, where  $MAC_{dust} = 0.048 \text{ m}^2 \text{ g}^{-1}$  at 520 nm and where the reported  $MAC$  has been adjusted to a  
629 density of  $2.0 \text{ g cm}^{-3}$  (Yang et al., 2009). Overall, although the contribution of supermicron particles to  
630 the total absorption is small in this region, it nonetheless must be considered.

631 *3.1.3 Relationship between scattering and absorption*

632 There has been increasing interest in the relationship between the absorption Ångström exponent  
633 and the scattering Ångström exponent (Yang et al., 2009; Russell et al., 2010; Bahadur et al., 2012; Giles  
634 et al., 2012; Cazorla et al., 2013; Costabile et al., 2013). The wide range of  $SAE$  values observed here  
635 allows for assessment of the  $AAE$  vs.  $SAE$  relationship in a constrained environment. The observed  
636  $AAE_{532-660}$  vs.  $SAE_{450-550}$  relationships for  $PM_{10}$ , submicron and supermicron particles are shown in [Figure](#)  
637 [8a-c](#). The observed  $AAE$  values at both sites fall in a fairly narrow range centered around 1.2 for  $PM_{10}$  and  
638 submicron particles, with much greater scatter for supermicron particles, consistent with [Figure 5](#). The  
639 submicron  $SAE$  values are  $>1.8$  and the supermicron  $SAE$  values are generally  $<0.2$ , while the  $PM_{10}$   $SAE$   
640 values span the range 0.3 – 2. The wide range of  $SAE$  values for  $PM_{10}$  results from time-varying  
641 contributions of supermicron and submicron particles to the total scattering. [Very similar results as shown](#)  
642 [in Figure 8 are obtained for both T0 and T1 when the other wavelength pairs are used \(not shown\).](#)

643 Cazorla et al. (2013) proposed a classification scheme based on the position in the  $AAE_{462-648}$  vs.  
644  $SAE_{450-700}$  space (c.f. their Figure 1). They classified particles with  $AAE < 1$  and  $SAE > 1.5$  as “EC  
645 dominated,” where EC stands for elemental carbon (which is approximately equivalent to BC (Andreae  
646 and Gelencser, 2006; Lack et al., 2014)). Here, almost none of the observations fall in this space, despite  
647 the submicron absorption being dominated by black carbon. Instead, the submicron measurements fall  
648 primarily in the space encompassed by  $1 < AAE < 1.5$  and  $SAE > 2$ , which Cazorla et al. (2013) classified  
649 as an “EC/OC mixture” and where an implicit assumption was that the OC (organic carbon) was absorbing  
650 in nature (i.e. BrC), thus leading to the elevated  $AAE$  values compared to the “EC dominated” region.  
651 These *in situ* measurements therefore suggest that the “EC/OC mixture” region should better be classified  
652 as “EC dominated” (or equivalently “BC dominated”). These measurements indicate that BrC  
653 contributions to submicron absorption can only be clearly identified if the  $AAE$  is well-above 1.5. Given  
654 that almost none of the submicron  $AAE$  values were  $< 1$ , the suggestion by Bahadur et al. (2012) that a  
655 “low-end baseline”  $AAE$  value of  $0.55 (\pm 0.24)$  that is related to “pure EC” seems unlikely to be correct

Formatted: Font: Not Bold

Deleted: Figure 7

Deleted: Figure 4

Formatted: Font: Not Bold

Deleted: previously

Deleted: and

and is more likely a result of a subset of the data points considered in that study having large uncertainties due to low signal levels. (Lower  $AAE$  values can be obtained if a wavelength pair is selected in which the wavelengths differ substantially and there is curvature in the  $b_{abs}$  vs. wavelength relationship (Bergstrom et al., 2007).) This conclusion is consistent with that of Russell et al. (2010) and with the *in situ* observations of Yang et al. (2009) and the remote sensing observations of Giles et al. (2012).

Cazorla et al. (2013) also classified particles having  $1 < AAE < 1.5$  and  $SAE < 1$  as being a “Dust/EC mix”, and those with  $AAE < 1$  and  $SAE < 1$  as being “Coated large particles.” As the supermicron contribution to scattering increases (and the  $SAE$  decreases), the observed  $AAE$  values, at T1 especially, do not strongly deviate from the 1-1.5 range. The supermicron particles sampled here were a mixture of sea spray and dust in varying amounts. This therefore suggests that the “Dust/EC mix” regime should be reclassified to be more general, as it is not specific to “dust,” only to “large particle/BC mixtures.” The measurements suggest that dust contributions can only be clearly elucidated when the  $AAE > 1.5$ , although even when such large  $AAE$  values are observed care must be taken if the absolute absorption values are small (as is the case here for supermicron particles), corresponding to individual  $AAE$  values with substantial uncertainties. Similar caution is suggested for identification of particles in the “Coated large particle” regime, as classified by Cazorla et al. (2013). The *in situ* measurements here suggest that observations that fall within this regime are likely the result of measurement uncertainties due to low signal levels, and do not correspond to the presence of “Coated large particles.” Based on the observations here, a new classification scheme using the  $AAE$  and  $SAE$  relationship is proposed (Figure 8d).

### 3.1.3 Light backscattering

The extent to which particles scatter light in the backward versus forward direction has an important controlling influence on their climate impacts, namely the amount of incident solar radiation that is reflected back to space and the associated radiative forcing (Haywood and Shine, 1995). Furthermore, the backscatter fraction and asymmetry parameter are important products of remote sensing retrievals. The backscatter fractions at 550 nm for  $PM_{10}$ ,  $f_{bsca,550,PM10}$ , measured by the nephelometer ranged from 0.1 to 0.23, with an average value of  $0.137 \pm 0.024$  for T0 and  $0.155 \pm 0.054$  for T1. These correspond to a  $g_{sca}$  range for  $PM_{10}$  of 0.40 to 0.67 and mean values of  $0.57 \pm 0.056$  for T0 and  $0.53 \pm 0.054$  for T1. This range of observed values is comparable to measurements made at other locations (Andrews et al., 2006), but the averages are somewhat smaller than  $g_{sca}$  values calculated by Kassianov et al. (2012) at 500 nm for the T0 and T1 sites (both  $g_{sca,500} = 0.65$ ). The observed  $g_{sca}$  versus  $f_{sca,PM1}$  relationship is shown in Figure 9b,c for T0 and T1. There is a general decrease in  $g_{sca}$  when  $f_{sca,PM1}$  increases at both sites, more clearly at T1 than at T0, but at both sites there is substantial scatter in the data. Some of this scatter appears to be driven

Deleted: Figure 7  
Formatted: Font: Not Bold

Deleted: this is a basic  
Deleted: parameter  
Deleted: for  
Deleted: and knowledge of atmospheric variability will improve such measurements

Deleted: Figure 8  
Formatted: Font: Not Bold  
Deleted: some

by variations in the size of the submicron mode, as characterized by  $d_{p,surf,PM1}$ . In general, for a given  $f_{sca,PM1}$  the observed  $g_{sca}$  values are smaller when  $d_{p,surf,PM1}$  is smaller.

This observed behavior is generally consistent with theoretical expectations. The theoretical relationship between  $g_{sca}$  and particle size for spherical particles is shown in [Figure 9a](#). The calculated  $g_{sca}$  increases nearly monotonically for diameters up to about 500 nm, reaching  $g_{sca} \sim 0.75$ . In the supermicron range above 1.5  $\mu m$  the  $g_{sca}$  is relatively constant around 0.75. In between 500 nm and 1.5  $\mu m$ , the  $g_{sca}$  exhibits a more complicated dependence on size. The steepness of the  $g_{sca}$  versus  $d_p$  relationship between 100 and 500 nm means that the observed  $g_{sca}$  for  $PM_{10}$  will be particularly sensitive to variations in the submicron particle size distribution. However, the  $g_{sca}$  will be less sensitive to variations in the supermicron particle size distribution because the  $d_p$  versus  $g_{sca}$  relationship is generally flatter. Further, we might expect some relationship between  $g_{sca}$  and the fraction of scattering due to sub- or supermicron particles to the extent that the two size regimes have generally distinct  $g_{sca}$  values. Indeed, such behavior is seen in the observations, in large part because the  $d_{p,surf,PM1}$  values vary within the sensitive range (100-500 nm).

Therefore, in an effort to account for this apparent co-dependence of  $g_{sca}$  on  $f_{sca,PM1}$  and  $d_{p,surf,PM1}$ , the  $f_{sca,PM1}$  values have been divided by the  $d_{p,surf,PM1}$  values, with the ratio indicated as  $R_g$ . There is, in general, a much stronger relationship between the  $g_{sca}$  values and  $R_g$  ([Figure 9d,e](#)) than there is with  $f_{sca,PM1}$  alone, and much of the residual scatter seems to be driven by variations in the supermicron size distribution. Linear fits give  $g_{sca} = -38.5R_g + 0.66$  for T0 ( $r^2 = 0.51$ ) and  $g_{sca} = -51.5R_g + 0.66$  for T1 ( $r^2 = 0.71$ ), and where  $d_{p,surf,PM1}$  is in nm. Overall, the observations here demonstrate that the observable backscatter coefficients depend importantly on the relative contributions of sub- versus supermicron particles to the total scattering, but that the specific relationship between backscatter and the sub- or supermicron scattering fraction is obscured by variations in the size distribution within each size range. However, the greatest sensitivity of  $g_{sca}$  is found for size variations within the submicron size range.

### 3.2 Influence of heating on optical properties

At the T0 site, the UCD CRD and PAS instruments sampled alternately dried, ambient particles ( $PM_{2.5}$ ) or particles that had been passed through a thermodenuder (TD) that was held at 225 °C during the study. As particles pass through the TD, some materials evaporate, including ammonium nitrate, ammonium sulfate and many organics, while others do not, including black carbon, dust and sea salt. Loss of these materials leads to changes in the optical properties, including the particle optically-weighted

Formatted: Font: Not Bold

Deleted: Figure 8

Deleted: Figure 8

Formatted: Font: Not Bold

732 hygroscopicity. The influence of heating on the optical properties is used here to further probe the particle  
733 composition.

734 The observed fraction of extinction remaining after heating,  $f_{\text{ext,TD}}$ , for PM<sub>2.5</sub> varied from ~0.15 to  
735 0.6, suggesting a wide range of particle volatility. This variability is strongly linked to the relative  
736 contribution of sub- versus supermicron particles to the observed extinction; an approximately linear  
737 relationship (with a [negative](#) slope) between  $f_{\text{ext,TD}}$  and the *EAE* measured for the ambient particles was  
738 observed ([Figure 10](#)). This increase in  $f_{\text{ext,TD}}$  with decreasing *EAE* suggests that the supermicron  
739 components are mostly non-volatile, consistent with a likely dust or sea salt contribution as identified  
740 above. Further, this suggests that  $f_{\text{ext,TD}}$  can be used as an indicator of [coarse mode fraction](#) in the current  
741 study. There is a cluster of points at the highest  $f_{\text{ext,TD}}$  (the light green points in [Figure 10](#)) that were  
742 observed during a specific overnight period when we suspect that the site was briefly impacted by large  
743 particles produced as part of local road resurfacing.

744 The bulk particle hygroscopicity, characterized by  $\gamma_{\text{RH}}$ , did not vary monotonically with  $f_{\text{ext,TD}}$   
745 ([Figure 11a](#)). This is because the observed hygroscopicity depends on compositional variability within  
746 both the sub- and supermicron modes (Atkinson et al., 2015). However, the change in the hygroscopicity  
747 upon heating,  $\Delta\gamma_{\text{RH}} = \gamma_{\text{RH,ambient}} - \gamma_{\text{RH,TD}}$ , does exhibit a clear correlation with  $f_{\text{ext,TD}}$ , with larger  $\Delta\gamma_{\text{RH}}$   
748 corresponding to smaller  $f_{\text{ext,TD}}$ , i.e. for smaller, typically more volatile particles ([Figure 11b](#)). The  
749 observed  $\Delta\gamma_{\text{RH}}$  appear to cross over zero around  $f_{\text{ext,TD}} = 0.4$ . Apparently, for smaller particles that exhibit  
750 greater overall mass loss upon heating, the  $\gamma_{\text{RH}}$  tends to decrease with heating. This is as might be  
751 expected, since one key residual component will be non-hygroscopic BC when the distribution is  
752 dominated by smaller particles. However, when the distribution is dominated by larger particles,  
753 evaporation leads to the residual particles appearing, on average, slightly more hygroscopic. This suggests  
754 that the supermicron components that are susceptible to evaporation are lower-hygroscopicity material,  
755 most likely organics but also, potentially, inorganics such as [ammonium](#) sulfate and [ammonium](#) nitrate,  
756 which have lower hygroscopicity than sodium chloride. [Some of the sea salt-containing particles observed](#)  
757 [during CARES were found to be internally mixed with organics \(likely organic acids\) that displaced](#)  
758 [chloride \(Laskin et al., 2012\), and organic salts are generally less hygroscopic than sea salt \(Drozd et al.,](#)  
759 [2014\). It is possible that these organics evaporated in the TD, leaving behind more hygroscopic material,](#)  
760 [although such a hypothesis requires further investigation. It is alternatively possible that the](#)  
761 [thermodenuding removed residual water that did not fully evaporate in the drier due to the presence of](#)  
762 [magnesium sea salts \(which do not effloresce until very low RH\), leading to an apparent increase in the](#)  
763 [hygroscopicity of the thermodenuded particles. However, the potential impact from this is expected to](#)

Deleted: positive

Deleted: Figure 9

Formatted: Font: Not Bold

Deleted: particle size

Formatted: Font: Not Bold

Deleted: Figure 9

Deleted: Figure 10

Formatted: Font: Not Bold

Formatted: Not Highlight

Formatted: Font: Not Bold

Deleted: Figure 10

Deleted: {Gupta, 2015 #1832}

771 [have been quite limited, given the small amount of residual water retained by magnesium salts at low RH](#)  
772 (Gupta et al., 2015).

773 The contribution to the total light absorption from non-BC materials that evaporate in the TD was  
774 characterized by the absorption enhancement,  $E_{\text{abs}}$ , which is here taken as the ratio between the ambient  
775 and thermodenuded  $b_{\text{abs}}$ . We have previously investigated the dependence of  $E_{\text{abs}}$  on photochemical age  
776 at CARES using the same data set as is being considered here, and separately the dependence on the  
777 relative amount of “coating” (non-BC) material that is internally mixed with BC at the CalNex field study  
778 (Cappa et al., 2012). It was found that the  $E_{\text{abs}}$  increases by only a small amount as PCA and coating  
779 amount increased. Here, we see that  $E_{\text{abs}}$  exhibits some slight dependence on  $f_{\text{ext},\text{TD}}$ , with somewhat larger  
780 values observed at smaller  $f_{\text{ext},\text{TD}}$  (Figure 11c,d). It is difficult to establish whether this dependence  
781 indicates that larger  $E_{\text{abs}}$  would have been observed in Cappa et al. (2012) for the CARES dataset had  
782 more material evaporated, but given that the  $f_{\text{ext},\text{TD}}$  here is determined predominately by changes in the  
783 relative contributions from sub- and supermicron particles this seems unlikely. (The complementary  
784 measurements from CalNex were for  $\text{PM}_{10}$ , not  $\text{PM}_{2.5}$  as here, and thus the influence of supermicron  
785 particles on the observations was substantially smaller during that study. For reference, the CalNex  
786 campaign-average submicron SAE for the 450-550 nm pair was 2.1. Thus, the conclusions here for the  
787 CARES dataset are not necessarily applicable to the interpretation of the CalNex dataset.) Further, a fit  
788 of the mean binned values of  $E_{\text{abs}}$  extrapolated to  $f_{\text{ext},\text{TD}} = 0$  gives only  $E_{\text{abs}} = 1.14 (\pm 0.02)$  and  $1.29 (\pm 0.06)$   
789 at 532 nm and 405 nm, respectively, suggesting that substantially larger values than the observed range  
790 would not have been likely had a greater extent of evaporation been observed. The larger extrapolated  
791 value at 405 nm than at 532 nm is consistent with a small contribution from so-called “brown carbon,”  
792 which has an absorption spectrum that strongly increases towards shorter wavelengths, to the observed  
793 absorption.

794 The particle single scatter albedo exhibits a non-monotonic dependence on  $f_{\text{ext},\text{TD}}$  at both 532 nm  
795 and 405 nm (Figure 11e,f). On average, the ambient SSA values are at a minimum of 0.85 around  $f_{\text{ext},\text{TD}}$   
796  $= 0.35$ . The SSA then increases at either larger or smaller  $f_{\text{ext},\text{TD}}$ . The increase in SSA towards smaller  
797  $f_{\text{ext},\text{TD}}$  likely reflects an increasing contribution of secondary aerosol species within the submicron mode  
798 (e.g. organics, ammonium sulfate, ammonium nitrate) relative to BC, leading the overall particulates to  
799 appear both more volatile and more scattering. Indeed, HR-AMS measurements indicate that secondary  
800 inorganic and organic species are dominant components of the submicron particles in the Sacramento and  
801 Sierra Nevada foothill region during CARES (Setyan et al., 2012; Shilling et al., 2013). The increase in  
802 SSA towards larger  $f_{\text{ext},\text{TD}}$  likely results from the increasing contribution of non-volatile sea salt and dust

Formatted: Font: Not Bold

Deleted: Figure 10

Deleted: Figure 10

Formatted: Font: Not Bold



805 components within the supermicron mode that are either non- or very weakly absorbing. Looking at the  
 806 change in SSA upon heating in the TD,  $\Delta\text{SSA}$ , there is a clear increase in  $\Delta\text{SSA}$  with decreasing  $f_{\text{ext,TD}}$   
 807 (Figure 11g,h). This is as expected because if material does not evaporate then no change in SSA should  
 808 be observed. The  $\Delta\text{SSA}$  linearly extrapolated to  $f_{\text{ext,TD}} = 0$  is  $0.46 (\pm 0.02)$  and  $0.50 (\pm 0.02)$  at 532 nm and  
 809 405 nm, respectively, corresponding to absolute extrapolated SSA values of  $\sim 0.4$  given the observed  
 810 ambient particle SSA values. (Linear extrapolation to zero is not fully justifiable because the  $f_{\text{ext,TD}}$  cannot  
 811 go to zero if there is some BC around or if there are other non-volatile materials and because there appears  
 812 to be some flattening off in the  $\Delta\text{SSA}$  values at smaller  $f_{\text{ext,TD}}$ . Nonetheless, it can provide an estimate in  
 813 the limit of small BC contributions.) These extrapolated SSA values are relatively large compared to some  
 814 laboratory observations for “fresh” BC particles that are produced, for example, from flames (Cross et al.,  
 815 2010) or gasoline or diesel vehicles (Schnaiter et al., 2005; Forestieri et al., 2013) and that have little  
 816 intrinsic organic material, but slightly smaller than that reported by one other laboratory study on flame-  
 817 generated soot (Radney et al., 2014). Primary emitted BC has a fractal-like structure that is thought to  
 818 collapse over time through atmospheric ageing processes. This change in shape due to collapse is thought  
 819 to lead to an increase in the SSA, separate from any contributions from scattering coating materials  
 820 (Chakrabarty et al., 2014). That the extrapolated SSA values are larger than many of the laboratory studies  
 821 on fresh BC suggests that the sampled particles were somewhat collapsed compared to their emitted state.  
 822 However, if non-absorbing and non-volatile materials remained (e.g. sea salt), then the extrapolated SSA  
 823 would not be fully representative of pure BC particles, confounding straightforward interpretation in terms  
 824 of morphological changes.

825 For the period where the T0 site was impacted by particles emitted from local road surfacing  
 826 activities (e.g. asphalt), the ambient SSA values are small and the  $\Delta\text{SSA}$  values deviate from the general  
 827 relationship observed for other periods. In fact, the absolute SSA measured for thermodenuded particles  
 828 during this particular period are around zero at 405 nm but  $\sim 0.2$  at 532 nm. Such very small SSA values  
 829 suggest that absorption is dominated by very small particles, or at least particles that are agglomerates of  
 830 very small spherules; the surface area-weighted size distribution measured during this period peaked  
 831 around 300 nm diameter and the SP2 BC particle size distributions clearly indicate that the overall BC  
 832 particle size was larger during the asphalt-impacted period (Figure S11), suggesting that agglomerates of  
 833 small spherules is most plausible. We cannot entirely rule out the possibility that the measurements during  
 834 this period were strongly impacted by some absorbing gas-phase species (e.g.  $\text{NO}_2$ ), confounding the SSA  
 835 measurements, although there was no evidence of gas-phase absorption in the background CRD channels  
 836 during this period suggesting that this is unlikely.

Formatted: Font: Not Bold

Deleted: Figure 10

Deleted: Figure S9



#### 4 Conclusions

Optical property measurements of  $PM_1$ ,  $PM_{2.5}$  and  $PM_{10}$  made during the CARES 2010 field study have been examined to develop understanding of the relationships between various intensive properties and to establish differences in behavior between sub- and supermicron PM. Measurements were made at two sites in the Sacramento region, one urban (T0) and one more rural (T1) but impacted by the urban outflow on most days under southwesterly flow conditions (Fast et al., 2012). At both sites, there is a strong contribution of supermicron particles to the total scattering, averaging around 50% at both sites. The source of these supermicron particles appears to be a combination of local dust and sea spray, along with some contributions from penetration of traditionally submicron particles into the supermicron mode. The specific contributions of any of these supermicron particle sources varies with time and depends on the prevailing transport patterns with, perhaps not surprisingly, generally larger sea spray contributions when air masses have been transported from the San Francisco Bay Area. The measured scattering Ångström exponents (*SAE*) for  $PM_{10}$  are strongly correlated with the submicron versus supermicron fraction of the total scattering, with similar linear relationships observed at both sites. This relationship held despite there being variations in the size distributions within a given mode, which can theoretically alter the *SAE*. This suggests that the relationships determined here are quite general, and that the *SAE* can be used to quantitatively attribute scattering to sub- and supermicron particles. There was no notable dependence of the absorption Ångström exponent (*AAE*) on *SAE* for  $PM_{10}$ , and these observations were used to propose an updated particle classification scheme based on the relationship between these two parameters.

The influence of photochemical processing on the sub- versus supermicron contribution to scattering differed between the two sites, with photochemical processing leading to an increase in the submicron fraction of scattering for the T0 (urban) site but minimal change, or even a slight decrease, at the T1 (downwind) site. This reflects in part the strong daytime peak in photochemical age at the T0 site in contrast to the more gradual increase at the T1 site, coupled with the much stronger diurnal profile in the wind speed, with a daytime peak, at the T1 site. Consequently, at the T1 site, photochemical production of secondary PM was spread over a wider range of times due to transport and was countered through local, temporally similar increases in dust production due to the higher daytime winds. At the T0 site, the strong photochemical production of secondary PM led to a clear increase in the submicron fraction of scattering with photochemical ageing.

The mass scattering coefficient for the supermicron particles varied inversely with the median surface-weighted particle diameter ( $d_{p,surf}$ ) of the supermicron mode, in general accordance with

theoretical expectations. This indicates clear temporal variability in the nature of the supermicron particle sources, which seem to be coupled to the prevailing wind direction or air mass history, as established through consideration of back trajectories. Light absorption was dominated by submicron particles, although there was some contribution from the supermicron particles. The mass absorption coefficient for supermicron particles exhibited a clear dependence on the supermicron  $d_{p,surf}$ , most likely due to variations in the relative contributions of non-absorbing sea spray particles, penetration of BC from the submicron mode, and very weak absorption by supermicron dust particles. Particle backscatter was found to be related to the relative fractions of sub- versus supermicron scattering, but with an additional sensitivity to variations in the size distribution within the submicron size range. The susceptibility of the particles to heating in a thermodenuder depended explicitly on the contribution of supermicron particles to the  $PM_{2.5}$  extinction, most likely because a large fraction of the supermicron particles were either essentially non-volatile sea spray or dust particles. Heating in general led to an increase in the average particle hygroscopicity and a decrease in the single scatter albedo. These together indicate that the residual particles are likely a combination of absorbing submicron BC and somewhat hygroscopic supermicron sea spray and less hygroscopic dust. The results presented here demonstrate that optical property measurements can be used to assess likely chemical differences in the contributing particle types, and thus to identify key PM sources.

**Author Information**

Corresponding Author: Christopher D. Cappa

E-mail: [cdcappa@ucdavis.edu](mailto:cdcappa@ucdavis.edu)

The authors declare no competing financial interest.

**Acknowledgements**

This work was supported by the Atmospheric System Research (ASR) program sponsored by the US Department of Energy (DOE), Office of Biological and Environmental Research (OBER), including Grant No. DE-SC0008937. The authors acknowledge W. Berk Knighton for the PTR-MS data at the T1 site, R. Subramanian for the SP2 data, Ari Setyan for collection of the SMPS data at the T1 site and B. Tom Jobson for the  $NO_x$ ,  $NO_y$ , PTR-MS and meteorological data at the T0 site. The authors acknowledge the NOAA Air Resources Laboratory (ARL) for the provision of the HYSPLIT transport and dispersion model (<http://www.ready.noaa.gov>) used in this publication. The backscattering Mie calculations were performed using MiePlot from Philip Laven ([www.philiplaven.com/mieplot.htm](http://www.philiplaven.com/mieplot.htm)). Funding for data

collection was provided by the US DOE's Atmospheric Radiation Measurement (ARM) Program. All data used in this study are available from the ARM data archive at: <http://www.arm.gov/campaigns/aaf2009carbonaerosol>. The views expressed in this document are solely those of the authors and the funding agencies do not endorse any products or commercial services mentioned in this publication.

## References

- Anderson, T. L., Masonis, S. J., Covert, D. S., Ahlquist, N. C., Howell, S. G., Clarke, A. D., and McNaughton, C. S.: Variability of aerosol optical properties derived from in situ aircraft measurements during ACE-Asia, *J. Geophys. Res.*, 108, 8647, doi:10.1029/2002JD003247, 2003.
- Anderson, T. L. and Ogren, J. A.: Determining Aerosol Radiative Properties Using the TSI 3563 Integrating Nephelometer, *Aerosol Sci. Technol.*, 29, 57-69, doi:10.1080/02786829808965551, 1998.
- Andreae, M. O. and Gelencser, A.: Black carbon or brown carbon? The nature of light-absorbing carbonaceous aerosols, *Atmos. Chem. Phys.*, 6, 3131-3148, doi:10.5194/acp-6-3131-2006, 2006.
- Andrews, E., Sheridan, P. J., Fiebig, M., McComiskey, A., Ogren, J. A., Arnott, P., Covert, D., Elleman, R., Gasparini, R., Collins, D., Jonsson, H., Schmid, B., and Wang, J.: Comparison of methods for deriving aerosol asymmetry parameter, *J. Geophys. Res.-Atmos.*, 111, D05S04, doi:10.1029/2004JD005734, 2006.
- Atkinson, D. B., Radney, J. G., Lum, J., Kolesar, K. R., Cziczo, D. J., Pekour, M. S., Zhang, Q., Setyan, A., Zelenyuk, A., and Cappa, C. D.: Aerosol optical hygroscopicity measurements during the 2010 CARES campaign, *Atmos. Chem. Phys.*, 15, 4045-4061, doi:10.5194/acp-15-4045-2015, 2015.
- Atkinson, R., Baulch, D. L., Cox, R. A., Crowley, J. N., Hampson, R. F., Hynes, R. G., Jenkin, M. E., Rossi, M. J., Troe, J., and Subcommittee, I.: Evaluated kinetic and photochemical data for atmospheric chemistry: Volume II - gas phase reactions of organic species, *Atmos. Chem. Phys.*, 6, 3625-4055, doi:10.5194/acp-6-3625-2006, 2006.
- Bahadur, R., Praveen, P. S., Xu, Y., and Ramanathan, V.: Solar absorption by elemental and brown carbon determined from spectral observations, *Proc. Nat. Acad. Sci.*, 109, 17366-17371, doi:10.1073/pnas.1205910109, 2012.
- Bates, T. S., Anderson, T. L., Baynard, T., Bond, T., Boucher, O., Carmichael, G., Clarke, A., Erlick, C., Guo, H., Horowitz, L., Howell, S., Kulkarni, S., Maring, H., McComiskey, A., Middlebrook, A., Noone, K., O'Dowd, C. D., Ogren, J., Penner, J., Quinn, P. K., Ravishankara, A. R., Savoie, D. L., Schwartz, S. E., Shinozuka, Y., Tang, Y., Weber, R. J., and Wu, Y.: Aerosol direct radiative effects over the northwest Atlantic, northwest Pacific, and North Indian Oceans: estimates based on in-situ chemical

and optical measurements and chemical transport modeling, *Atmos. Chem. Phys.*, 6, 1657-1732, doi:10.5194/acp-6-1657-2006, 2006.

Bergstrom, R. W., Pilewskie, P., Russell, P. B., Redemann, J., Bond, T. C., Quinn, P. K., and Sierau, B.: Spectral absorption properties of atmospheric aerosols, *Atmos. Chem. Phys.*, 7, 5937-5943, doi:10.5194/acp-7-5937-2007, 2007.

Bohren, C. F. and Huffman, D. R.: *Absorption and scattering of light by small particles*, Wiley, New York, 1983.

Bond, T. C., Anderson, T. L., and Campbell, D.: Calibration and intercomparison of filter-based measurements of visible light absorption by aerosols, *Aerosol Sci. Technol.*, 30, 582-600, doi:10.1080/027868299304435, 1999.

Brown, S. S., Talukdar, R. K., and Ravishankara, A. R.: Rate constants for the reaction  $\text{OH} + \text{NO}_2 + \text{M} \rightarrow \text{HNO}_3 + \text{M}$  under atmospheric conditions, *Chem. Phys. Lett.*, 299, 277-284, doi:10.1016/S0009-2614(98)01283-4, 1999.

California Air Resources Board: Characterization of ambient PM10 and PM2.5 in California. Sacramento, CA, 2005; <http://www.arb.ca.gov/pm/pmmeasures/pmch05/pmch05.htm>.

Canagaratna, M. R., Jayne, J. T., Jimenez, J. L., Allan, J. D., Alfarra, M. R., Zhang, Q., Onasch, T. B., Drewnick, F., Coe, H., Middlebrook, A., Delia, A., Williams, L. R., Trimborn, A. M., Northway, M. J., DeCarlo, P. F., Kolb, C. E., Davidovits, P., and Worsnop, D. R.: Chemical and microphysical characterization of ambient aerosols with the Aerodyne aerosol mass spectrometer, *Mass Spectrom. Rev.*, 26, 185-222, doi:10.1002/mas.20115, 2007.

Cappa, C. D., Onasch, T. B., Massoli, P., Worsnop, D., Bates, T. S., Cross, E., Davidovits, P., Hakala, J., Hayden, K., Jobson, B. T., Kolesar, K. R., Lack, D. A., Lerner, B., Li, S. M., Mellon, D., Nuaanman, I., Olfert, J., Petaja, T., Quinn, P. K., Song, C., Subramanian, R., Williams, E. J., and Zaveri, R. A.: Radiative absorption enhancements due to the mixing state of atmospheric black carbon *Science*, 337, 1078-1081, doi:10.1126/science.1223447, 2012.

Cappa, C. D., Williams, E. J., Lack, D. A., Buffaloe, G. M., Coffman, D., Hayden, K. L., Herndon, S. C., Lerner, B. M., Li, S. M., Massoli, P., McLaren, R., Nuaaman, I., Onasch, T. B., and Quinn, P. K.: A case study into the measurement of ship emissions from plume intercepts of the NOAA Ship Miller Freeman, *Atmos. Chem. Phys.*, 14, 1337-1352, doi:10.5194/acp-14-1337-2014, 2014.

Cazorla, A., Bahadur, R., Suski, K. J., Cahill, J. F., Chand, D., Schmid, B., Ramanathan, V., and Prather, K. A.: Relating aerosol absorption due to soot, organic carbon, and dust to emission sources determined from in-situ chemical measurements, *Atmos. Chem. Phys.*, 13, 9337-9350, doi:10.5194/acp-13-9337-2013, 2013.

966 Chakrabarty, R. K., Beres, N. D., Moosmuller, H., China, S., Mazzoleni, C., Dubey, M. K., Liu,  
 967 L., and Mishchenko, M. I.: Soot superaggregates from flaming wildfires and their direct radiative  
 968 forcing, *Scientific Reports*, 4, 5508, doi:10.1038/srep05508, 2014.  
 969 Chung, C. E., Ramanathan, V., and Decremer, D.: Observationally constrained estimates of  
 970 carbonaceous aerosol radiative forcing, *Proc. Nat. Acad. Sci.*, 109, 11624-11629,  
 971 doi:10.1073/pnas.1203707109, 2012.  
 972 Clarke, A. and Kapustin, V.: Hemispheric Aerosol Vertical Profiles: Anthropogenic Impacts on  
 973 Optical Depth and Cloud Nuclei, 329, 1488-1492, doi:10.1126/science.1188838, 2010.  
 974 Clarke, A., Shinozuka, Y., Kapustin, V. N., Howell, S., Huebert, B. J., Doherty, S. J., Anderson,  
 975 T. L., Covert, D., Anderson, J., Hua, X., Moore II, K. G., McNaughton, C., Carmichael, G., and Weber,  
 976 R.: Size distributions and mixtures of dust and black carbon aerosol in Asian outflow: Physiochemistry  
 977 and optical properties, *J. Geophys. Res.*, 109, D15S09, doi:10.1029/2003JD004378, 2004.  
 978 Costabile, F., Barnaba, F., Angelini, F., and Gobbi, G. P.: Identification of key aerosol  
 979 populations through their size and composition resolved spectral scattering and absorption, *Atmos.*  
 980 *Chem. Phys.*, 13, 2455-2470, doi:10.5194/acp-13-2455-2013, 2013.  
 981 Cross, E. S., Onasch, T. B., Ahern, A., Wrobel, W., Slowik, J. G., Olfert, J., Lack, D. A.,  
 982 Massoli, P., Cappa, C. D., Schwarz, J. P., Spackman, J. R., Fahey, D. W., Sedlacek, A., Trimborn, A.,  
 983 Jayne, J. T., Freedman, A., Williams, L. R., Ng, N. L., Mazzoleni, C., Dubey, M., Brem, B., Kok, G.,  
 984 Subramanian, R., Freitag, S., Clarke, A., Thornhill, D., Marr, L. C., Kolb, C. E., Worsnop, D. R., and  
 985 Davidovits, P.: Soot Particle Studies—Instrument Inter-Comparison—Project Overview, *Aerosol Sci.*  
 986 *Technol.*, 44, 592 - 611, doi:10.1080/02786826.2010.482113, 2010.  
 987 Cziczo, D. J., Thomson, D. S., Thompson, T. L., DeMott, P. J., and Murphy, D. M.: Particle  
 988 analysis by laser mass spectrometry (PALMS) studies of ice nuclei and other low number density  
 989 particles, *Int. J. Mass Spectrom.*, 258, 21-29, doi:10.1016/j.ijms.2006.05.013, 2006.  
 990 DeCarlo, P. F., Slowik, J. G., Worsnop, D., Davidovits, P., and Jimenez, J. L.: Particle  
 991 morphology and density characterization by combined mobility and aerodynamic diameter  
 992 measurements. Part 1: Theory, *Aerosol Science and Technology*, 38, 1185-1205,  
 993 doi:10.1080/027868290903907, 2004.  
 994 Draxler, R. R. and Rolph, G. D.: HYSPLIT (HYbrid Single-Particle Lagrangian Integrated  
 995 Trajectory) Model access via NOAA ARL READY Website, <http://www.arl.noaa.gov/HYSPLIT.php>,  
 996 NOAA Air Resources Laboratory, College Park, MD, USA, last access: 29 August 2015, 2015.

997 Drozd, G., Woo, J., Hakkinen, S. A. K., Nenes, A., and McNeill, V. F.: Inorganic salts interact  
 998 with oxalic acid in submicron particles to form material with low hygroscopicity and volatility, *Atmos.*  
 999 *Chem. Phys.*, 14, 5205-5215, doi:10.5194/acp-14-5205-2014, 2014.

1000 Dubovik, O., Holben, B., Eck, T. F., Smirnov, A., Kaufman, Y. J., King, M. D., Tanre, D., and  
 1001 Slutsker, I.: Variability of absorption and optical properties of key aerosol types observed in worldwide  
 1002 locations, *J. Atmos. Sci.*, 59, 590-608, 2002.

1003 Dubovik, O. and King, M. D.: A flexible inversion algorithm for retrieval of aerosol optical  
 1004 properties from Sun and sky radiance measurements, 105, 20673-20696, doi:10.1029/2000JD900282,  
 1005 2000.

1006 Eck, T. F., Holben, B. N., Sinyuk, A., Pinker, R. T., Goloub, P., Chen, H., Chatenet, B., Li, Z.,  
 1007 Singh, R. P., Tripathi, S. N., Reid, J. S., Giles, D. M., Dubovik, O., O'Neill, N. T., Smirnov, A., Wang,  
 1008 P., and Xia, X.: Climatological aspects of the optical properties of fine/coarse mode aerosol mixtures,  
 1009 115, D19205, doi:10.1029/2010JD014002, 2010.

1010 Ewing, S. A., Christensen, J. N., Brown, S. T., Vancuren, R. A., Cliff, S. S., and Depaolo, D. J.:  
 1011 Pb Isotopes as an Indicator of the Asian Contribution to Particulate Air Pollution in Urban California,  
 1012 *Environ. Sci. Technol.*, 44, 8911-8916, doi:10.1021/es101450t, 2010.

1013 Fast, J. D., Gustafson Jr, W. I., Berg, L. K., Shaw, W. J., Pekour, M., Shrivastava, M., Barnard,  
 1014 J. C., Ferrare, R. A., Hostetler, C. A., Hair, J. A., Erickson, M., Jobson, B. T., Flowers, B., Dubey, M.  
 1015 K., Springston, S., Pierce, R. B., Dolislager, L., Pederson, J., and Zaveri, R. A.: Transport and mixing  
 1016 patterns over Central California during the carbonaceous aerosol and radiative effects study (CARES),  
 1017 *Atmos. Chem. Phys.*, 12, 1759-1783, doi:10.5194/acp-12-1759-2012, 2012.

1018 Forestieri, S. D., Collier, S., Kuwayama, T., Zhang, Q., Kleeman, M. J., and Cappa, C. D.: Real-  
 1019 Time Black Carbon Emission Factor Measurements from Light Duty Vehicles, *Environ. Sci. Technol.*,  
 1020 47, 13104-13112, doi:10.1021/es401415a, 2013.

1021 Garland, R. M., Yang, H., Schmid, O., Rose, D., Nowak, A., Achtert, P., Wiedensohler, A.,  
 1022 Takegawa, N., Kita, K., Miyazaki, Y., Kondo, Y., Hu, M., Shao, M., Zeng, L. M., Zhang, Y. H.,  
 1023 Andreae, M. O., and Pöschl, U.: Aerosol optical properties in a rural environment near the mega-city  
 1024 Guangzhou, China: implications for regional air pollution, radiative forcing and remote sensing, *Atmos.*  
 1025 *Chem. Phys.*, 8, 5161-5186, doi:10.5194/acp-8-5161-2008, 2008.

1026 Giles, D. M., Holben, B. N., Eck, T. F., Sinyuk, A., Smirnov, A., Slutsker, I., Dickerson, R. R.,  
 1027 Thompson, A. M., and Schafer, J. S.: An analysis of AERONET aerosol absorption properties and  
 1028 classifications representative of aerosol source regions, 117, D17203, doi:10.1029/2012JD018127,  
 1029 2012.

1030        Ginoux, P., Prospero, J. M., Gill, T. E., Hsu, N. C., and Zhao, M.: Global-scale attribution of  
1031 anthropogenic and natural dust sources and their emission rates based on MODIS Deep Blue aerosol  
1032 products, *Rev. Geophys.*, 50, RG3005, doi:10.1029/2012RG000388, 2012.

1033        Gupta, D., Eom, H. J., Cho, H. R., and Ro, C. U.: Hygroscopic behavior of NaCl–MgCl<sub>2</sub> mixture  
1034 particles as nascent sea-spray aerosol surrogates and observation of efflorescence during humidification,  
1035 *Atmos. Chem. Phys.*, 15, 11273–11290, doi:10.5194/acp-15-11273-2015, 2015.

1036        Gyawali, M., Arnott, W. P., Lewis, K., and Moosmüller, H.: In situ aerosol optics in Reno, NV,  
1037 USA during and after the summer 2008 California wildfires and the influence of absorbing and non-  
1038 absorbing organic coatings on spectral light absorption, *Atmos. Chem. Phys.*, 9, 8007–8015,  
1039 doi:10.5194/acp-9-8007-2009, 2009.

1040        Gysel, M., Laborde, M., Olfert, J. S., Subramanian, R., and Gröhn, A. J.: Effective density of  
1041 Aquadag and fullerene soot black carbon reference materials used for SP2 calibration, *Atmos. Meas.*  
1042 *Technol.*, 4, 2851–2858, doi:10.5194/amt-4-2851-2011, 2011.

1043        Haywood, J. M. and Shine, K. P.: The Effect of Anthropogenic Sulfate and Soot Aerosol on the  
1044 Clear-Sky Planetary Radiation Budget, *Geophys. Res. Lett.*, 22, 603–606, doi:10.1029/95GL00075,  
1045 1995.

1046        Huffman, J. A., Ziemann, P. J., Jayne, J. T., Worsnop, D. R., and Jimenez, J. L.: Development  
1047 and characterization of a fast-stepping/scanning thermodenuder for chemically-resolved aerosol  
1048 volatility measurements, *Aerosol Sci. Technol.*, 42, 395–407, doi:10.1080/02786820802104981, 2008.

1049        IPCC: Climate Change 2013: The Physical Science Basis. Contribution of Working Group I to  
1050 the Fifth Assessment Report of the Intergovernmental Panel on Climate Change, Cambridge University  
1051 Press, Cambridge, United Kingdom and New York, NY, USA, 2013.

1052        Jung, J., Lee, H., Kim, Y. J., Liu, X., Zhang, Y., Hu, M., and Sugimoto, N.: Optical properties of  
1053 atmospheric aerosols obtained by in situ and remote measurements during 2006 Campaign of Air  
1054 Quality Research in Beijing (CAREBeijing-2006), *J. Geophys. Res.*, 114, n/a–n/a,  
1055 doi:10.1029/2008JD010337, 2009.

1056        Kassianov, E., Pekour, M., and Barnard, J.: Aerosols in central California: Unexpectedly large  
1057 contribution of coarse mode to aerosol radiative forcing, *Geophys. Res. Lett.*, 39, L20806,  
1058 doi:10.1029/2012GL053469, 2012.

1059        Kaufman, Y. J., Tanre, D., and Boucher, O.: A satellite view of aerosols in the climate system,  
1060 *Nature*, 419, 215–223, doi:10.1038/nature01091, 2002.

1061 Laborde, M., Mertes, P., Zieger, P., Dommen, J., Baltensperger, U., and Gysel, M.: Sensitivity  
 1062 of the Single Particle Soot Photometer to different black carbon types, *Atmos. Meas. Tech.*, 5, 1031-  
 1063 1043, doi:10.5194/amt-5-1031-2012, 2012a.

1064 Laborde, M., Schnaiter, M., Linke, C., Saathoff, H., Naumann, K. H., Möhler, O., Berlenz, S.,  
 1065 Wagner, U., Taylor, J. W., Liu, D., Flynn, M., Allan, J. D., Coe, H., Heimerl, K., Dählkötter, F.,  
 1066 Weinzierl, B., Wollny, A. G., Zannata, M., Cozic, J., Laj, P., Hitzenberger, R., Schwarz, J. P., and Gysel,  
 1067 M.: Single Particle Soot Photometer intercomparison at the AIDA chamber, *Atmos. Meas. Tech.*, 5,  
 1068 3077-3097, doi:10.5194/amt-5-3077-2012, 2012b.

1069 Lack, D., Moosmüller, H., McMeeking, G., Chakrabarty, R., and Baumgardner, D.:  
 1070 Characterizing elemental, equivalent black, and refractory black carbon aerosol particles: a review of  
 1071 techniques, their limitations and uncertainties, *Anal Bioanal Chem*, 406, 99-122, doi:10.1007/s00216-  
 1072 013-7402-3, 2014.

1073 Lack, D. A. and Cappa, C. D.: Impact of brown and clear carbon on light absorption  
 1074 enhancement, single scatter albedo and absorption wavelength dependence of black carbon, *Atmos.*  
 1075 *Chem. Phys.*, 10, 4207-4220, doi:10.5194/acp-10-4207-2010, 2010.

1076 Lack, D. A. and Langridge, J. M.: On the attribution of black and brown carbon light absorption  
 1077 using the Angstrom exponent, *Atmos. Chem. Phys.*, 13, 10535-10543, doi:10.5194/acp-13-10535-2013,  
 1078 2013.

1079 Lack, D. A., Richardson, M. S., Law, D., Langridge, J. M., Cappa, C. D., McLaughlin, R. J., and  
 1080 Murphy, D. M.: Aircraft Instrument for Comprehensive Characterization of Aerosol Optical Properties,  
 1081 Part 2: Black and Brown Carbon Absorption and Absorption Enhancement Measured with Photo  
 1082 Acoustic Spectroscopy, *Aerosol Sci. Technol.*, 46, 555-568, doi:10.1080/02786826.2011.645955, 2012.

1083 Langridge, J. M., Richardson, M. S., Lack, D., Law, D., and Murphy, D. M.: Aircraft Instrument  
 1084 for Comprehensive Characterization of Aerosol Optical Properties, Part I: Wavelength-Dependent  
 1085 Optical Extinction and Its Relative Humidity Dependence Measured Using Cavity Ringdown  
 1086 Spectroscopy, *Aerosol Sci. Technol.*, 45, 1305-1318, doi:10.1080/02786826.2011.592745, 2011.

1087 Laskin, A., Moffet, R. C., Gilles, M. K., Fast, J. D., Zaveri, R. A., Wang, B. B., Nigge, P., and  
 1088 Shutthanandan, J.: Tropospheric chemistry of internally mixed sea salt and organic particles: Surprising  
 1089 reactivity of NaCl with weak organic acids, *J. Geophys. Res.-Atmos.*, 117, D15302,  
 1090 doi:10.1029/2012jd017743, 2012.

1091 Malm, W. C. and Hand, J. L.: An examination of the physical and optical properties of aerosols  
 1092 collected in the IMPROVE program, *Atmos. Environ.*, 41, 3407-3427,  
 1093 doi:10.1016/j.atmosenv.2006.12.012, 2007.



1094 Malm, W. C., Pitchford, M. L., McDade, C., and Ashbaugh, L. L.: Coarse particle speciation at  
1095 selected locations in the rural continental United States, *Atmos. Environ.*, 41, 2225-2239,  
1096 doi:10.1016/j.atmosenv.2006.10.077, 2007.

1097 Myhre, G., Samset, B. H., Schulz, M., Balkanski, Y., Bauer, S., Berntsen, T. K., Bian, H.,  
1098 Bellouin, N., Chin, M., Diehl, T., Easter, R. C., Feichter, J., Ghan, S. J., Hauglustaine, D., Iversen, T.,  
1099 Kinne, S., Kirkevåg, A., Lamarque, J. F., Lin, G., Liu, X., Luo, G., Ma, X., Penner, J. E., Rasch, P. J.,  
1100 Seland, Ø., Skeie, R. B., Stier, P., Takemura, T., Tsigaridis, K., Wang, Z., Xu, L., Yu, H., Yu, F., Yoon,  
1101 J. H., Zhang, K., Zhang, H., and Zhou, C.: Radiative forcing of the direct aerosol effect from AeroCom  
1102 Phase II simulations, *Atmos. Chem. Phys.*, 13, 1853-1877, doi:10.5194/acp-13-1853-2013, 2012.

1103 Nakayama, T., Kondo, Y., Moteki, N., Sahu, L. K., Kinase, T., Kita, K., and Matsumi, Y.: Size-  
1104 dependent correction factors for absorption measurements using filter-based photometers: PSAP and  
1105 COSMOS, *J. Aerosol Sci.*, 41, 333-343, doi:10.1016/j.jaerosci.2010.01.004, 2010.

1106 Ogren, J. A.: Comment on “Calibration and Intercomparison of Filter-Based Measurements of  
1107 Visible Light Absorption by Aerosols”, *Aerosol Sci. Technol.*, 44, 589-591,  
1108 doi:10.1080/02786826.2010.482111, 2010.

1109 Parrish, D. D., Stohl, A., Forster, C., Atlas, E. L., Blake, D. R., Goldan, P. D., Kuster, W. C., and  
1110 de Gouw, J. A.: Effects of mixing on evolution of hydrocarbon ratios in the troposphere, *J. Geophys.*  
1111 *Res.-Atmos.*, 112, D10S34, doi:10.1029/2006JD007583, 2007.

1112 Quinn, P. K., Coffman, D. J., Bates, T. S., Welton, E. J., Covert, D. S., Miller, T. L., Johnson, J.  
1113 E., Maria, S., Russell, L., Arimoto, R., Carrico, C. M., Rood, M. J., and Anderson, J.: Aerosol optical  
1114 properties measured on board the Ronald H. Brown during ACE-Asia as a function of aerosol chemical  
1115 composition and source region, *J. Geophys. Res.-Atmos.*, 109, D19S01, doi:10.1029/2003JD004010,  
1116 2004.

1117 Radney, J. G., You, R., Ma, X., Conny, J. M., Zachariah, M. R., Hodges, J. T., and Zangmeister,  
1118 C. D.: Dependence of Soot Optical Properties on Particle Morphology: Measurements and Model  
1119 Comparisons, *Environ. Sci. Technol.*, 48, 3169-3176, doi:10.1021/es4041804, 2014.

1120 Roberts, J. M., Fehsenfeld, F. C., Liu, S. C., Bollinger, M. J., Hahn, C., Albritton, D. L., and  
1121 Sievers, R. E.: Measurements of aromatic hydrocarbon ratios and NO<sub>x</sub> concentrations in the rural  
1122 troposphere - observation of air-mass photochemical aging and NO<sub>x</sub> removal, *Atmos. Environ.*, 18,  
1123 2421-2432, doi:10.1016/0004-6981(84)90012-x, 1984.

1124 Russell, P. B., Bergstrom, R. W., Shinozuka, Y., Clarke, A. D., DeCarlo, P. F., Jimenez, J. L.,  
1125 Livingston, J. M., Redemann, J., Dubovik, O., and Strawa, A.: Absorption Angstrom Exponent in

1126 AERONET and related data as an indicator of aerosol composition, *Atmos. Chem. Phys.*, 10, 1155-  
1127 1169, doi:10.5194/acp-10-1155-2010, 2010.

1128 Schnaiter, M., Linke, C., Mohler, O., Naumann, K. H., Saathoff, H., Wagner, R., Schurath, U.,  
1129 and Wehner, B.: Absorption amplification of black carbon internally mixed with secondary organic  
1130 aerosol, *J. Geophys. Res.-Atmos.*, 110, doi:10.1029/2005JD006046, 2005.

1131 Schuster, G. L., Dubovik, O., and Holben, B. N.: Angstrom exponent and bimodal aerosol size  
1132 distributions, *J. Geophys. Res.-Atmos.*, 111, D07207, doi:10.1029/2005JD006328, 2006.

1133 Schwartz, S. E.: The whitehouse effect—Shortwave radiative forcing of climate by  
1134 anthropogenic aerosols: an overview, *J. Aerosol Sci.*, 27, 359-382, doi:10.1016/0021-8502(95)00533-1,  
1135 1996.

1136 Schwarz, J. P., Gao, R. S., Fahey, D. W., Thomson, D. S., Watts, L. A., Wilson, J. C., Reeves, J.  
1137 M., Darbeheshti, M., Baumgardner, D. G., Kok, G. L., Chung, S. H., Schulz, M., Hendricks, J., Lauer,  
1138 A., Karcher, B., Slowik, J. G., Rosenlof, K. H., Thompson, T. L., Langford, A. O., Loewenstein, M.,  
1139 and Aikin, K. C.: Single-particle measurements of midlatitude black carbon and light-scattering aerosols  
1140 from the boundary layer to the lower stratosphere, *J. Geophys. Res.-Atmos.*, 111, D16207,  
1141 doi:10.1029/2006jd007076, 2006.

1142 Seinfeld, J. H. and Pandis, S. N.: *Atmospheric chemistry and physics : from air pollution to*  
1143 *climate change*, Wiley, New York, 1998.

1144 Setyan, A., Song, C., Merkel, M., Knighton, W. B., Onasch, T. B., Canagaratna, M. R.,  
1145 Worsnop, D. R., Wiedensohler, A., Shilling, J. E., and Zhang, Q.: Chemistry of new particle growth in  
1146 mixed urban and biogenic emissions – insights from CARES, *Atmos. Chem. Phys.*, 14, 6477-6494,  
1147 doi:10.5194/acp-14-6477-2014, 2014.

1148 Setyan, A., Zhang, Q., Merkel, M., Knighton, W. B., Sun, Y., Song, C., Shilling, J. E., Onasch,  
1149 T. B., Herndon, S. C., Worsnop, D. R., Fast, J. D., Zaveri, R. A., Berg, L. K., Wiedensohler, A.,  
1150 Flowers, B. A., Dubey, M. K., and Subramanian, R.: Characterization of submicron particles influenced  
1151 by mixed biogenic and anthropogenic emissions using high-resolution aerosol mass spectrometry:  
1152 results from CARES, *Atmos. Chem. Phys.*, 12, 8131-8156, doi:10.5194/acp-12-8131-2012, 2012.

1153 Shilling, J. E., Zaveri, R. A., Fast, J. D., Kleinman, L., Alexander, M. L., Canagaratna, M. R.,  
1154 Fortner, E., Hubbe, J. M., Jayne, J. T., Sedlacek, A., Setyan, A., Springston, S., Worsnop, D. R., and  
1155 Zhang, Q.: Enhanced SOA formation from mixed anthropogenic and biogenic emissions during the  
1156 CARES campaign, *Atmos. Chem. Phys.*, 13, 2091-2113, doi:10.5194/acp-13-2091-2013, 2013.

1157 Tsigaridis, K., Daskalakis, N., Kanakidou, M., Adams, P. J., Artaxo, P., Bahadur, R., Balkanski,  
1158 Y., Bauer, S. E., Bellouin, N., Benedetti, A., Bergman, T., Berntsen, T. K., Beukes, J. P., Bian, H.,

1159 Carslaw, K. S., Chin, M., Curci, G., Diehl, T., Easter, R. C., Ghan, S. J., Gong, S. L., Hodzic, A., Hoyle,  
 1160 C. R., Iversen, T., Jathar, S., Jimenez, J. L., Kaiser, J. W., Kirkevåg, A., Koch, D., Kokkola, H., Lee, Y.  
 1161 H., Lin, G., Liu, X., Luo, G., Ma, X., Mann, G. W., Mihalopoulos, N., Morcrette, J. J., Müller, J. F.,  
 1162 Myhre, G., Myriokefalitakis, S., Ng, N. L., O'Donnell, D., Penner, J. E., Pozzoli, L., Pringle, K. J.,  
 1163 Russell, L. M., Schulz, M., Sciare, J., Seland, Ø., Shindell, D. T., Sillman, S., Skeie, R. B., Spracklen,  
 1164 D., Stavrou, T., Steenrod, S. D., Takemura, T., Tiitta, P., Tilmes, S., Tost, H., van Noije, T., van Zyl,  
 1165 P. G., von Salzen, K., Yu, F., Wang, Z., Wang, Z., Zaveri, R. A., Zhang, H., Zhang, K., Zhang, Q., and  
 1166 Zhang, X.: The AeroCom evaluation and intercomparison of organic aerosol in global models, *Atmos.*  
 1167 *Chem. Phys.*, 14, 10845-10895, doi:10.5194/acp-14-10845-2014, 2014.  
 1168 Virkkula, A., Ahlquist, N. C., Covert, D. S., Arnott, W. P., Sheridan, P. J., Quinn, P. K., and  
 1169 Coffman, D. J.: Modification, calibration and a field test of an instrument for measuring light absorption  
 1170 by particles, *Aerosol Sci. Technol.*, 39, 68-83, doi:10.1080/027868290901963, 2005.  
 1171 Wang, W., Rood, M. J., Carrico, C. M., Covert, D. S., Quinn, P. K., and Bates, T. S.: Aerosol  
 1172 optical properties along the northeast coast of North America during the New England Air Quality  
 1173 Study - Intercontinental Transport and Chemical Transformation 2004 campaign and the influence of  
 1174 aerosol composition, *J. Geophys. Res.-Atmos.*, 112, D10S23, doi:10.1029/2006JD007579, 2007.  
 1175 Warneke, C., de Gouw, J. A., Edwards, P. M., Holloway, J. S., Gilman, J. B., Kuster, W. C.,  
 1176 Graus, M., Atlas, E., Blake, D., Gentner, D. R., Goldstein, A. H., Harley, R. A., Alvarez, S.,  
 1177 Rappenglueck, B., Trainer, M., and Parrish, D. D.: Photochemical aging of volatile organic compounds  
 1178 in the Los Angeles basin: Weekday-weekend effect, *J. Geophys. Res.-Atmos.*, 118, 5018-5028,  
 1179 doi:10.1002/jgrd.50423, 2013.  
 1180 Warneke, C., McKeen, S. A., de Gouw, J. A., Goldan, P. D., Kuster, W. C., Holloway, J. S.,  
 1181 Williams, E. J., Lerner, B. M., Parrish, D. D., Trainer, M., Fehsenfeld, F. C., Kato, S., Atlas, E. L.,  
 1182 Baker, A., and Blake, D. R.: Determination of urban volatile organic compound emission ratios and  
 1183 comparison with an emissions database, *J. Geophys. Res.-Atmos.*, 112, D10S47,  
 1184 doi:10.1029/2006JD007930, 2007.  
 1185 Yang, M., Howell, S. G., Zhuang, J., and Huebert, B. J.: Attribution of aerosol light absorption  
 1186 to black carbon, brown carbon, and dust in China – interpretations of atmospheric measurements during  
 1187 EAST-AIRE, *Atmos. Chem. Phys.*, 9, 2035-2050, doi:10.5194/acp-9-2035-2009, 2009.  
 1188 Zaveri, R. A., Shaw, W. J., Cziczo, D. J., Schmid, B., Ferrare, R. A., Alexander, M. L.,  
 1189 Alexandrov, M., Alvarez, R. J., Arnott, W. P., Atkinson, D. B., Baidar, S., Banta, R. M., Barnard, J. C.,  
 1190 Beranek, J., Berg, L. K., Brechtel, F., Brewer, W. A., Cahill, J. F., Cairns, B., Cappa, C. D., Chand, D.,  
 1191 China, S., Comstock, J. M., Dubey, M. K., Easter, R. C., Erickson, M. H., Fast, J. D., Floerchinger, C.,

1192 Flowers, B. A., Fortner, E., Gaffney, J. S., Gilles, M. K., Gorkowski, K., Gustafson, W. I., Gyawali, M.,  
 1193 Hair, J., Hardesty, R. M., Harworth, J. W., Herndon, S., Hiranuma, N., Hostetler, C., Hubbe, J. M.,  
 1194 Jayne, J. T., Jeong, H., Jobson, B. T., Kassianov, E. I., Kleinman, L. I., Kluzek, C., Knighton, B.,  
 1195 Kolesar, K. R., Kuang, C., Kubátová, A., Langford, A. O., Laskin, A., Laulainen, N., Marchbanks, R.  
 1196 D., Mazzoleni, C., Mei, F., Moffet, R. C., Nelson, D., Obland, M. D., Oetjen, H., Onasch, T. B., Ortega,  
 1197 I., Ottaviani, M., Pekour, M., Prather, K. A., Radney, J. G., Rogers, R. R., Sandberg, S. P., Sedlacek, A.,  
 1198 Senff, C. J., Senum, G., Setyan, A., Shilling, J. E., Shrivastava, M., Song, C., Springston, S. R.,  
 1199 Subramanian, R., Suski, K., Tomlinson, J., Volkamer, R., Wallace, H. W., Wang, J., Weickmann, A.  
 1200 M., Worsnop, D. R., Yu, X. Y., Zelenyuk, A., and Zhang, Q.: Overview of the 2010 Carbonaceous  
 1201 Aerosols and Radiative Effects Study (CARES), *Atmos. Chem. Phys.*, 12, 7647-7687, doi:10.5194/acp-  
 1202 12-7647-2012, 2012.  
 1203 Zelenyuk, A., Imre, D., Nam, E. J., Han, Y. P., and Mueller, K.: ClusterSculptor: Software for  
 1204 expert-steered classification of single particle mass spectra, *Int. J. Mass Spectrom.*, 275, 1-10,  
 1205 doi:10.1016/j.ijms.2008.04.033, 2008.  
 1206 Zelenyuk, A., Yang, J., Choi, E., and Imre, D.: SPLAT II: An Aircraft Compatible, Ultra-  
 1207 Sensitive, High Precision Instrument for In-Situ Characterization of the Size and Composition of Fine  
 1208 and Ultrafine Particles, *Aerosol Sci. Technol.*, 43, 411-424, doi:10.1080/02786820802709243, 2009.  
 1209 Zhang, Q., Jimenez, J. L., Canagaratna, M. R., Ulbrich, I. M., Ng, N. L., Worsnop, D. R., and  
 1210 Sun, Y. L.: Understanding atmospheric organic aerosols via factor analysis of aerosol mass  
 1211 spectrometry: a review, *Anal. Bioanal. Chem.*, 401, 3045-3067, doi:10.1007/s00216-011-5355-y, 2011.  
 1212  
 1213  
 1214

1215 **Table 1.** Table of instrumentation.

Instrument	Property Measured	Site
UCD Photoacoustic Spectrometer (PAS) <sup>a</sup>	Dry PM <sub>2.5</sub> light absorption at 405 nm and 532 nm	T0
UCD Cavity Ringdown Spectrometer (CRDS) <sup>a</sup>	Dry PM <sub>2.5</sub> light extinction at 405 nm and 532 nm; humidified particle extinction at 532 nm	T0
Particle Soot Absorption Photometer (PSAP) <sup>b</sup>	Dry PM <sub>1</sub> and PM <sub>10</sub> light absorption at 470, 532 and 660 nm	T0, T1
Nephelometer <sup>b</sup>	Dry PM <sub>1</sub> and PM <sub>10</sub> light scattering at 450, 550 and 700 nm	T0, T1
Aerodyne High Resolution Time of Flight Aerosol Mass Spectrometer (HR-ToF-AMS)	Non-refractory PM <sub>1</sub> composition (NR-PM <sub>1</sub> ); Organic aerosol types through positive matrix factor analysis	T0, T1
PNNL Single Particle Laser Ablation Time of Flight Mass Spectrometer (SPLAT-II)	Single particle composition and identification for PM <sub>0.05</sub> -PM <sub>2</sub> (optimized for PM <sub>0.1-0.6</sub> )	T0
Particle Ablation Laser-desorption Mass Spectrometer (PALMS)	Single particle composition and identification for PM <sub>0.15</sub> -PM <sub>2</sub>	T1
Single Particle Soot Photometer (SP2)	Refractory black carbon (rBC) number and mass concentration and size distributions	T0, T1
Scanning mobility particle sizer (SMPS)	PM <sub>1</sub> particle mobility size distributions	T0, T1
Aerodynamic particle sizer (APS)	PM <sub>0.7</sub> -PM <sub>10</sub> aerodynamic size distributions	T0, T1
NO <sub>x</sub> chemiluminescence	NO + NO <sub>2</sub> (gas-phase)	T0
NO <sub>y</sub> by thermal conversion and chemiluminescence	Nitrogen oxides (NO + NO <sub>2</sub> + HNO <sub>3</sub> + alkyl nitrates + peroxy nitrates)	T0
Proton Transfer Reaction Mass Spectrometer (PTR-MS)	Concentrations of select volatile organic compounds (specifically, benzene and toluene)	T0, T1

<sup>a</sup>These instruments sampled either ambient particles or particles that had been thermodenuded at 225 °C, switching on a 2.5 or 5 minute cycle

<sup>b</sup> These instruments alternately sampled PM<sub>1</sub> or PM<sub>10</sub> on a 6 minute cycle

1216

1217

1218 **Table 2.** Campaign average optical properties at T0 and T1 for submicron and supermicron particles.

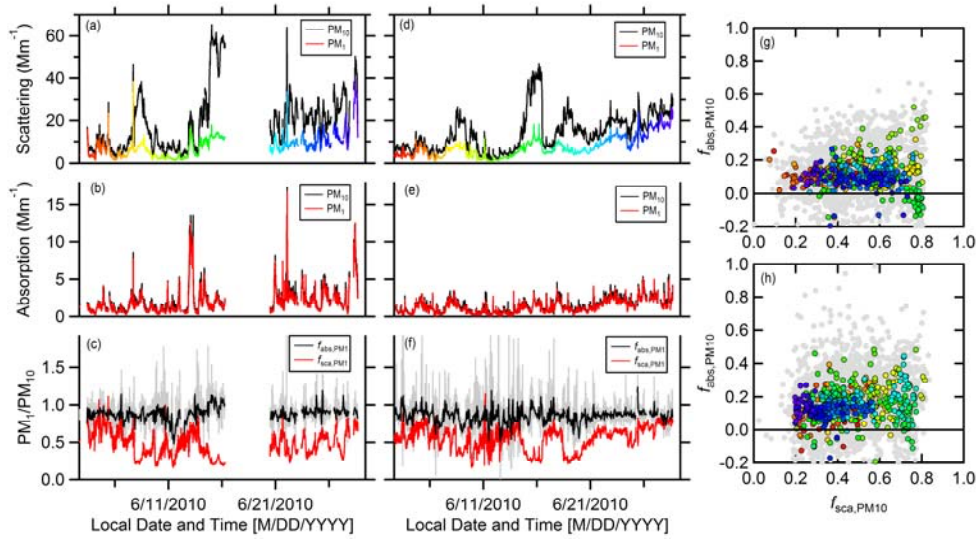
Property	T0			T1	
	PM <sub>1</sub>	PM <sub>2.5</sub>	supermicron <sup>+</sup>	PM <sub>1</sub>	supermicron <sup>+</sup>
$b_{sca,450}$	12.9 Mm <sup>-1</sup>		10.7 Mm <sup>-1</sup>	12.7 Mm <sup>-1</sup>	6.6 Mm <sup>-1</sup>
$b_{sca,550}$	7.9 Mm <sup>-1</sup>		10.9 Mm <sup>-1</sup>	7.6 Mm <sup>-1</sup>	6.8 Mm <sup>-1</sup>
$b_{sca,700}$	4.2 Mm <sup>-1</sup>		10.9 Mm <sup>-1</sup>	3.4 Mm <sup>-1</sup>	6.8 Mm <sup>-1</sup>
$b_{abs,470}$	2.3 Mm <sup>-1</sup>		0.31 Mm <sup>-1</sup>	1.45 Mm <sup>-1</sup>	0.26 Mm <sup>-1</sup>
$b_{abs,530}$	1.9 Mm <sup>-1</sup>		0.25 Mm <sup>-1</sup>	1.25 Mm <sup>-1</sup>	0.20 Mm <sup>-1</sup>
$b_{abs,660}$	1.5 Mm <sup>-1</sup>		0.19 Mm <sup>-1</sup>	0.95 Mm <sup>-1</sup>	0.14 Mm <sup>-1</sup>
$b_{ext,405}$		27.0 Mm <sup>-1</sup>			
$b_{ext,532}$		18.0 Mm <sup>-1</sup>			
$b_{abs,405}$		2.8 Mm <sup>-1</sup>			
$b_{abs,532}$		2.1 Mm <sup>-1</sup>			
$AAE_{470-532}^{\#}$	1.21 ± 0.18		1.93 ± 0.83	1.22 ± 0.33	2.03 ± 1.04
$AAE_{470-660}^{\#}$	1.17 ± 0.11		1.54 ± 0.50	1.28 ± 0.22	1.76 ± 0.69
$AAE_{532-660}^{\#}$	1.15 ± 0.12		1.30 ± 0.52	1.28 ± 0.21	1.68 ± 0.77
$AAE_{405-532}^{\#}$		1.3 ± 0.9			
$SAE_{450-550}^*$	2.42 ± 0.38		-0.13 ± 0.31	2.58 ± 0.27	-0.15 ± 0.34
$EAE_{405-532}^*$		1.53 ± 0.5			

<sup>+</sup> Values for supermicron particles are calculated as the difference between PM<sub>10</sub> and PM<sub>1</sub>.

<sup>#</sup> The reported uncertainties were determined from fitting a histogram of the observed values to a Gaussian distribution and are the 1 $\sigma$  spread.

<sup>\*</sup> The reported uncertainties are 1 $\sigma$  standard deviations.

1224



1225

1226 **Figure 1.** Time-series of  $\text{PM}_1$  and  $\text{PM}_{10}$  scattering (a and d) and absorption (b and e) coefficients at 550  
 1227 nm for T0 (left panels) and T1 (right panels). Values for  $\text{PM}_{10}$  are shown as black lines and for  $\text{PM}_1$  as  
 1228 colored lines. The ratio between  $\text{PM}_1$  and  $\text{PM}_{10}$  scattering (red) and absorption (black) are shown in panels  
 1229 c and f. (For absorption, the data have been further averaged to 1 hour; the higher time resolution data are  
 1230 shown as gray.) The co-variation between  $f_{\text{abs,PM10}}$  and  $f_{\text{sca,PM10}}$  for T0 (g) and T1 (h) are also shown. The  
 1231 1-hr averaged points are colored according to time during the campaign, and correspond to the time-series  
 1232 in panels a and d; the gray points are the data at higher time-resolution.

1233

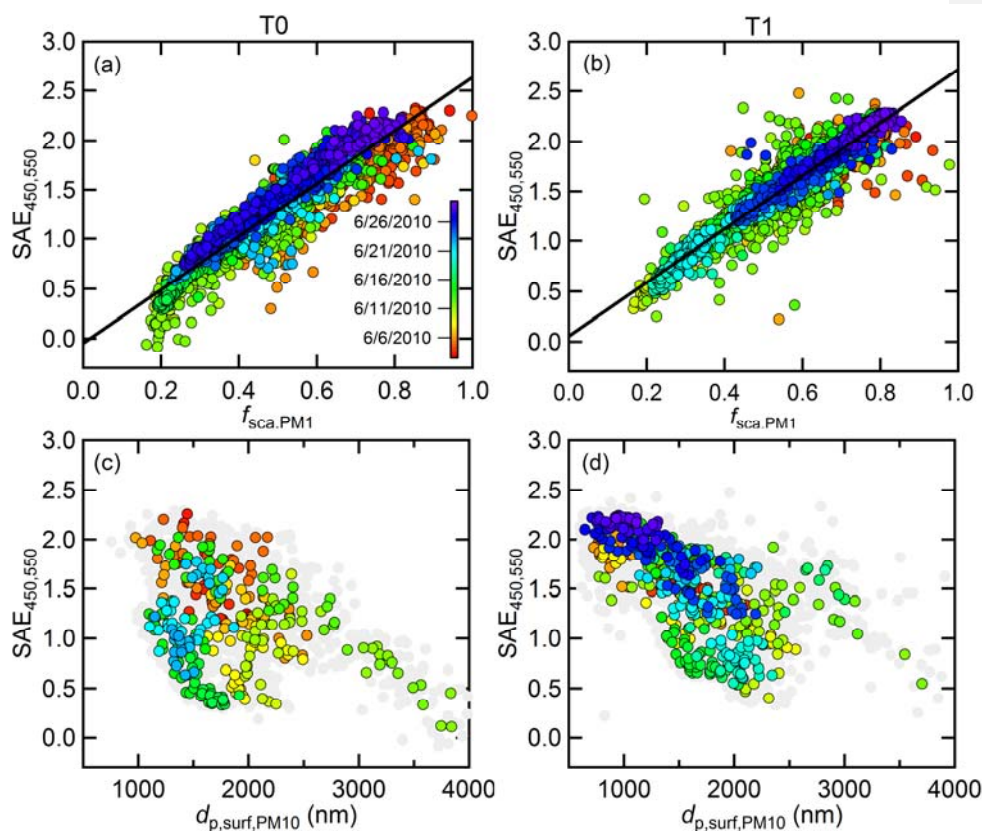


**Figure 2.** (a,b) The relationship between the  $\text{PM}_{10}$  scattering Ångstrom exponent for the 450-550 nm pairs and the  $f_{\text{sca},\text{PM}1}$  for both T0 (left panels) and T1 (right panels). (c,d) The relationship between the  $\text{SAE}$  and the median surface-weighted diameter for  $\text{PM}_{10}$ . The points in all graphs are colored according to time during the campaign (see legend). For panels (a,b) data at 10 min resolution are shown, while in panels (c,d) the colored points are for data averaged to 1 h and the gray points are for 10 min data. The fewer colored points in panel (c) is the result of a malfunction of the APS after 22 June 2010, which precludes calculation of  $d_{\text{p,surf},\text{PM}10}$ .

Formatted: Font: Italic



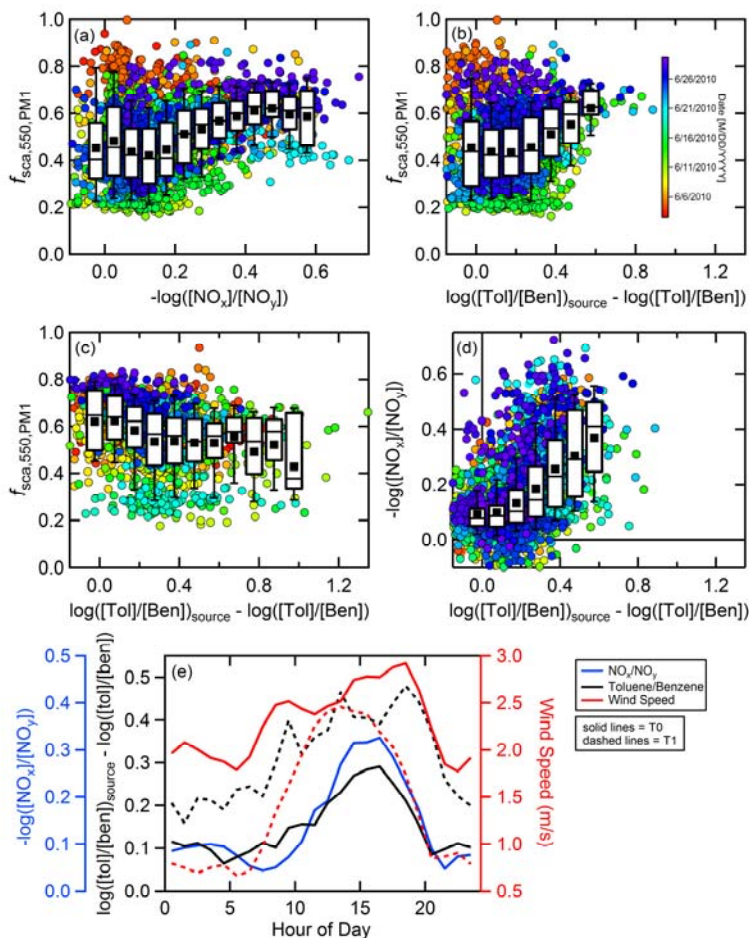


**Figure 3.** Submicron fraction of scattering for the T0 and T1 sites as a function of photochemical age proxies. Observations at T0 using the (a)  $NO_x/NO_y$  ratio and the (b) toluene/benzene ratio and at T1 for the (c) toluene/benzene ratio as the PCA proxy. Individual measurements (averaged to 10 minutes) are colored by time. (d) The relationship between the two PCA estimation methods at T0. (e) The diurnal variation in the PCA estimation methods and the measured wind speed for T0 (solid lines) and T1 (dashed lines). Box and whisker plots show the median (line), mean (square) upper and lower quartile (box) and 10<sup>th</sup> and 90<sup>th</sup> percentile (whiskers).

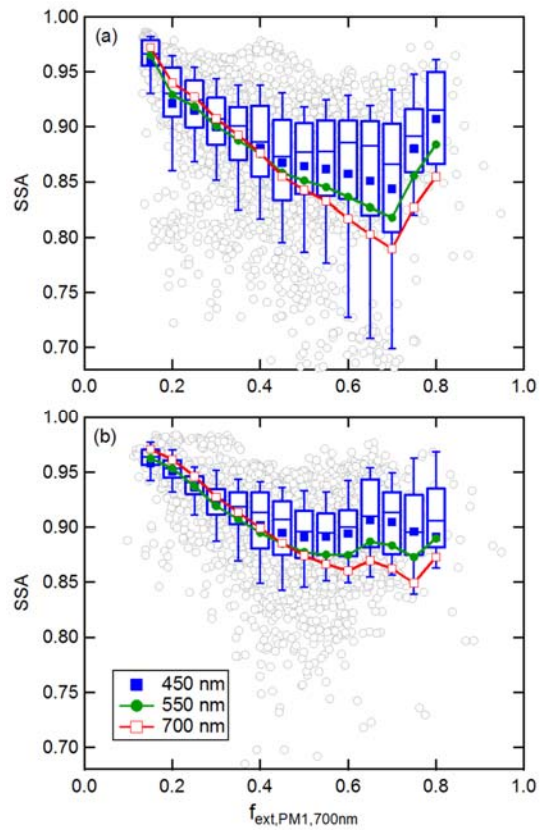


**Figure 4.** Relationship between the  $PM_{10}$  SSA and the  $PM_1$  fraction of extinction at 700 nm,  $f_{ext,PM1,700}$ , for the (a) T0 and (b) T1 sites. The individual data points (gray, circles) are shown for the  $SSA_{PM10}$  at 450 nm along with a box-and-whisker plot binned by  $f_{ext,PM1,700}$ . For the  $SSA_{PM10}$  at 550 nm (green line) and 700 nm (red line) only the mean, binned values are shown.

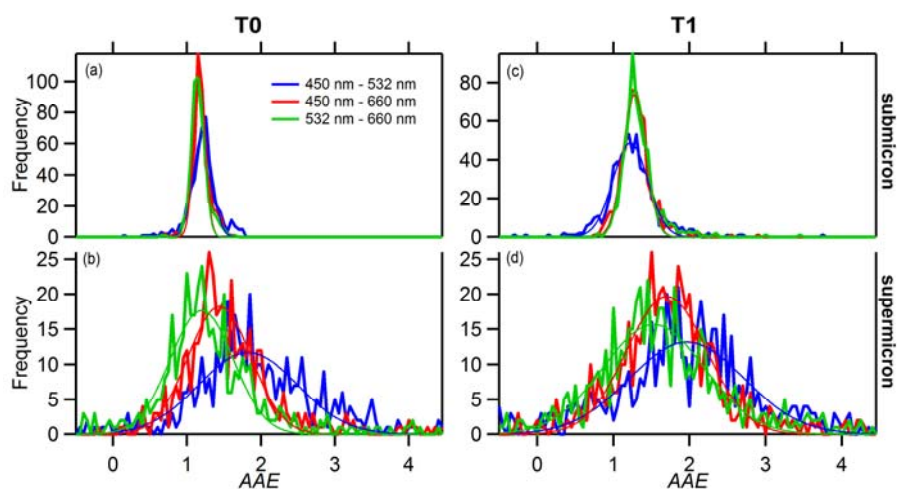
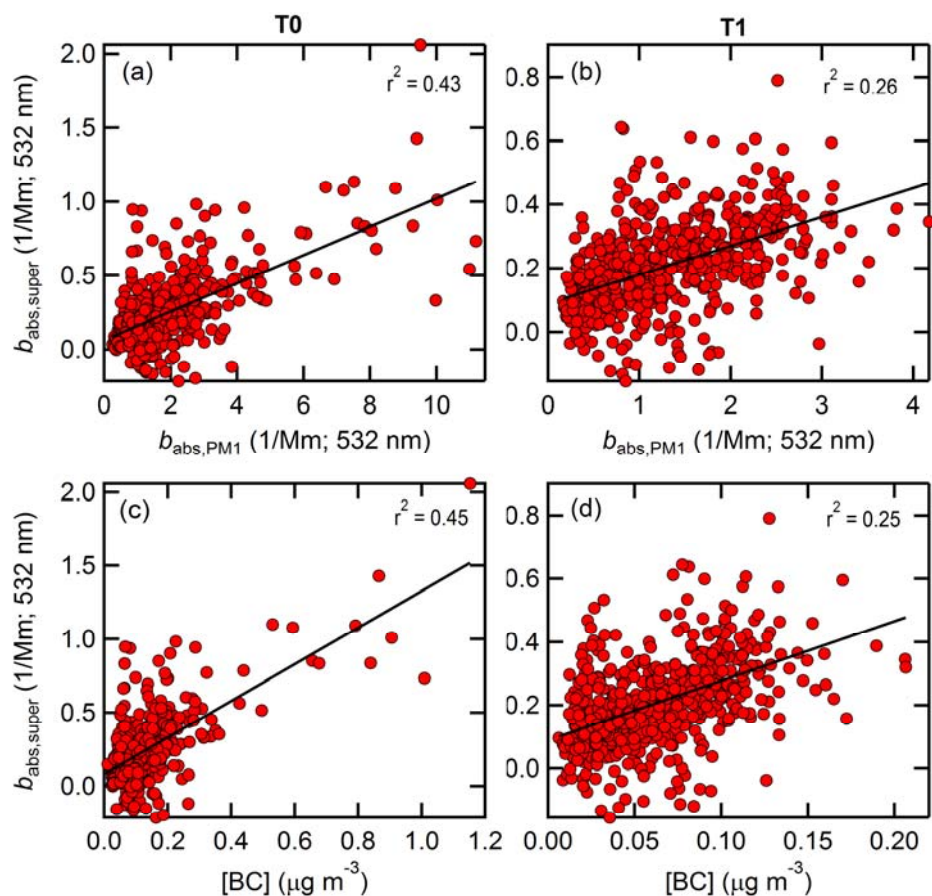


**Figure 5.** Histograms of the measured *AAE* values for various wavelength pairs for submicron (top; a and c) and supermicron (bottom; b and d) particles at the T0 (left) and T1 (right) sites. The different colors correspond to different wavelength pairs (see legend). The thick lines correspond to the observations while the thin lines show the results from fitting of the distributions to a Gaussian function.

Deleted: 4

1266

1267



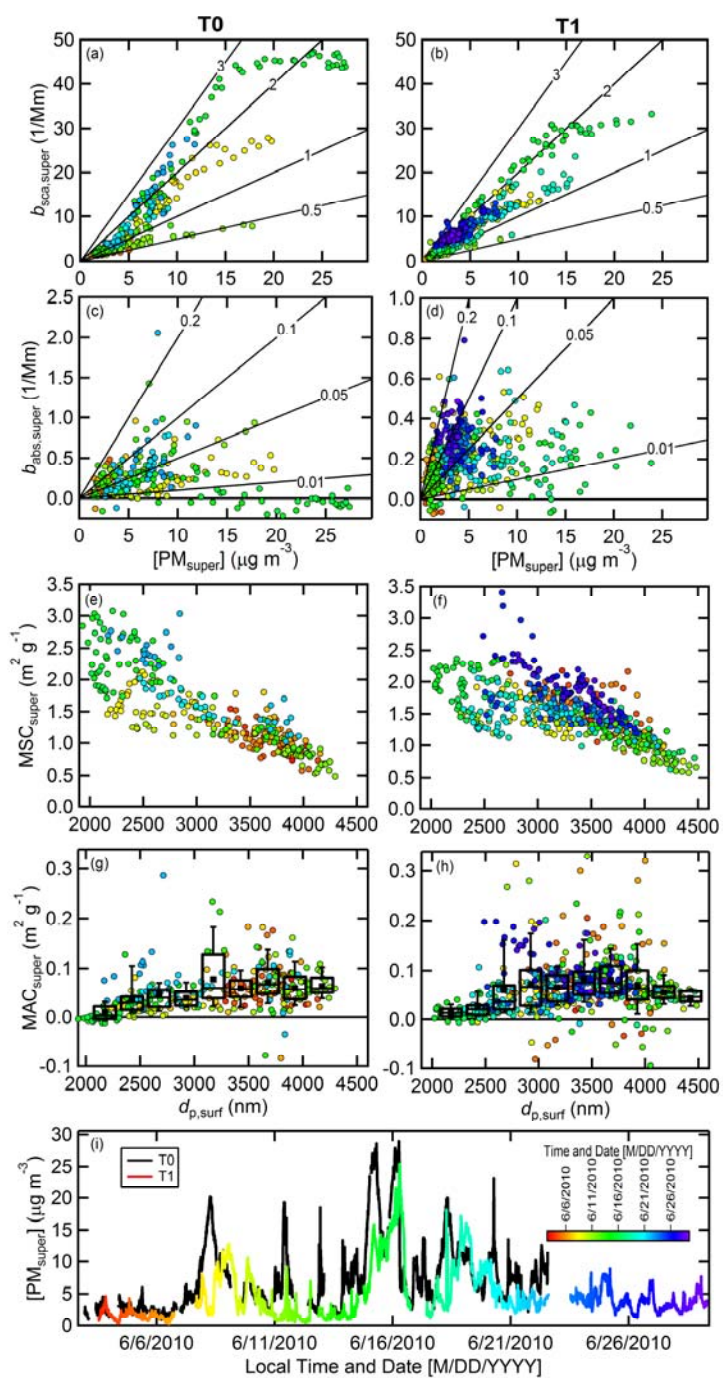
1268

1269

1270 **Figure 6.** Co-variation of the supermicron absorption at T0 (left panels) and T1 (right panels) with the  
 1271 submicron absorption (top panels) and with black carbon concentration (bottom panels). Note that  
 1272 negative values of  $b_{\text{abs,super}}$  result from this being derived from the difference between  $b_{\text{abs,PM10}}$  and  $b_{\text{abs,PM1}}$ .

1273

Deleted: 5



1276 **Figure 7.** (a,b) Scatter plot between  $b_{\text{sca,super}}$  at 532 nm and  $[\text{PM}_{\text{super}}]$  for (left panels) T0 and (right panels)  
1277 T1. The lines correspond to different  $MSC$  values (in  $\text{m}^2 \text{g}^{-1}$ ). (c,d) Scatter plot between  $b_{\text{abs,super}}$  at 532 nm  
1278 and  $[\text{PM}_{\text{super}}]$ . The lines correspond to different  $MAC$  values (in  $\text{m}^2 \text{g}^{-1}$ ). (e,f) The relationship between 1-  
1279 hr average  $MSC$  values and the surface area weighted mean diameter,  $d_{\text{p,surf}}$  at the two sites. (g,h) The  
1280 relationship between 1-hr average  $MAC$  values and  $d_{\text{p,surf}}$  at the two sites. The individual 1-hr average data  
1281 points are shown overlaid by box-and-whisker plots showing the mean (■), median (-), lower and upper  
1282 quartile (boxes), and 9<sup>th</sup> and 91<sup>st</sup> percentile (whiskers). The points in panels a-h are colored according to  
1283 time, and correspond to the colors in the bottom figure and color scale. (i) Time series of the supermicron  
1284 particle mass concentration for T0 and T1. T0 values are black lines, and T1 values are colored according  
1285 to time.

Deleted: 6

1286  
1287

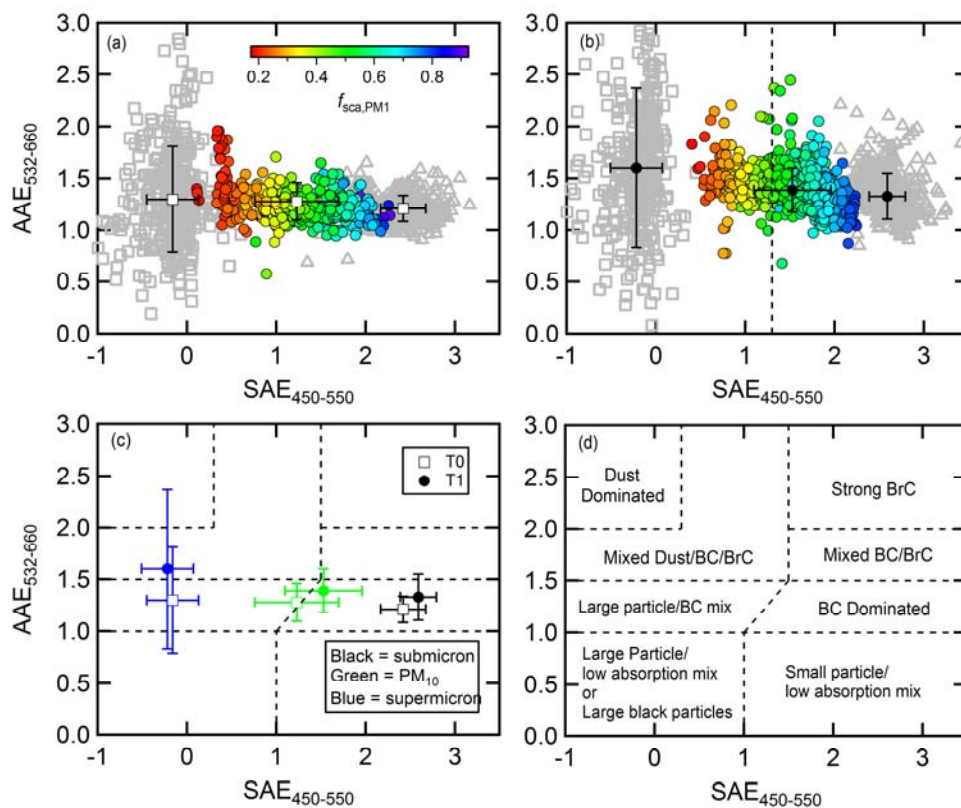


**Figure 8.** Observed relationship between the AAE (532-600 nm pair) and the SAE (450-550 nm pair) for PM<sub>10</sub> (colored circles), submicron (open grey triangles) and supermicron (open grey squares) particles for the (a) T0 and (b) T1 sites. (c) Comparison between the PM<sub>10</sub> (green), submicron (black) and supermicron (blue) particle averages between the T0 (filled circles) and T1 (open squares) sites. (d) An alternate classification scheme to that suggested by Cazorla et al. (2013).

Deleted: 7



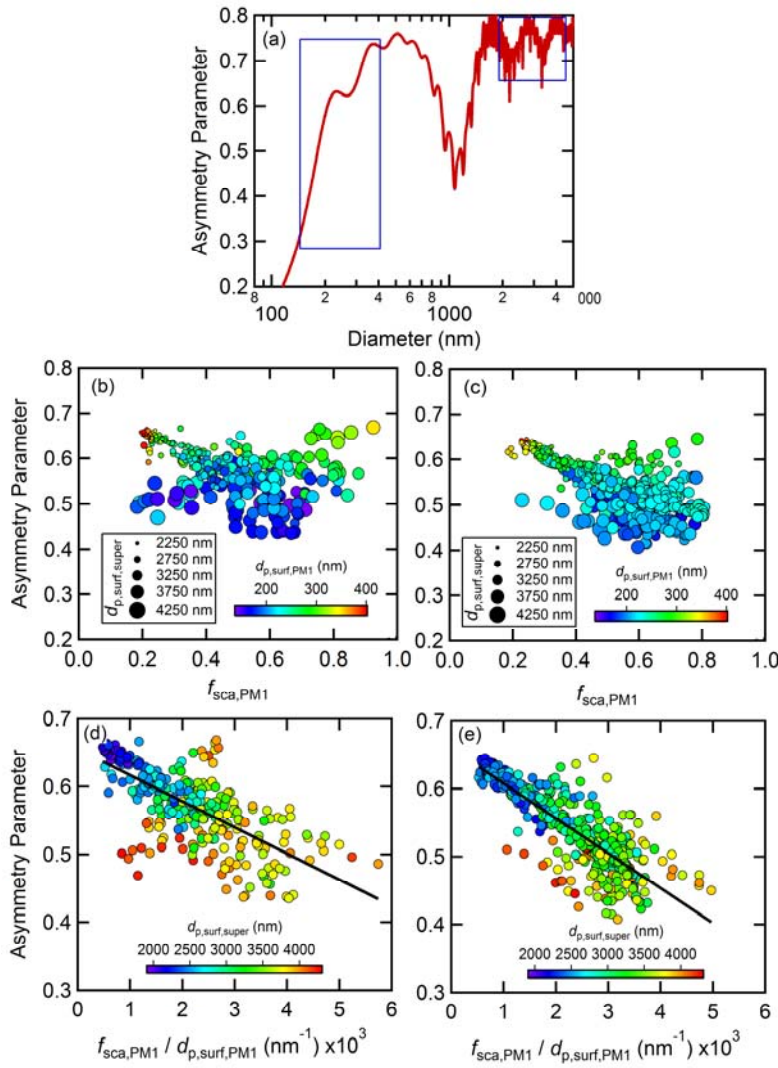
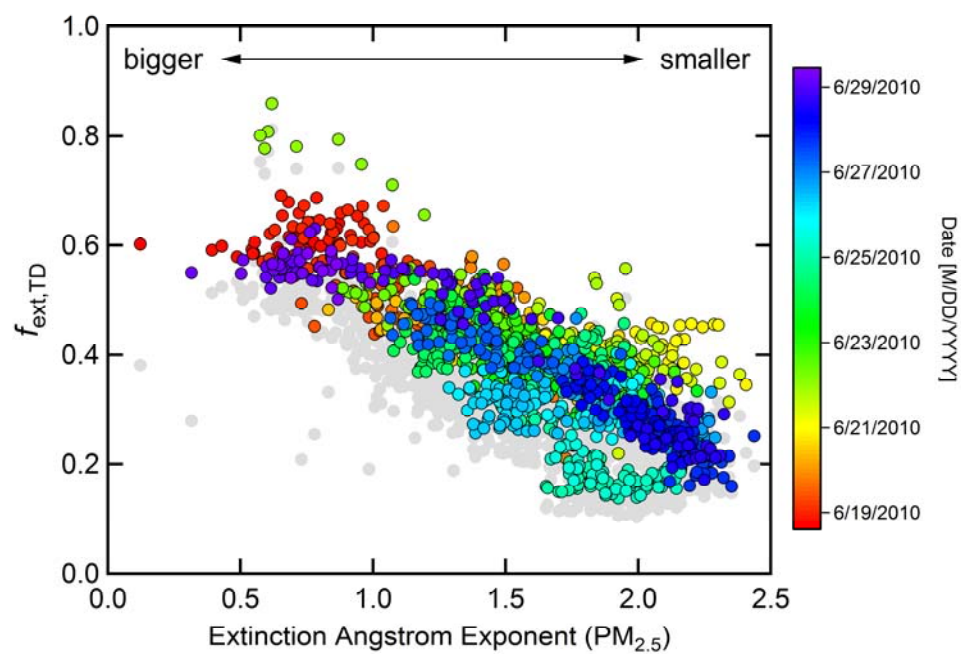


**Figure 2.** (a) Theoretical variation in the asymmetry parameter,  $g_{sca}$ , with particle diameter, assuming spherical particles with  $RI = 1.5 + 0.0i$ . The blue boxes indicate the range of  $d_{p,surf}$  values observed for submicron and supermicron particles. (b,c) The observed dependence of  $g_{sca}$  on  $f_{sca,PM1}$  for (b) T0 and (c) T1. The points are colored according to  $d_{p,surf,PM1}$  and the point size corresponds to  $d_{p,surf,super}$ . (d,e) The relationship between  $g_{sca}$  and  $R_g = f_{sca,PM1}/d_{p,surf,PM1}$  for (d) T0 and (e) T1. The points are colored according to  $d_{p,surf,super}$ .

Deleted: 8



1305



1306

1307 **Figure 10.** Variation of the extinction fraction remaining at 532 nm (colored points) and 405 nm (gray  
1308 points) as a function of the observed ambient particle extinction Ångstrom exponent for  $PM_{2.5}$ . The points  
1309 are colored by date.

1310

1311

Deleted: 9

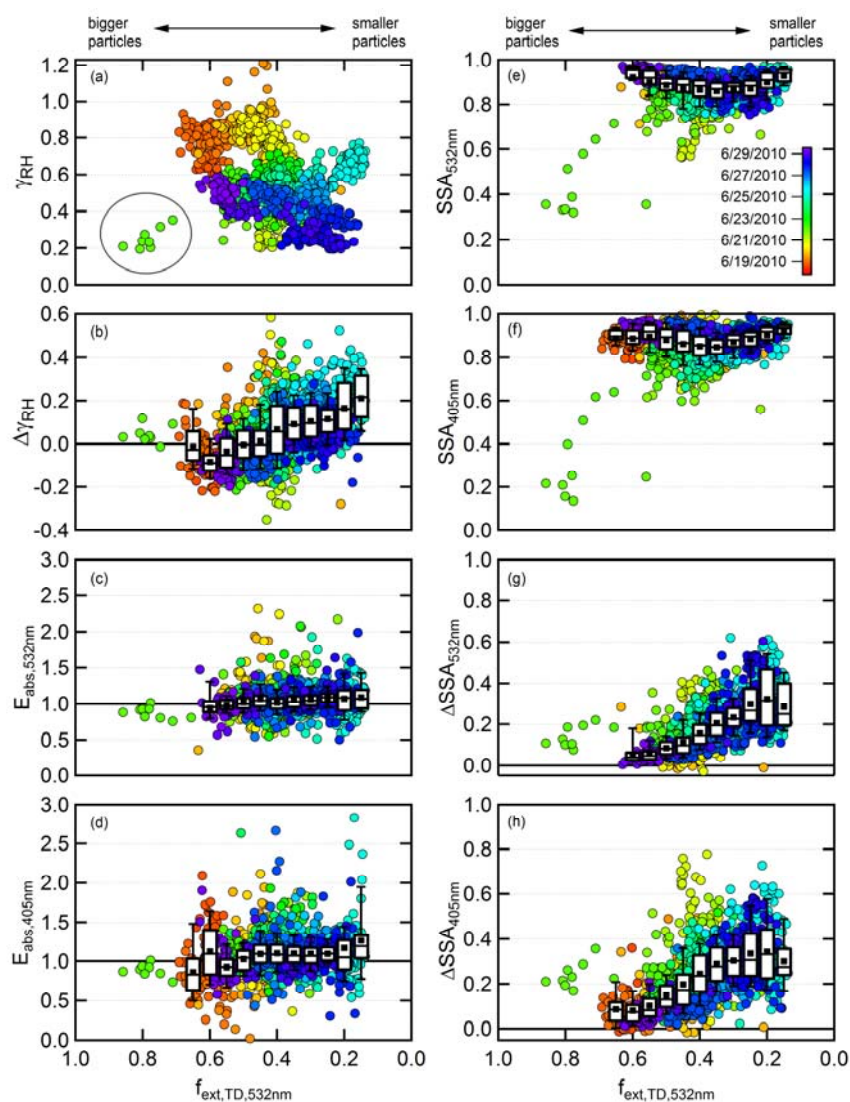


**Figure 11.** Dependence of various intensive parameters on the fraction of extinction remaining after heating in the thermodenuder. Data are shown for (a) the absolute  $\gamma_{RH}$ , (b) the change in  $\gamma_{RH}$  (c) the absorption enhancement at 532 nm, (d) the absorption enhancement at 405 nm, (e) the SSA at 532 nm, (f) the SSA at 405 nm, (g) the change in SSA at 532 nm and (h) the change in SSA at 405 nm. The points are colored by time. The circled points in (a) show the period that was impacted by local road resurfacing activities.

Deleted: 10

1 The Supplemental Material contains [three](#) tables (Table S1-[S3](#)) and [eleven](#) figures (Figure S1-[S11](#))  
2 to provide additional information about and support for the results presented in the manuscript main text.

3

- Deleted: one
- Deleted: eight
- Deleted: S8

7 **Table S1.** Summary of abbreviations and symbols used in this work.

Symbol	Definition
$PC_{ANOx}$	Average photochemical age of the air mass
$PC_{AHC}$	Average photochemical age of the air mass
$PM_1$	Particulate matter with aerodynamic diameter $< 1 \mu m$
$PM_{10}$	Particulate matter with aerodynamic diameter $< 10 \mu m$
$PM_{super}$	Particulate matter with aerodynamic diameter between 1 and $10 \mu m$
$I_{sca,super}$	Scattering attributed to particles between 1 and $10 \mu m$
$I_{abs,super}$	Absorption attributed to particles between 1 and $10 \mu m$
$f_{sca,PM1}$	Fraction of scattering from particles $< 1 \mu m$ diameter (submicron)
$f_{abs,PM1}$	Fraction of absorbing from particles $< 1 \mu m$ diameter (submicron)
$f_{sca,super}$	Fraction of scattering from particles between 1 and $10 \mu m$ diameter
$f_{abs,super}$	Fraction of absorbing from particles between 1 and $10 \mu m$ diameter
$AAE_{\lambda 1, \lambda 2}$	Absorbing Ångström exponent from $\lambda 1$ and $\lambda 2$
$AAE_{PM1}$	Absorption Ångström exponent for particles $< 1 \mu m$ diameter (submicron)
$AAE_{PM10}$	Absorption Ångström exponent for particles $< 10 \mu m$ diameter
$AAE_{10-1}$	Absorption Ångström exponent for particles from 1 to $10 \mu m$ diameter
$\Delta AAE_{amb-TD}$	Difference in AAE between ambient and thermodenuded states
$SAE_{\lambda 1, \lambda 2}$	Scattering Ångström exponent from a given wavelength pair ( $\lambda 1$ and $\lambda 2$ )
$SAE_{PM1}$	Scattering Ångström exponent for particles $< 1 \mu m$ diameter (submicron)
$SAE_{PM10}$	Scattering Ångström exponent for particles $< 10 \mu m$ diameter
$\Delta SAE_{10-1}$	Difference in scattering Ångström exponent for particles from 1 to $10 \mu m$ diameter
$EAE_{PM10}$	Extinction Ångström exponent for particles $< 10 \mu m$ diameter
$EAE_{PM10-50}$	$EAE_{PM10}$ value where $f_{sca,PM1} = 0.5$
$SSA$	Single scatter albedo – fraction of extinction due to scattering
$f_{bsca}$	Fraction of light that is backscattered
$g_{sca}$	Asymmetry parameter
$f_{ext,TD}$	Fraction of extinction remaining in the thermodenuder
$\chi_{RH}$	Hygroscopicity
$\Delta \chi_{RH}$	Difference in hygroscopicity between undenuded and denuded
$MAC_{PM1}$	Mass absorption coefficient for particles $< 1 \mu m$ diameter
$MAC_{PM10}$	Mass absorption coefficient for particles $< 10 \mu m$ diameter
$MAC_{super}$	Mass absorption coefficient for particles from 1 to $10 \mu m$ diameter
$MSC_{PM1}$	Mass scattering coefficient for particles $< 1 \mu m$ diameter
$MSC_{PM10}$	Mass scattering coefficient for particles $< 10 \mu m$ diameter
$MSC_{super}$	Mass scattering coefficient for particles from 1 to $10 \mu m$ diameter
$E_{abs}$	Absorption enhancement
$AOD$	Aerosol Optical Depth
$FME$	Fine mode fraction of extinction

8

9

Formatted	... [1]
Formatted	... [2]
Formatted Table	... [3]
Formatted	... [4]
Formatted	... [5]
Formatted	... [6]
Formatted	... [7]
Formatted	... [8]
Formatted	... [9]
Formatted	... [10]
Formatted	... [11]
Formatted	... [12]
Formatted	... [13]
Formatted	... [14]
Formatted	... [15]
Formatted	... [16]
Formatted	... [17]
Formatted	... [18]
Formatted	... [19]
Formatted	... [20]
Formatted	... [21]
Formatted	... [22]
Formatted	... [23]
Formatted	... [24]
Formatted	... [25]
Formatted	... [26]
Formatted	... [27]
Formatted	... [28]
Formatted	... [29]
Formatted	... [30]
Formatted	... [31]
Formatted	... [32]
Formatted	... [33]
Formatted	... [34]
Formatted	... [35]
Formatted Table	... [36]
Formatted	... [37]
Formatted	... [38]
Formatted	... [39]
Formatted	... [40]
Formatted	... [41]
Formatted	... [42]
Formatted	... [43]
Formatted	... [44]
Formatted	... [45]
Formatted	... [46]
Formatted	... [47]
Formatted	... [48]
Formatted	... [49]
Formatted	... [50]
Formatted	... [51]
Formatted	... [52]
Formatted	... [53]

10

Table S2. Results from linear fitting of  $SAE_{PM10}$  versus  $f_{sca,PM1}$ .

Wavelength Pair <i><math>SAE_{PM10}</math></i>	Wavelength <i><math>f_{sca,PM1}</math></i> (nm)	Slope*	Intercept <sup>#</sup>
450-550	450	2.65	-0.34
450-550	550	2.69	-0.05
450-550	700	2.81	0.27
450-700	450	2.63	-0.41
450-700	550	2.70	-0.14
450-700	700	2.92	0.15
550-700	450	2.62	-0.47
550-700	550	2.71	-0.21
550-700	700	3.01	0.05
T1			
450-550	450	2.62	-0.24
450-550	550	2.66	-0.06
450-550	700	2.76	0.40
450-700	450	2.69	-0.42
450-700	550	2.76	-0.14
450-700	700	2.97	0.18
550-700	450	2.77	-0.59
550-700	550	2.85	-0.31
550-700	700	3.15	-0.02
550-700	700	3.01	0.05

\* The fit uncertainties were typically < 0.02, which is much smaller than the experimental uncertainty.

<sup>#</sup> The fit uncertainties were typically < 0.01, which is much smaller than the experimental uncertainty.

Deleted: ¶

Deleted: S1

Formatted: Font: Italic

11

12

15 **Table S3.** Summary of the  $EAE_{PM10-50}$  values dependence on the wavelength pairs used. See Figure S6  
 16 for the relevant observations.

17

$EAE_{PM10}$ Wavelength Pair (nm)	$f_{ext,PM1}$ Wavelength (nm)	$EAE_{PM10-50}$
<a href="#">450,550</a>	<a href="#">450</a>	<a href="#">0.92</a>
<a href="#">450,550</a>	<a href="#">550</a>	<a href="#">1.15</a>
<a href="#">450,550</a>	<a href="#">700</a>	<a href="#">1.42</a>
<a href="#">450,700</a>	<a href="#">450</a>	<a href="#">0.85</a>
<a href="#">450,700</a>	<a href="#">550</a>	<a href="#">1.09</a>
<a href="#">450,700</a>	<a href="#">700</a>	<a href="#">1.37</a>
<a href="#">550,700</a>	<a href="#">450</a>	<a href="#">0.79</a>
<a href="#">550,700</a>	<a href="#">550</a>	<a href="#">1.03</a>
<a href="#">550,700</a>	<a href="#">700</a>	<a href="#">1.32</a>

18

Formatted: Indent: First line: 0"

Formatted: Font: Italic

Formatted: Left, Space After: 0 pt, Line spacing: single, Position: Horizontal: Center, Relative to: Column, Vertical: 0", Relative to: Paragraph, Horizontal: 0.13", Wrap Around

Formatted Table

Formatted: Space After: 0 pt, Line spacing: single, Position: Horizontal: Center, Relative to: Column, Vertical: 0", Relative to: Paragraph, Horizontal: 0.13", Wrap Around

Formatted: Space After: 0 pt, Line spacing: single, Position: Horizontal: Center, Relative to: Column, Vertical: 0", Relative to: Paragraph, Horizontal: 0.13", Wrap Around

Formatted: Space After: 0 pt, Line spacing: single, Position: Horizontal: Center, Relative to: Column, Vertical: 0", Relative to: Paragraph, Horizontal: 0.13", Wrap Around

Formatted: Space After: 0 pt, Line spacing: single, Position: Horizontal: Center, Relative to: Column, Vertical: 0", Relative to: Paragraph, Horizontal: 0.13", Wrap Around

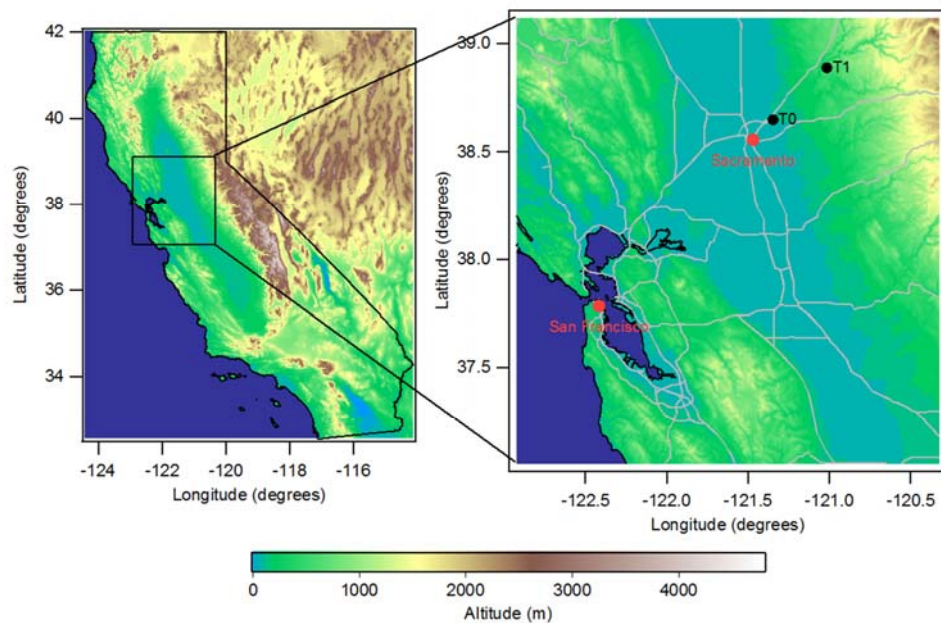
Formatted: Space After: 0 pt, Line spacing: single, Position: Horizontal: Center, Relative to: Column, Vertical: 0", Relative to: Paragraph, Horizontal: 0.13", Wrap Around

Formatted: Space After: 0 pt, Line spacing: single, Position: Horizontal: Center, Relative to: Column, Vertical: 0", Relative to: Paragraph, Horizontal: 0.13", Wrap Around

Formatted: Space After: 0 pt, Line spacing: single, Position: Horizontal: Center, Relative to: Column, Vertical: 0", Relative to: Paragraph, Horizontal: 0.13", Wrap Around

Formatted: Space After: 0 pt, Line spacing: single, Position: Horizontal: Center, Relative to: Column, Vertical: 0", Relative to: Paragraph, Horizontal: 0.13", Wrap Around

19



20

21 **Figure S1.** (left) A map of California, showing the general measurement location. (right) A closer-up view of the two  
 22 observational sites, T0 near Sacramento, CA and T1 near Cool, CA. The gray lines show the main interstate and highway  
 23 network. [Dark blue areas indicate water.](#)  
 24  
 25

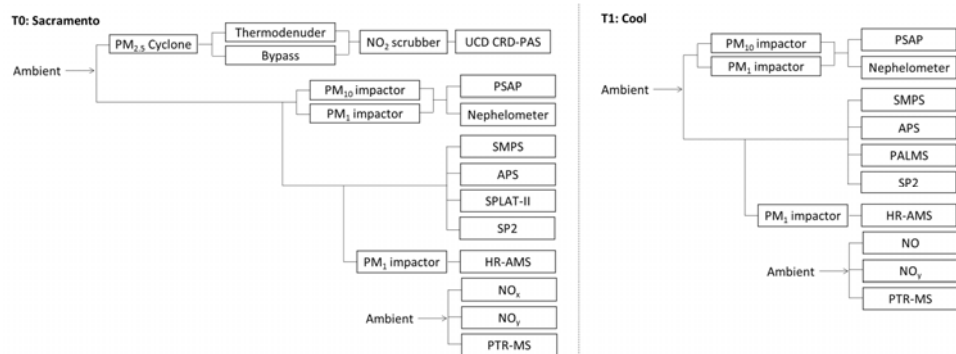
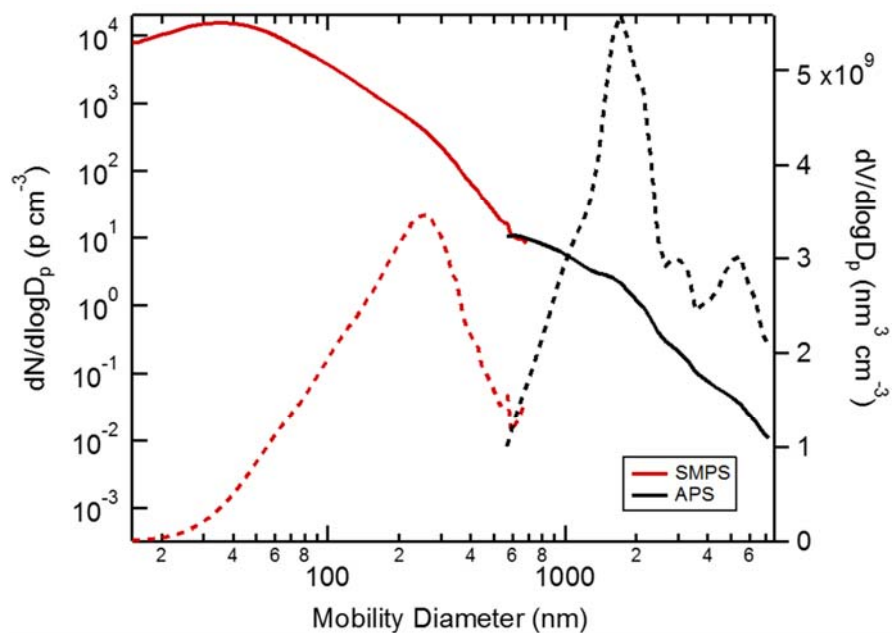


**Figure S2.** Schematic of the sampling scheme during CARES for the (left) T0 site in Sacramento and (right) T1 site in Cool.



30  
31  
32



33  
34  
35  
36  
37  
38

**Figure S3.** Merged campaign-average mobility-equivalent size distribution for the T0 site showing the measurements made using the SMPS (red) and APS (black). The APS aerodynamic diameters were adjusted to mobility-equivalent diameters assuming a material density of  $2.0 \text{ g cm}^{-3}$ . The number-weighted distribution is shown as solid lines and the volume-weighted size distribution as dashed lines.

Deleted: 2

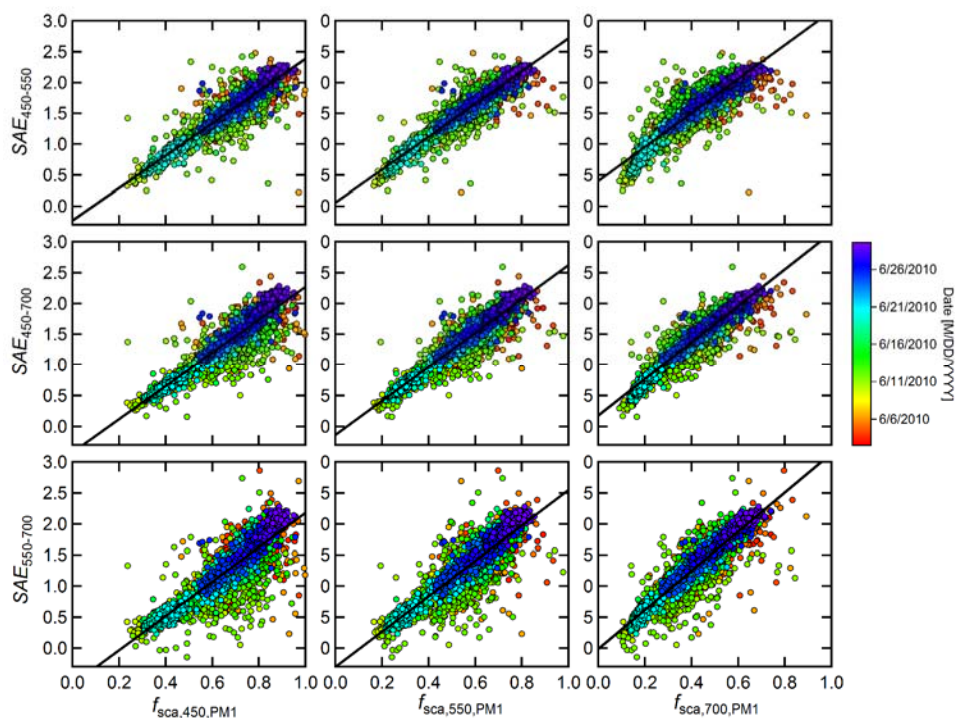
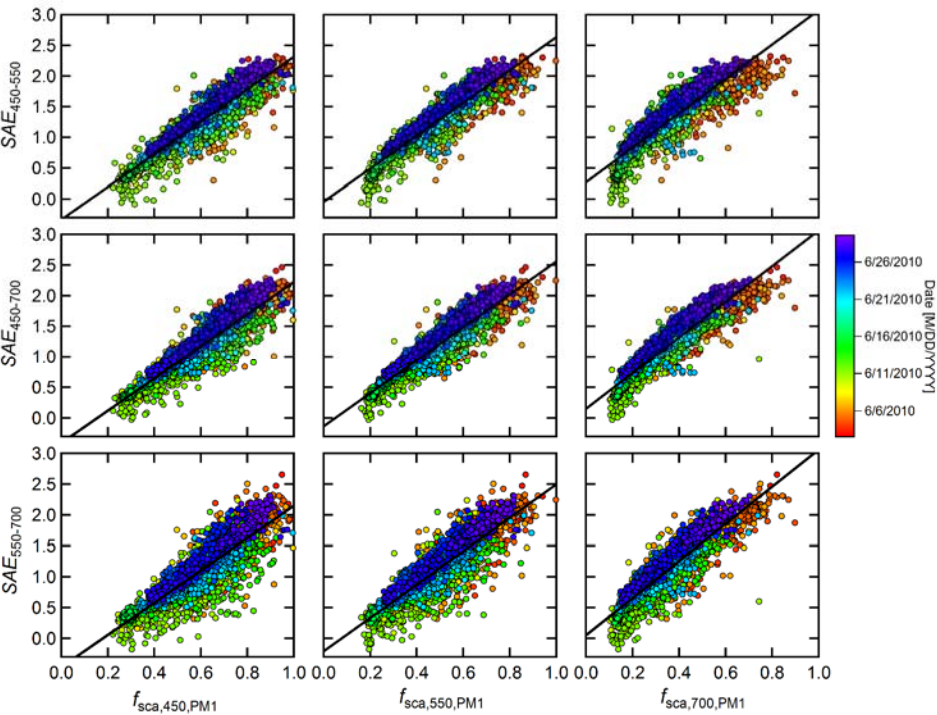


**Figure S4.** The relationship between the scattering Ångström exponent for  $PM_{10}$  for different wavelength pairs and the  $PM_{10}/PM_{10}$  scattering ratio ( $f_{sca,PM1}$ ) at different wavelengths for the T0 site. The points are colored according to time during the campaign. Slope and intercept values from the linear fits (black lines) are reported in Table S2.

Deleted: 3

Deleted: 1



50 **Figure S5.** The relationship between the scattering Ångström exponent for PM<sub>10</sub> for different wavelength pairs and the  
51 PM<sub>1</sub>/PM<sub>10</sub> scattering ratio ( $f_{sca,PM1}$ ) at different wavelengths for the T1 site. The points are colored according to time during the  
52 campaign. Slope and intercept values from the linear fits (black lines) are reported in Table S2.  
53

Deleted: 4  
Deleted: 1

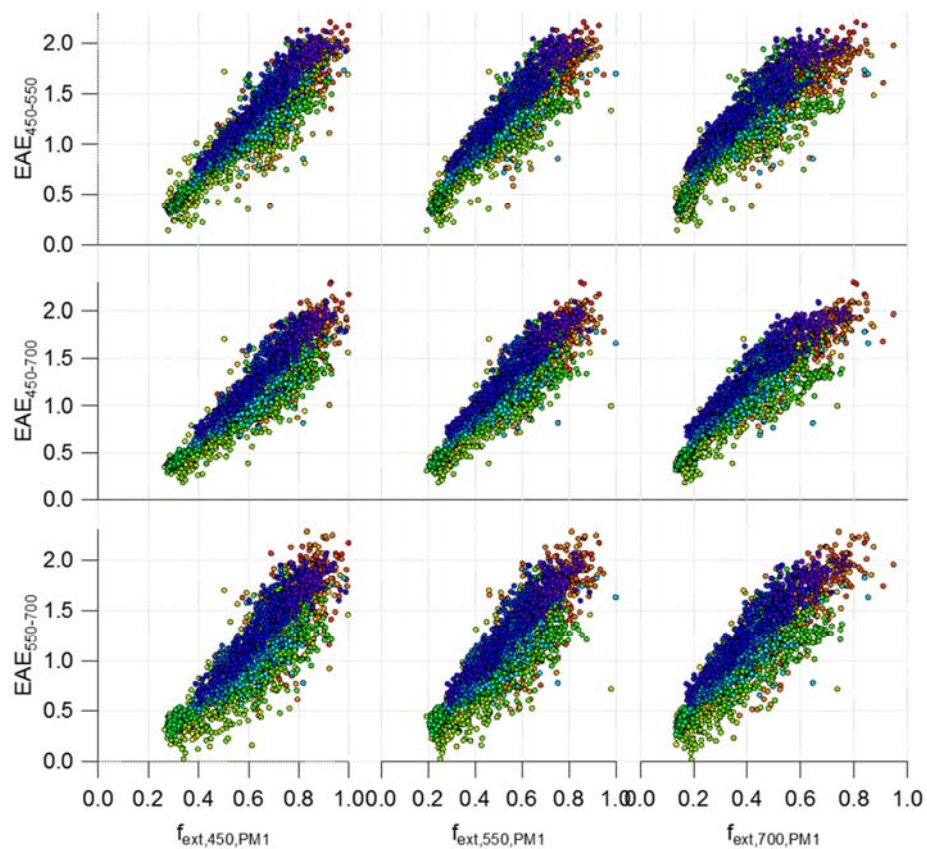


**Figure S6.** The relationship between the extinction Ångström exponent for  $PM_{10}$  for different wavelength pairs and the  $PM_1/PM_{10}$  extinction ratio ( $f_{ext,PM1}$ ) at different wavelengths for the T0 site. The points are colored according to time during the campaign, as in Figure S4. The  $EAE$  values when  $f_{ext,PM1} = 0.5$  are reported in Table S3.

Formatted: Justified

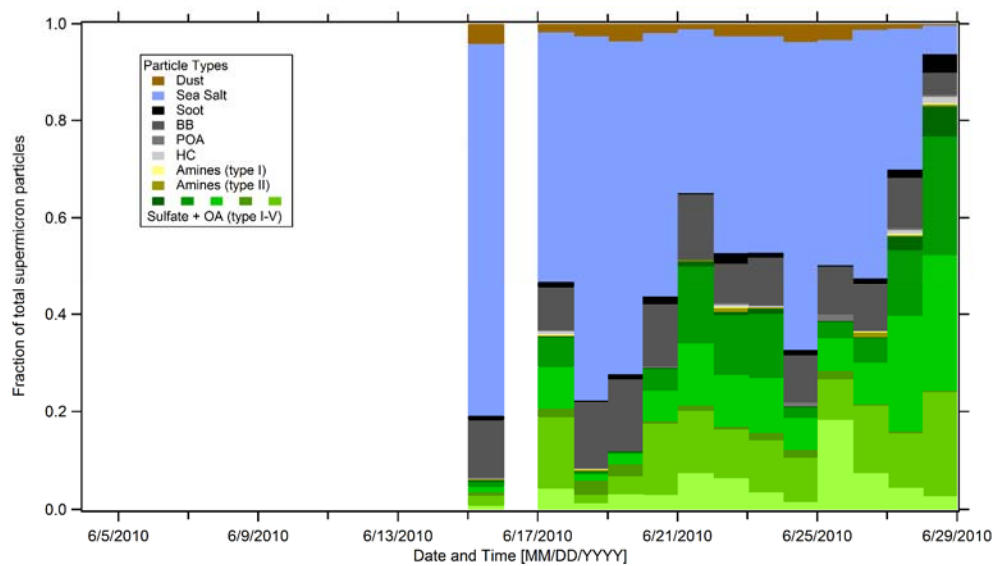
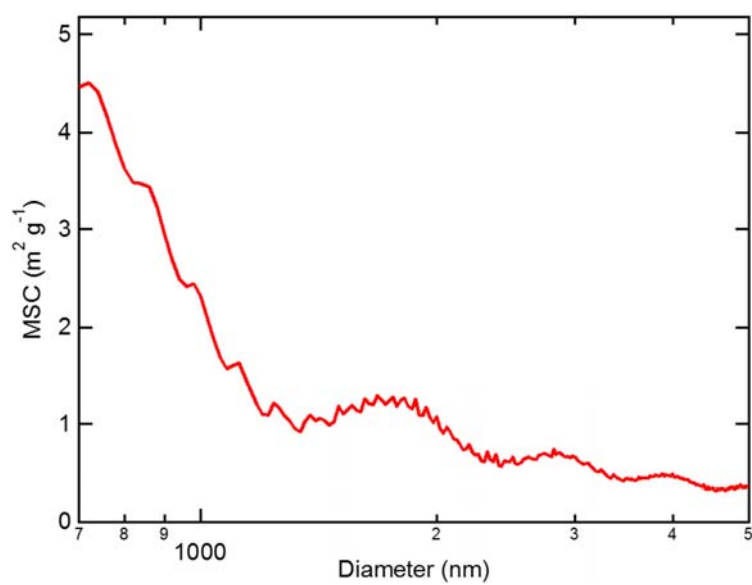


**Figure S7.** Fractional number abundance of supermicron particles ( $d_a > 1$  micron) as measured by the SPLAT-II instrument at the T0 site. It should be noted that the upper-limit sampling range for SPLAT-II is around 2 microns, and thus supermicron particles that are larger than this are not characterized.

Deleted: 5

68

69



70

71 **Figure S8.** Calculated relationship between the mass scattering coefficient and mobility diameter for spherical particles with  
72 density =  $2 \text{ g cm}^{-3}$ . A complex refractive index of  $\text{RI} = 1.5 + 0.0i$  was used.  
73

Deleted: 6

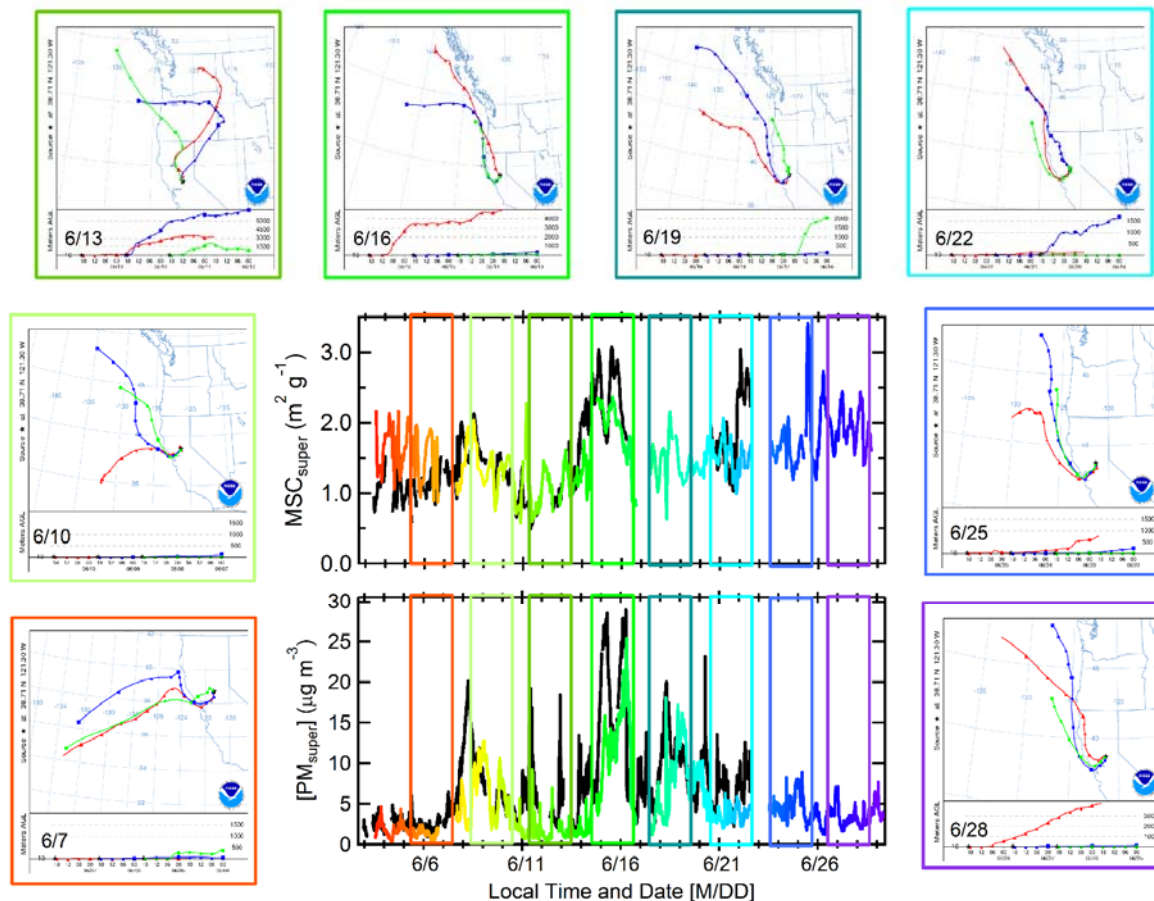


**Figure S2.** The central panels show time-series of the mass scattering coefficient and PM concentration for supermicron particles for both T0 (black lines) and T1 (colored lines). The outer panels show back trajectories calculated from HYSPLIT, using the NAM meteorological data, arriving at the T0 site at noon local time each day. Each outer panel shows three back trajectories that are separated by 24 hours (note that time goes backwards in these panels). The boxes around each outer panel correspond in color to the boxes shown in each of the central panels and provide a visual reference as to which trajectories correspond to which time period.

Deleted: 7

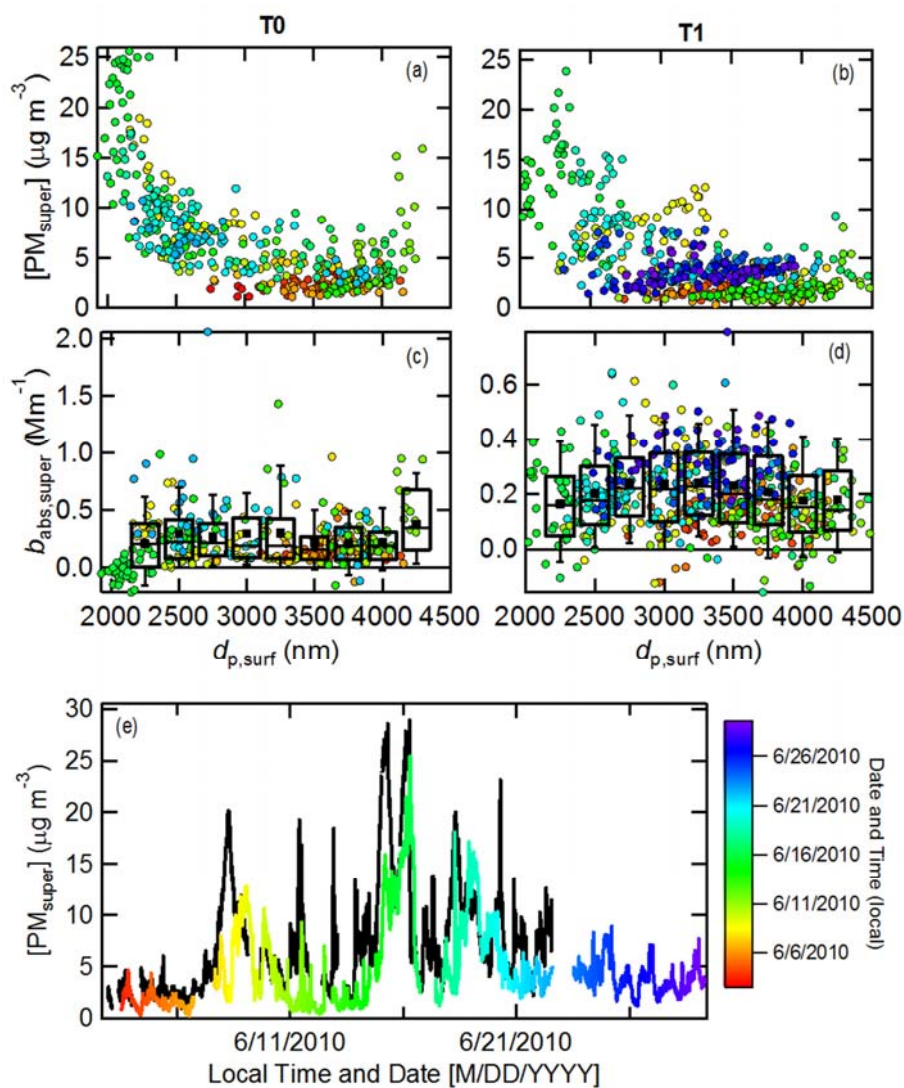


**Figure S10.** The relationship between the supermicron particle concentration (a,b) or the absolute supermicron absorption at 532 nm (c,d) and the surface-weighted median diameter of the supermicron mode. Observations from T0 are shown in (a) and (c) and from T1 in (b) and (d). For reference, the time series of  $[PM_{super}]$  is shown for both sites in panel (e), where T0 is shown in black and T1 in color. The points are colored according to date, as indicated in the color scale.

Deleted: 8



88

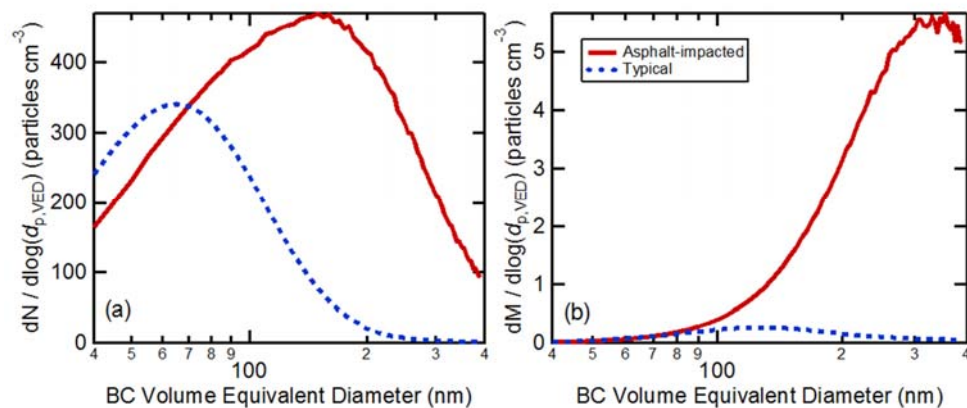
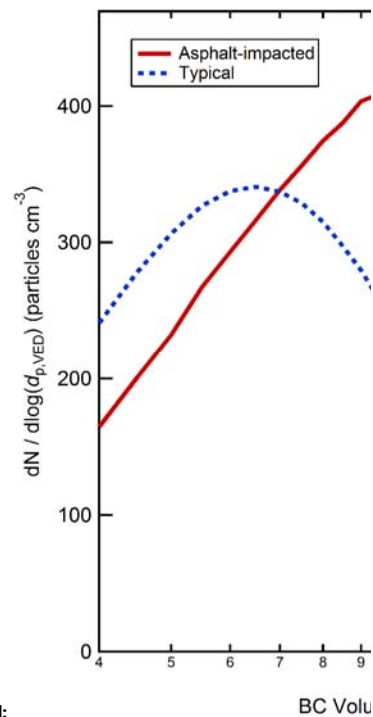


**Figure S11.** Refractory BC (a) number-weighted and (b) mass-weighted size distributions measured by the SP2 during the asphalt impacted period (22 June between 1:15 am and 2:30 am, local time) and during typical time periods. The typical size distribution is shown as a dashed blue line and the asphalt-impacted period as a red line.



Deleted:

Deleted: 9

BC Volu